THE MECHANICS OF PLATE CUTTING WITH APPLICATION TO SHIP GROUNDING.

by

PAUL FRANCIS THOMAS

B.S. Naval Architecture and Marine Engineering

U.S. Coast Guard Academy (1985)

Submitted to the Department of

OCEAN ENGINEERING

In Partial Fulfillment of the Requirements

For the Degrees of

MASTER OF SCIENCE IN NAVAL ARCHITECTURE AND MARINE ENGINEERING

and

MASTER OF SCIENCE IN MECHANICAL ENGINEERING

at the

MASSACHUSETTS INSTITUTE OF TECHNOLOGY

June, 1992

Signature of Author______________________________
Department of Ocean Engineering
May, 1992

Certified by;______________________________
Professor Tomasz Wierzbicki
Thesis Supervisor

Certified by;__________________
Professor David M. Parks
Thesis Reader

Accepted by;______________________________
A. Douglas Carmichael, Chairman
Departmental Graduate Committee
Department of Ocean Engineering

THE MECHANICS OF PLATE CUTTING WITH APPLICATION TO SHIP GROUNDING.

by

Paul Francis Thomas

Submitted to the Department of Ocean Engineering on 8 May,
1992, in partial fulfillment of the requirements for the
degrees of Master of Science in Naval Architecture and
Marine Engineering
and
Master of Science in Mechanical Engineering

Abstract

The mechanics of cutting a plate by a rigid wedge is developed and applied to damage prediction for large tank vessels in high energy grounding.

A closed form solution for the force to cut a plate during initiation of the cutting process is developed from a simple kinematically compatible model of the process. Self-consistent, single term formulas for the indentation force and energy absorption, which are a function of the cut length, are arrived at by relating the "far field" and "near tip" deformation events through a geometric parameter. The solution is identical in form and characteristics to an empirical result reported recently by Lu and Calladine [15].

Plate cutting experiments are presented which show that the closed form solution for the initiation period can be used to estimate the steady state wedge indentation force. In the eight experiments conducted on mild steel and aluminum plate, the cutting process consistently entered steady state when the length of the cut was approximately equal to twice the length of the cutting wedge. The constant steady state cutting force is estimated by evaluating the closed form solution at this length.

A damaged prediction model for double hull tank vessels is then developed using the improved formulation for the plate cutting force. Two other energy absorbing mechanisms included in this model are plate tearing, and girder tearing. The plate tearing and girder tearing forces are derived from application of plasticity and fracture mechanics in conjunction with simplified models of the failure modes. The predictions of this model are compared to the results of Vaughan's method for a typical 39000 DWT tank vessel. Good correlation between the two methods exists when the reef wedge semi-angle is about 40°, but for semi-angles less than 40° Vaughan's method significantly under predicts the amount of damage done. It also is shown that Vaughan's method incorrectly predicts relative performance of alternative tank vessel designs in resistance to grounding damage.

The model offers significant improvement over the existing damage prediction methods because it is not empirical, it is based on steady state plate cutting mechanics, it distinguishes between the energy absorbing contribution of each major structural member, and it is sufficiently accurate for broad practical application.

Thesis Supervisor: Dr. Tomasz Wierzbicki
Title: Professor of Applied Mechanics

Acknowledgement

I wish to express my sincere appreciation to Professor Tomasz Wierzbicki for his constant guidance and enccuragement in preparation of this thesis and other professional projects. I also wish to thank Professor David M. Parks for his careful review of the thesis and many constructive suggestions which have added to its contents and presentation.

Thanks are also due to the crew of the machine and metal shops at Coast Guard Support Center Boston, for their work in the design and manufacture of the experimental apparatus used in the research for this thesis. They include Mr. Harry Lgnchitz, Shop Foreman, Mr. James B. McGowan JR., Marine Machinist, Mr. John McComiskey, Marine Machinist, and Mr. James Balogonese, Marine Welder.

Finally, I'd like to acknowledge LCDR Michael Blair of the Coast Guard Marine Technical and Hazardous Materials Division, Coast Guard Headquarters, for diligent performance of his duty as Graduate Student Liaison Officer. LCDR Blair has consistently assisted me in administrative and logistical matters which greatly facilitated the timely completion of my research and thesis preparation.

Table of Contents

Page

IV. Chapter 3. Damage Prediction Model for Unidirectionally Stiffened Double Hull (USDH) Vessels.

Table of Figures

Notation

B	vessel beam
b	breadth of the reef at any distance from the top
b_1	breadth of damage at bottom plate
b_2	breadth of damage at inner bottom plate
C	empirical constant from Reference [15]
$\dot{E}_b$	rate of bending work
$\dot{E}_m$	rate of membrane work
$\dot{E}_{shear}$	rate of shear work
F	total steady state resisting force of the hull
F_c	total plate cutting force
F_{c1}	cutting force in the bottom plate
F_{c2}	cutting force in the inner bottom plate
F_f	frictional resistance force
F_g	horizontal resisting force of the girders
F_p	plastic resistance force
F_T	total steady state plate tearing force
F_{T1}	tearing force in the bottom plate
F_{T2}	tearing force in the inner bottom plate
H	maximum breadth of the reef at a depth equal to the vessel draft before grounding
h	cell height (bottom separation)
k	number of longitudinal girder sets damaged
$\dot{K}$	rate of curvature
L	vessel length
ℓ	cut length
ℓ_{cr}	critical cut length at which the cutting process transitions to steady state.
ℓ_p	length of membrane stretch zone
ℓ^*	wedge length
ℓ_1^*	wedge length in bottom plate
ℓ_2^*	wedge length in inner bottom plate
M	vessel mass (DWT)
M_o	fully plastic bending moment
$M_{\alpha\beta}$	bending moment tensor
$N_{\alpha\beta}$	membrane force tensor
n	power exponent
R	rolling radius
$\mathbf{R}_o$	essential work to fracture
r	experimentally determined coefficient which describes the cut length at the onset of steady state cutting in terms of wedge length
S_{max}	longitudinal extent of damage
s_1	cell width (side girder separation)
T_c	vessel draft
t	plate thickness
t_g	side girder thickness
t_{p1}	bottom plate thickness
t_{p2}	inner bottom plate thickness
$\dot{u}_\alpha$	plate velocity vector
V	wedge velocity

V_n	velocity of the plate material normal to the wedge surface
V_o	vessel impact velocity
V_t	velocity of the plate material tangential to the wedge surface
W	work of cutting
w	near-tip lift function
z^*	distance up the flap at which the plate begins to tear
α	plate tilt angle / sloping angle of the reef
β	spreading angle of the reef
Δ	local vertical penetration depth of the reef into the vessel
Δ_r	height of reef above the vessel baseline
Δ_L	vertical lift of the ship at contact point with the reef
δ_t	crack opening displacement parameter
$\bar{\delta}_t$	dimensionless crack opening displacement parameter
Λ	$= H/\Delta_r$, reef aspect ratio
η	ratio of cutting force to withdrawal force from [15]
ε	strain rate
$\varepsilon_{\alpha\beta}$	strain tensor
θ	wedge semi-angle / reef wedge semi-angle
$\dot{\kappa}_{\alpha\beta}$	rate of curvature tensor
μ	friction coefficient
$\xi(x)$	membrane deformation zone boundary
σ_o	material flow stress
$\sigma_{\alpha\beta}$	stress tensor
ϕ	rate of rotation

I. Overview

Since the groundings of the tanker EXXON VALDEZ in Alaska's Prince William Sound in 1989, and the tanker AMERICAN TRADER off the coast of Southern California in 1990, the public in the United States and world-wide has been awakened to the dangers of transporting large amounts of oil and other hazardous bulk cargos on our seas. For the first time the commercial shipbuilding industry, and the agencies which regulate it, are being asked to provide protection to the environment through improved tank vessel design. Traditionally, naval architects have designed vessels which are intended to be safe under "normal" operating conditions. Now, however, the industry is forced to address the problem of vessel performance in collision or grounding.

A great deal of the recent literature on ship grounding has consisted of comparative studies [41] [42] [43], which are intended to evaluate the relative effectiveness of alternative tank vessel designs in limiting the extent of damage and loss of cargo due to high energy grounding. To a large extent, these studies have been undertaken to meet the immediate need of U.S. and international regulatory agencies and political bodies for information on which to base long term policy decisions regarding the next generation of tank vessels. Unfortunately, the state-of-the-art in structural analysis of ships has not kept pace with this need for information, and as a result these decisions have been based on technology which is over a decade old. The recent studies have not served to advance the state-of-the-art in damage prediction, but rather they have relied on methods which are outdated and/or lack generality.

The objective of this thesis is to advance the state-of-the-art in damage prediction for steady state grounding of tank vessels. This is primarily accomplished through the application of plate cutting mechanics and small scale experiments to the problem of ship grounding.

The existing damage prediction methods fall into two broad categories; 1) those based on small scale experiments involving a specific hull configuration, and 2) those based on Vaughan's [1] [6] [7] [40] empirical analysis of plate cutting experiments. Both of these general types of approach have limitations which restrict their application.

The formulation of a damage prediction method from small scale experiments is fundamentally correct, but is severely restricted in it's application. The RR701 group of the Shipbuilding Research Association of Japan recently presented such a formulation to the International Maritime Organization (IMO) based on a series of test which involved cutting a scale section of a double hull [43]. They proposed a formula for the cutting force in the form

$$F = \eta \, \sigma_o \, A \, , \tag{1}$$

where η is an empirically determined proportionality constant, σ_o is the material flow stress, and A is the cross-sectional area of damage. The constant η contains many important parameters of the problem including critical strain and fracture toughness of the material, friction coefficient, reef geometry, arrangement of stiffeners and girders, and double bottom separation. As a result, this expression (1) can only be applied to structures which closely resemble the test section, and can not be used for comparative studies.

Vaughan's method of damage prediction is not only limited in application due to its empirical nature, but is fundamentally incorrect because it is based on plate cutting experiments which involved the initiation portion of the cutting process only. When a plate is cut by a wedge of finite width, the cutting force increases with the length of the cut until the process reaches steady state, and then the force levels out. For the most part, the grounding event must be considered as a <u>steady state</u> penetration of a wedge into a stiffened plate, which involves a constant cutting force. It is incorrect to formulate a steady state damage prediction model based initiation experiments alone. The Vaughan method of damage prediction will be discussed further in Chapters Two and Three of this paper because it has been the basis of many of the recent comparative studies.

This paper addresses the two primary limitations of the existing damage prediction methods describe above. It develops a model which is both fundamentally based and general enough for broad practical application. The approach used here follows that developed by Wierzbicki et al. [34 - 38] in applying the concepts of "crashworthiness" to the analysis of ships structures. Three primary energy absorbing mechanisms of the hull girder are separately analyzed using the principles of plasticity and fracture mechanics, and then combined into an overall damage prediction model. These mechanisms are, 1) plate cutting, 2) plate tearing, and 3) girder tearing. Although the plate cutting is the primary focus of the present work, plate tearing and girder tearing are also included, but in a less rigorous fashion.

The thesis is comprised of three chapters. In Chapter One the mechanics of the plate cutting during the initiation phase of the process are developed through careful consideration of a kinematically compatible model. Vaughan [40] and Lu and Calladine [15] have analyzed this problem empirically in the past. The closed form solution developed in Chapter One matches their results for specific configurations, and also allows direct scaling for application to ships.

In Chapter Two, the steady state plate cutting problem is addressed. Experimental data is presented which shows that the closed form solution developed in Chapter One can be used to estimate the steady state plate cutting force. An expression for the force to tear the plate transversely is also derived in this chapter.

In Chapter Three a steady state damage prediction model for double hull tank vessels is developed using the analysis of Chapters One and Two, and some additional analysis of the girder tearing. This model is intended to eliminate the major limitations of the existing damage prediction methods through application of the steady state plate cutting solution, and the use of a non-empirical analysis for the primary failure modes of the major structural members involved in grounding. The model is applied to the damage assessment for a typical Uni-directionally Stiffened Double Hull (USDH) tank vessel. A comparison between Vaughan's method and this model is presented for the absolute and comparative damage assessment cases.

Each chapter has a brief introduction which reviews the literature relevant to that specific topic, and clarifies the existing state-of-the-art and its current application. Each chapter also contains a brief conclusion. The conclusion section at the end of the paper provides an overview of how the present work advances the state-of-the-art, and suggests areas for future research.

II. Chapter 1

Closed Form Solution for the Force of a Wedge Cutting Through a Thin Metal Plate.

1.1 Introduction

The problem of penetration of a wedge into thin metal plates has been the subject of intense research over the past decade [1 - 14]. Often the motivation for undertaking this type of research has been a need to determine contact force and energy dissipation in the process of collision and grounding of ships. An excellent summary of current work in this area was recently presented by Lu and Calladine [15]. It is generally agreed among investigators that the plate resistance to wedge indentation involves two direct mechanisms; "far-field" plastic deformation, and "near-tip" fracture. A third, indirect mechanism addressed in some studies is friction. Attempts have been made in the literature to isolate the above mechanisms and to quantify the individual work or force contributions of each from experimental data. These attempts have not been fully successful, as reviewed in Reference [15].

Lu and Calladine performed a series of well controlled experiments and showed that a single-term empirical formula for the work of cutting, W, adequately described the test results. They proposed the following formula for the work of cutting plates;

$$W = C \, \sigma_o \, \ell^n \, t^{3-n} , \tag{1.1}$$

where σ_o is the material flow stress, ℓ is the length of cut, and t is the plate thickness.

In this form certain parameters of the process (e.g. semi-angle of the wedge and friction coefficient) are lumped together into a single numerical constant, C. In thirty nine tests on mild steel and other metals, Lu and Calladine found this numerical constant to vary in the range C = 0.9 - 3.5, while the exponent was in the range n = 1.2 - 1.4. The corresponding power to which thickness is raised in Equation (1.1) is (3 - n) = 1.8 - 1.6. It is interesting to note that in a steady-state "trousers test" type of experiment involving a shear fracture mode, Yu et al. [22] found the tearing energy to be proportional to $t^{1.61}$.

While Lu and Calladine recognized the existence of two essentially distinct processes of plastic deformation involved in the near-tip and far-field regions of the plate, they also observed that the sum of two effects may be adequately approximated by the single term Equation (1.1), and that no fracture parameter is necessary for correlation of the experimental data.

This point of view has been opposed by Atkins, [16] [17], who suggested that the far-field and near-tip events should give rise to separate, independent terms in the expressions for the energy absorption and hence the indentation force. Furthermore, he argued that the solution should depend explicitly on only one fracture toughness parameter [21]. A somewhat similar point of view is represented by the work of Stronge et al [18] [19] and Reddy and Reid [20], who calculated the work of fracture in axial splitting of metal tubes on the basis of the fracture toughness parameter from linear fracture mechanics. According to such calculations, the contribution of the fracture process to the overall energy absorption is very small.

This chapter resolves the above controversy by showing that the global and local deformation (far-field and near-tip) mechanisms are not independent, as previously believed, but are related through a single geometric parameter. This parameter is the instantaneous bending or rolling radius, R, of cylindrical flaps formed in the wake of the cut. Specifically, the far-field bending work is inversely proportional to R, while the membrane work in the near-tip fracture zone increases in a non-linear way with the rolling radius. The optimization of the instantaneous indentation force with respect to R yields a simple one-term relationship identical in form to that of Equation (1.1). It should be noted that calculation of membrane work near the crack tip in this analysis is based on the Crack Opening

Displacement (COD) parameter, δ_t.

Further analysis of the present formulation reveals that the fracture process enters the solution only through a numerical constant, C. This possibility was overlooked by parties on both sides of the debate. Clearly, the fact that the constant C determined experimentally by Lu and Calladine is different for different materials lends credibility to the present interpretation. It is also shown is this chapter that when the frictional component is added to the solution the indentation force is insensitive to the wedge angle θ, but is strongly dependent on the friction coefficient, μ. These characteristics were observed experimentally and reported by Lu and Calladine [15].

1.2 Formulation of the Problem

The equilibrium of the wedge-plate system is expressed via the principle of virtual work,

$$F_p V = \dot{E}_b + \dot{E}_m \, , \tag{1.2}$$

where F_p is the plastic resistance force, V is the wedge velocity, and $\dot{E}_b$ and $\dot{E}_m$ denote the rates of bending and membrane work respectively. In a plane stress condition these quantities are defined by;

$$\dot{E}_b = \int_S M_{\alpha\beta} \dot{K}_{\alpha\beta} \, dS \; + \; \sum_i M_o^{(i)} \, \phi^{(i)} \, \ell^{(i)} \tag{1.3}$$

$$\dot{E}_m = \int_S N_{\alpha\beta} \dot{\varepsilon}_{\alpha\beta} \, dS \qquad\qquad \alpha , \beta = 1,2 \tag{1.4}$$

where $\dot{K}_{\alpha\beta}$ and $\varepsilon_{\alpha\beta}$ are the curvature rate and strain rate tensors respectively, and $M_{\alpha\beta}$ and $N_{\alpha\beta}$ are the corresponding bending moment and membrane force tensors. The second term on the right hand side of Equation (1.3) is the rate of work on a discontinuous velocity field (rotation rate ϕ), where M_o is, as before, a fully plastic bending moment, σ_o is the flow stress of the material, and t is the plate thickness. The integration in the continuous deformation field is performed over the area S of the plastically deforming regions, while the contribution of a discontinuous field is summed over a finite number of straight line segments of length $\ell^{(i)}$ each.

For rigid-plastic, non-harding material Equation (1.2) gives an upper bound for the instantaneous force F_p if a kinematically admissible velocity field $\dot{u}_\alpha(x,y)$ can be constructed compatible with the kinematic boundary condition (wedge motion V) and the strain rate field ($\dot{K}_{\alpha\beta}$, $\dot{\varepsilon}_{\alpha\beta}$, $\dot{\phi}$). It should be noted that Equation (1.2) is also valid for a cracked body, where the fracture process enters the solution through continuously changing geometry of the wedge-plate system.

Appendix A shows the application of a similar approach to a well understood problem in structural plasticity; the axial crushing of a square prismatic tube. In this problem the mean crushing force of the tube is derived from equating the applied work to the plastic work increment for a currently kinematically admissible flow field. The upper bound expression which results is then minimized with respect to three parameters to produce the least upper bound to the crushing force. This minimization reduces a three term expression to a simple single term expression even though the plastic work is known to involve three distinct mechanisms. This type of analysis will be applied to the wedge indentation problem.

The problem consists in choosing a suitable, kinematically admissible flow field, and optimizing it with respect to one or more free parameters in order to arrive at the best upper bound. In addition to plastic resistance, friction has an influence on the total cutting force. The contribution of friction to the indentation force F_f is addressed separately in Section 1.7.

1.3 Kinematics of the Cutting Process

The kinematic model used to formulate the present theory is shown in Figure 1.1. It is based in part on a visual analysis of the experimental results presented in Reference [15], and in part on simple physical models. Specifically, Figure 3 of Reference [15] is a photograph of a plate which has been cut by a wedge when a small tilt angle ($\alpha = 10°$) was introduced. This is the case for which the model presented here is most valid, because it results in "clean curling" without any reverse curling. More will be said on the origin and consequences of this restriction in Section 1.7.

Consider a wedge of a semi-angle θ advancing into a plate with a constant velocity V. A careful examination of the geometry of the flaps formed in the wake of the cut reveals that the plate material on both sides of the wedge is bent and curled into two variable curvature cylindrical surfaces as in Figure 1.1a. Formation of double curvature flaps is not likely when a small tilt angle is present ($\alpha = 10°$) because it would require considerable membrane deformation in addition to bending, and would greatly increase the amount of energy involved. Since the least work (lowest upper bound) gives the best estimate of force, the structure will go into a purely bending mode and the flaps must deform into a developable or ruled surface, which can be either a cylinder or a cone.

Although the flaps may look like two cones (see Figure 3. of Reference [15]), they in fact can not be. A careful

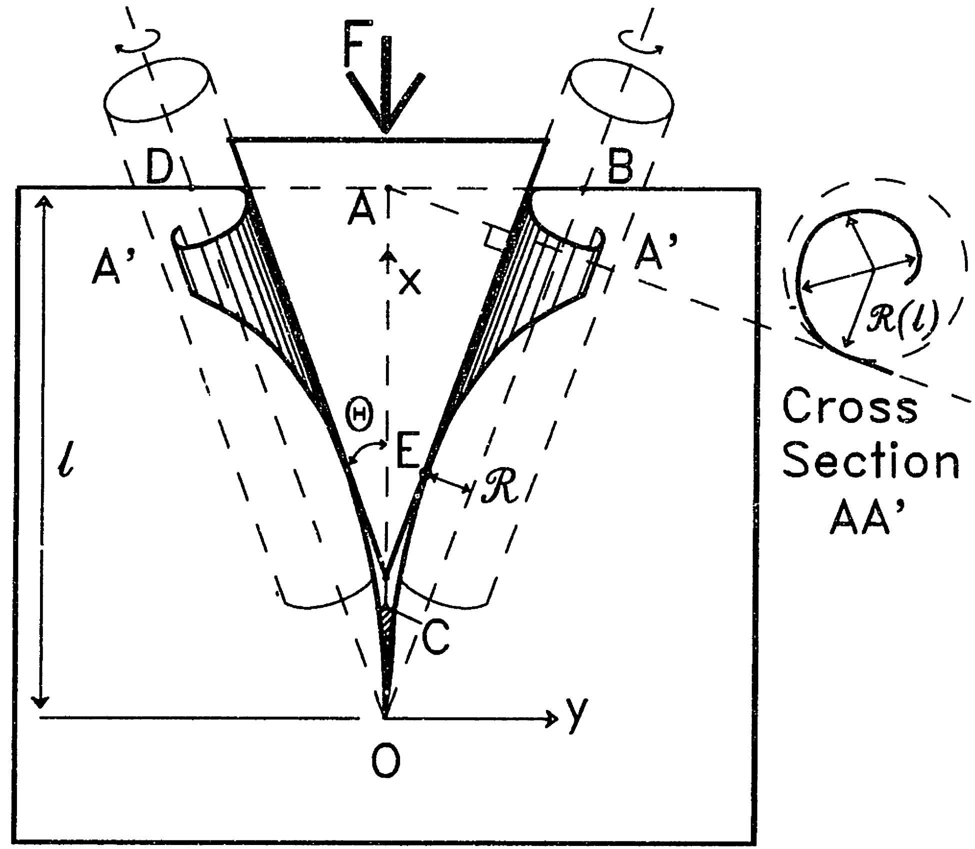

Figure 1.1a

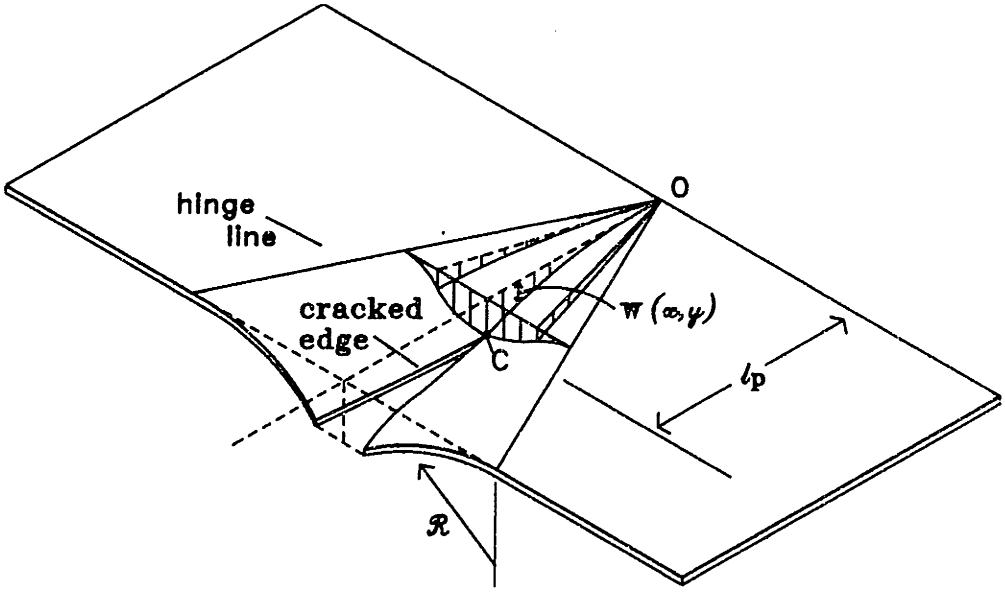

Figure 1.1 a) Overall kinematics of the wedge indentation. b) View from beneath showing lift in the near-tip region. (see Figures 1.2 and 1.3 for details of the near-tip region)

geometrical construction reveals that the wedge would lose contact with the plate if the flaps were rolled into cones, which is contrary to experimental observations. The plate must, therefore, wind into two inclined cylinders with an instantaneous radius of curvature, R. This radius does not have to be constant, and the calculations presented in the subsequent sections show that the curling process starts with a small radius R which increases with the cut length ℓ. For this reason, any cross-section of the flap with a plane normal to the cylinder's axis (AA') reveals a spiral as shown in the insert to Figure 1.1a.

According to this model, the wedge touches the cracked edge of the plate only at one Point E. The wedge is in full contact with a generator of the cylindrical surface EG (rolled edge of the plate), and then looses contact with the plate over the distance EC near the tip region. This geometry is in perfect agreement with photographic evidence presented in References [1], [10], and [15], and our own observations. In other words, the "crease" in the plate consists of a straight line portion parallel to the flank of the wedge and a curved portion, as shown in Figure 1.2 (Section 1.4). It may appear at first sight that the entire crease is a curved line, but this impression is incorrect and is caused by an optical illusion due to the proximity of the helical crack edge.

For the reader who has difficulty visualizing the assumed geometry it is easy to construct a simple physical model by cutting a sheet of paper and curling the edges. Another view of this geometry (seen from the back or beneath) is presented in Figure 1.1b. This picture shows the out-of-plane lift of the plate near the crack tip. As shown, the lift emanates radially from the Point O with increasing amplitude.

As shown in Figure 1.1a, the intersection of the instantaneous axis of the cylinders locates the initiation point O of a fully plastic deformation zone. Consider a triangular region of the plate, OAB. This region curls into a curvilinear triangle OA'B, and the cut edge OEA' forms a modified helical line (a normal helical line is formed by wrapping a triangle over a constant radius cylinder). The separation between the right and left modified helical is denoted by δ, but, as explained in the next section, it is only in a material with no resistance to fracture that the crack extends all the way to the origin. In a real material, the hatched section in Figure 1.1a is actually solid and the distance between the helical lines (separation $\delta(x)$) simply indicates the amount of stretch that must be applied to the crack tip to close the gap. In addition to the horizontal separation there is an out-of-plane lift near the crack tip $w(x,y)$ which results in bending deformation. A close-up view of the near tip deformation is shown in Figures 1.2 and 1.3.

Of interest to the near-tip fracture process is the behavior of the function δ near the point O. Assuming that locally the radius of the cylinder is constant in θ, the expression for δ can be calculated from the geometry of the problem.

$$\delta = 2\left[x \sin\theta - R \sin\left(\frac{x}{R} \sin\theta\right)\right] \cos\theta \,, \tag{1.5}$$

where x is measured from Point O along the axis of symmetry. Expanding the second term on the right hand side of (1.5) in a Taylor series for small x/R, and retaining the first two terms, an approximate expression for the separation is obtained,

$$\frac{\delta}{R} = \frac{1}{3}\left(\frac{x}{R} \sin\theta\right)^3 \cos\theta \,. \tag{1.6}$$

1.4 The COD Criterion

The fracture of the plate in front of the wedge tip can be conveniently described in terms of the Crack Opening Displacement (COD) criterion. A similar criterion was used by Parks et al. [26],[27],[28], in the related problem of "unzipping" of a tube by an internal pressure. <u>In a material with zero fracture toughness, the length of the cut due to wedge indentation would extend from Point A all the way to Point O in Figure 1.1a</u>. This length is denoted ℓ, and is treated as a process parameter, or independent variable, in the problem. The resulting separation for this type of material $\delta(x)$, and lift $w(x)$, are shown in the inset of Figure 1.3 (Section 1.5). For ductile materials however, the ligament holds the plate together (the gap is closed) until a critical separation or crack opening displacement δ_t is reached. A finite value of δ_t has the effect of shortening the theoretical cut length ℓ by a distance ℓ_p, which is the distance from the origin to the crack tip. Note that over this distance the material is unfractured, and that separation occurs only above the Point C. Details of the near-tip region are shown in Figures 1.2 and 1.3. The magnitude of ℓ_p can be uniquely determined from the geometry of the problem and the value of δ_t. Clearly the parameter δ_t will be different for different materials, and it appears that the COD approach is particularly useful in characterizing fracture properties of ductile sheets. Alternatively, the Crack Opening Angle could be used in the formulation, and may be preferable when the geometry of the crack tip is complicated.

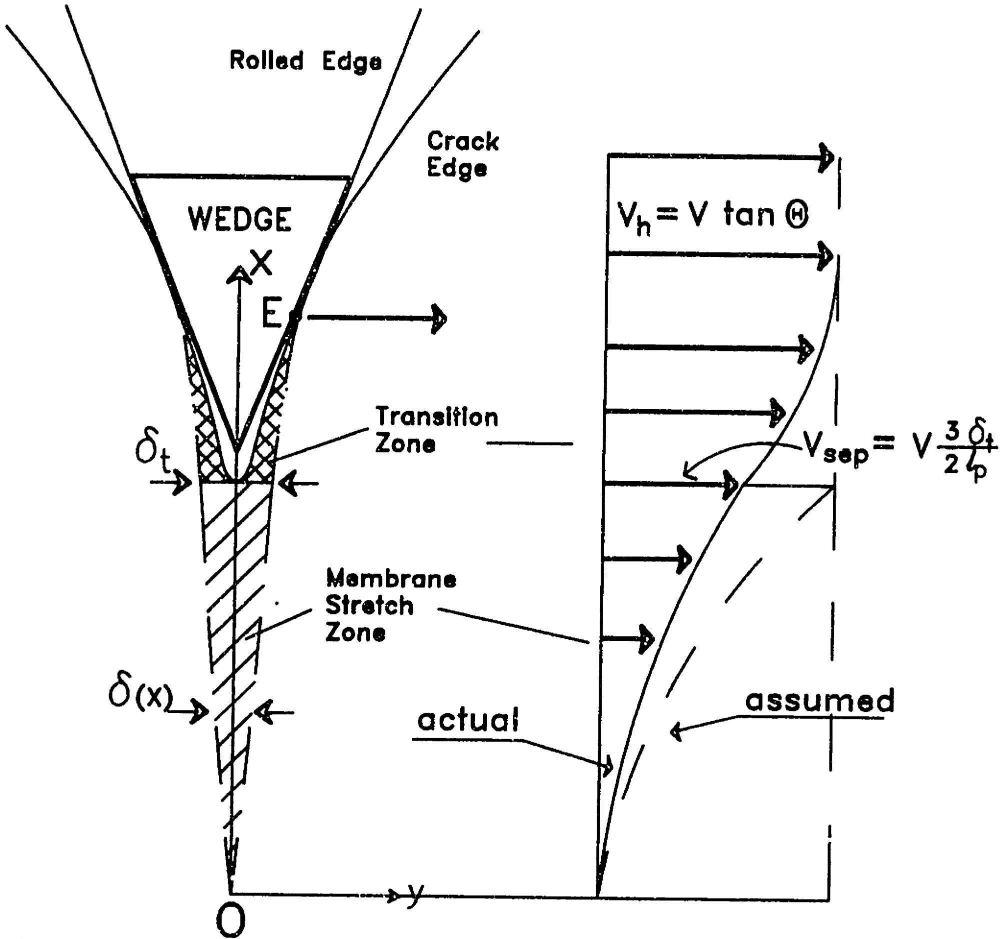

Figure 1.2. Displacements and velocity profiles in the near-tip deformation zone.

In Reference [26], the crack opening displacement parameter was taken to be equal to the tube thickness, $\delta_t = t$. Here we will keep δ_t, or dimensionless critical separation, $\overline{\delta}_t = \delta_t/t$, as a parameter. It is assumed that $\overline{\delta}_t$ is independent of the cut length (except at the onset of indentation) and that it fully characterizes rigid-plastic plane stress tearing of metal sheets.

The shaded zone (single hatched) in Figure 1.2 illustrates the "amount" of membrane stretch in the y direction of the near-tip plastic zone. The double hatched area is a transition zone which connects the near-tip membrane deformation to the far-field bending. In this transition zone there must be plastic extension in the direction parallel to the crack edge. More discussion on the effect of the transition zone is given in Section 1.5.

Returning to the near-tip zone (single hatched section of Figure 1.2), plastic deformation extends from the axis of symmetry to a certain boundary curve $\xi(x)$ which separates the plastic and elastic regions (see Figure 1.3). The length of the plastic zone, ℓ_p, can be calculated from (1.6) by setting $\delta = \delta_t$ and $x = \ell_p$;

$$\frac{\ell_p}{t} = 1.44 \left(\frac{R}{t}\right)^{\frac{2}{3}} \bar{\delta}_t \, (\cos\theta)^{-\frac{1}{3}} \, (\sin\theta)^{-1} \, . \tag{1.7}$$

The normalized length of the plastic membrane zone is then expressed in terms of the dimensionless fracture parameter $\bar{\delta}_t$ and the instantaneous rolling radius R, yet to be determined.

1.5 Calculation of Bending and Membrane Work

The rate of internal energy dissipation in the plate is calculated from the kinematic model explained in Section 1.3. A number of simplifying assumptions have been made to facilitate effective calculation of the rate of work dissipation in the bending and membrane modes. These are:

(i) The material is treated as rigid-perfectly plastic with an average flow stress σ_o. This flow stress has the same value in both the bending and membrane deformation modes.

(ii) The plastic interaction of the bending moment $M_{\alpha\beta}$ and the membrane force $N_{\alpha\beta}$ in the doubly curved portion of the plate near the crack tip is neglected. This assumption results in over estimation of the actual rate of energy dissipation. Note that the contribution of bending in both the near-tip and remote fields has been included in this formulation. What is neglected is a small reverse bending needed to close the gap in the near-tip zone (see insert of Figure 1.3).

(iii) Plastic in-plane shear strain is neglected in the membrane zone. The validity of this assumption is discussed in Appendix B.

(iv) The small curvature and out-of-plane displacements in the near-tip membrane deformation zone are neglected in the strain rate calculations.

(v) Plastic work in the near-tip zone is predominantly dissipated by the diffused mode.

The plane stress yield condition is used to relate the components of the stress tensor $\sigma_{\alpha\beta}$;

$$\sigma_{xx}^2 - \sigma_{xx}\sigma_{yy} + \sigma_{yy}^2 + 3\sigma_{xy}^2 = \sigma_o^2 . \tag{1.8}$$

The associated flow rule gives three independent equations;

$$\begin{aligned} \dot{\epsilon}_{xx} &= \lambda\,(2\,\sigma_{xx} - \sigma_{yy}) \\ \dot{\epsilon}_{yy} &= \lambda\,(2\,\sigma_{yy} - \sigma_{xx}) \\ \dot{\epsilon}_{xy} &= \lambda 6\,\sigma_{xy} , \end{aligned} \tag{1.9}$$

from which all components of the stress tensor can be calculated given $\dot{\varepsilon}_{\alpha\beta}$.

Bending Work

According to the assumed kinematics of the problem all plastic bending is concentrated in two moving hinge lines, OB and OD on Figure 1.1a, and no work is dissipated in the continuous bending mode, $\dot{K}_{\alpha\beta} = 0$. The curled portion of each flap rotates as a rigid body about these lines. The rate of bending work is equal to the product of the fully plastic bending moment M_o, the rate of rotation ϕ, and the length of the hinge lines;

$$\dot{E}_b = 2 M_o \phi \ell (\cos\theta)^{-1} , \tag{1.10}$$

where σ_o is understood to be the average flow stress in the bent region of the plate.

The rate of rotation at the moving hinge line which sweeps through the plate and leaves behind a curved cylindrical surface is calculated from the condition of kinematic continuity (Hopkins [29]),

$$\phi = \frac{V_n}{R} = \frac{V \sin\theta}{R} . \tag{1.11}$$

Here V_n is the component of the indentation velocity normal to the cylinder axis. Combining (1.10) and (1.11) gives the rate of bending work;

$$\dot{E}_b = \frac{4}{\sqrt{3}} \frac{\sigma_o t^2}{4} \frac{\ell}{R} V \tan\theta . \tag{1.12}$$

Membrane Work

The rate of membrane work in the plane stress condition is,

$$\dot{E}_m = t \int_S \sigma_{\alpha\beta} \dot{\epsilon}_{\alpha\beta} \, dS , \tag{1.13}$$

where $x_\alpha(x,y)$ is a local rectangular coordinate system with origin at point O, and S is the area of the membrane zone.

The strain rate is

$$\dot{\epsilon}_{\alpha\beta} = \frac{1}{2} (\dot{u}_{\alpha,\beta} + \dot{u}_{\beta,\alpha}) , \tag{1.14}$$

where $\dot{u}_\alpha = (v_x, v_y)$ are components of the velocity vector in the x and y directions, respectively. Equation (1.14) carries with it the previously stated assumption that small reverse curvature in the plastic membrane zone is neglected in the strain rate calculation.

The wedge motion results in a quasi-steady state process in which the component of the strain rate in the direction of the wedge motion must vanish, $\varepsilon_{xx} \equiv 0$. If this were not the case compressive strain would accumulate in front of the crack tip, which is not physically possible. Additionally, the shear strain rate is neglected in the rate of plastic work calculations, $\varepsilon_{xy} = 0$. The justification of this assumption is given in Appendix B.

Given the above assumptions, it follows from the flow rule (1.9) that $\sigma_{xx} = ½ \sigma_{yy}$, $\sigma_{xy} = 0$, and from the yield condition (1.8) that $\sigma_{yy} = (2/\sqrt{3})\sigma_o$. With this, the expression for the in-plane membrane rate of work (1.13) simplifies to

$$\dot{E}_m = 2t\int_0^{\ell_p}\int_0^{\xi(x)} \frac{2}{\sqrt{3}}\,\sigma_o\dot{\varepsilon}_{yy}\,dy\,dx = 2t\int_0^{\ell_p}\int_0^{\xi(x)} \frac{2}{\sqrt{3}}\,\sigma_o\frac{dv_y}{dy}\,dy\,dx\,, \qquad (1.15)$$

where $\xi(x)$ is an unknown boundary of the membrane deformation region in the transverse direction.

Figure 1.3 shows a close-up of the membrane deformation region and an arbitrary cross section B-B. The upper cross section is typical of a material with zero fracture toughness in which the wedge causes lifting and separation of the plate by a distance w(x) and $\delta(x)$ respectively. In the lower cross section of Figure 1.3, a material with a finite value of fracture toughness will lift and stretch the distance $\delta(x)$ to resist fracture and close the gap. This plastic stretching extends in the y direction to the unknown boundary, $\xi(x)$, beyond which the material behaves elastically.

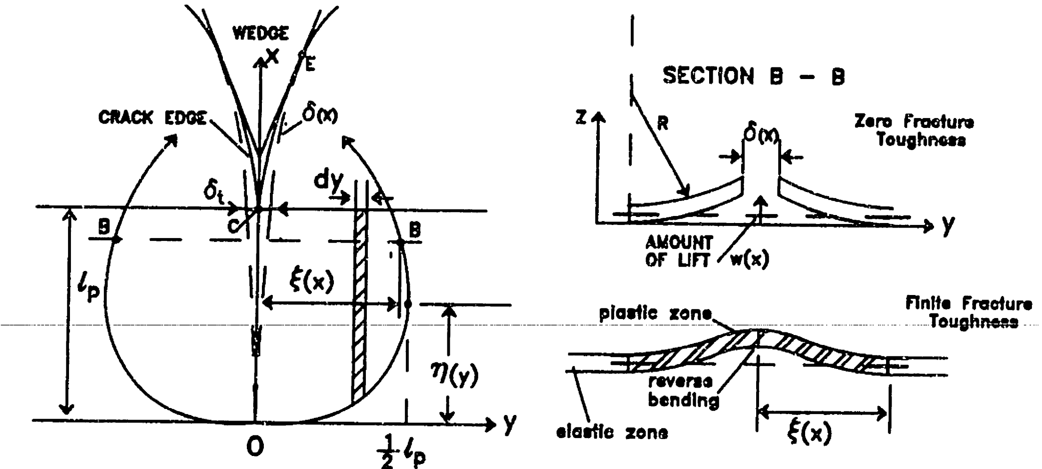

Figure 1.3. **The extent of the membrane deformation zone near the crack-tip.**

The integration of (1.15) with respect to y yields

$$\dot{E}_m = \frac{4}{\sqrt{3}}\, t\, \sigma_o \int_0^{l_p} v(x)\, dx\,, \tag{1.16}$$

where v(x) denotes the velocity at the symmetry line relative to the undisturbed material, $v(x) = v_y(x=0) - v_y(x=\xi) = v_y(x=0)$. Note that the velocity of the boundary of the plastic zone in the transverse direction is zero. In this way, the unknown transverse extent of the plastic deformation zone $x = \xi$, shown in Figure 1.3, does not enter the solution.

The velocity in the transverse direction ranges from zero at point O, to a maximum value, V tan θ, at the point of contact between the wedge and the cut edge (Point E). The shape of the velocity profile v(x) in this region must be compatible with the previously calculated shape of the displacement field (separation profile) given by Equation (1.6) (see Figure 1.2). The separation has been shown to be a cubic function of x, $\delta = Ax^3$. The corresponding velocity is;

$$V_{sep}(x) = \frac{\partial}{\partial t}\left(\frac{\delta}{2}\right) = \frac{\partial}{\partial x}\left(\frac{\delta(x)}{2}\right)\frac{\partial x}{\partial t}. \quad (1.17)$$

For the steady-state process dx/dt = V. Using (1.6), (1.7), and (1.17), the separation velocity can be found;

$$V_{sep}(x) = \frac{3\bar{\delta}_t}{2\,\ell_p} V \left(\frac{x}{\ell_p}\right)^2. \quad (1.18)$$

Evaluating this expression at the point $x = \ell_p$, the separation velocity at the crack tip is;

$$V_{sep}(x{=}\ell_p) = \frac{3\bar{\delta}_t}{2\,\ell_p} V. \quad (1.19)$$

The velocity (1.19) is different from the transverse velocity of the point E, at which first contact is established between the wedge and the fractured surface of the plate. This velocity is determined by the wedge motion;

$$V_h = V \tan\theta . \quad (1.20)$$

The relationship between V_{sep} and V_h is shown in the transverse velocity profile of Figure 1.2. Usually $\tan\theta > 3\delta_t/2\ell_p$, and the difference in transverse velocities of points C and E (Figure 1.2) must exist to allow for a variable shape of the opening near the crack tip. Clearly, some plastic work is dissipated through in-plane stretching and shear in the transition zone CE (double hatched section in Figure 1.2). Beyond this region there is only inextensional deformation in the form of out-of plane bending. The rate of plastic work in the transition region has not been explicitly accounted for in the present formulation. The additional contribution will be included in the present analysis by keeping the size of the plastic zone ℓ_p unchanged while increasing the crack tip velocity from the actual value V_{sep} (Equation (1.19)) to the higher value V_h (Equation (1.20)) as shown in Figure 1.2. The final expression for the velocity profile then becomes

$$v(x) = V \tan\theta \left(\frac{x}{\ell_p}\right)^2 . \tag{1.21}$$

Introducing (1.21) into (1.16) and performing the integration gives the final expression for the rate of membrane work:

$$\dot{E}_m = \frac{4}{3\sqrt{3}} \sigma_o t \, \ell_p V \tan\theta . \tag{1.22}$$

With the rates of bending and membrane work as stated, the equilibrium equation (1.2) yields;

$$F_p = \frac{2}{\sqrt{3}} \sigma_o t^2 \left[\frac{1}{2} \frac{\ell}{R} + \frac{2}{3} \frac{\ell_p}{t}\right] \tan\theta . \tag{1.23}$$

Now the expression for the length of the near-tip plastic zone ℓ_p defined by (1.7) can be introduced into (1.23) to give the instantaneous cutting force:

$$F_p = \frac{2}{\sqrt{3}} \sigma_o t^2 \left[\frac{1}{2} \frac{\ell}{R} \tan\theta + 0.96 \left(\frac{R}{t} \right)^{\frac{2}{3}} \overline{\delta}_t \left(\cos\theta \right)^{-\frac{4}{3}} \right]. \quad (1.24)$$

It is recognized that there may be other kinematically admissible fields which will lead to different expressions for the resistance force. The present model, however, is fully geometrically compatible and provides a smooth link between the local deformation ahead of the crack tip and the global out-of-plane curling. It is believed that <u>any</u> model which is both kinematically compatible and physically realistic will yield a result which is both a good upper bound to the actual cutting force, and very close to that obtained in the present analysis.

1.6 The Rolling Radius and Minimum Cutting Force

The first term in the Equation (1.24) for the cutting force is inversely proportional to R, while the second term is proportional to $R^{2/3}$. Therefore, the function $F_p(R)$ (Equation 1.24) for the instantaneous cutting force has an analytical minimum with respect to R. The physical interpretation is that for a given cut length, the rolling radius adjusts itself so that the sum of the bending and membrane rates of work are minimized. Thus, an expression for the instantaneous rolling radius can be easily found from the condition $dF_p/dR = 0$.

$$R = 0.86\, t^{\frac{2}{5}}\, \ell^{\frac{3}{5}}\, (\overline{\delta}_t)^{-\frac{3}{5}}\, (\sin\theta)^{\frac{3}{5}}\, (\cos\theta)^{\frac{1}{5}}\,. \tag{1.25}$$

As mentioned in Section 1.3, the minimization procedure in the presence of ever changing geometry can be applied to plastic fracture when the assumed kinematics of the problem correspond closely to reality, as is the case with the present model. The minimization process can be regarded as a sequence of "upper-bound" calculations with a continuously updated geometry.

It is seen that the radius given by Equation (1.25) is an increasing function of the cut length so that the flaps wind up on cylinders whose radii increase with the total depth of penetration. This is shown in the insert of Figure 1.1a by the helical cross-section. It is also worth mentioning that this radius is independent of the material yield strength because it is the ratio of bending and membrane rates of work that matters, not the absolute magnitude.

Taking $t = 0.9$ mm, $\theta = 20°$, and $\bar{\delta}_t = 1$, gives;

$$R = 0.43\ (\ell)^{0.6} \tag{1.26}$$

The photographic evidence presented in Reference [15] supports the above results in the sense that the radius can be seen to increase with cut length. Equation (1.26) seems to under-predict the magnitude of the rolling radius. As discussed in Section 1.7, this difference appears to be due primarily to friction effects which have not yet been accounted for. The friction force between the wedge and the flap tends to "open-up" the curls and enlarge the radius.

From Equations (1.7) and (1.25) we can infer that the length of the plastic zone also increases with cut length, according to;

$$\frac{\ell_p}{t} = 1.30\left(\frac{\ell}{t}\right)^{\frac{2}{5}} (\bar{\delta}_t)^{\frac{3}{5}} (\cos\theta)^{-\frac{1}{5}} (\sin\theta)^{-\frac{3}{5}}\ . \tag{1.27}$$

This result is physically justifiable because the plate geometry changes in the initial indentation/ cutting problem, and so must the near-tip field. Only in the case of steady state ploughing of a constant width wedge through a plate will the length of the plastic zone be constant.

Replacing the radius terms in (1.24) with the expression (1.25) reduces the formula for minimum cutting force to the single-term expression;

$$F_p = \frac{2}{\sqrt{3}} \sigma_o (\overline{\delta}_t)^{0.6} t^{1.6} \ell^{0.4} (\sin\theta)^{0.4} (\cos\theta)^{-1.2} (0.58 + 0.87),$$

$$= 1.67 \sigma_o (\overline{\delta}_t)^{0.6} t^{1.6} \ell^{0.4} (\sin\theta)^{0.4} (\cos\theta)^{-1.2}, \qquad (1.28)$$

where the coefficients 0.58 and 0.87 are the fractional contribution of bending and stretching work respectively.

Thus the cutting force depends on two material parameters (σ_o and δ_t), the plate thickness and the wedge angle, and is an increasing function of the cut length. Furthermore, the minimization procedure predicts that the ratio of bending to membrane energy is fixed at 2:3, as shown by the coefficients in Equation (1.28). Most importantly, Equation (1.28) predicts the correct magnitude of the fractional power ($n = 1.4$) to which thickness and cut length are raised. This exponent is within the range $1.2 \leq n \leq 1.5$ determined experimentally by Lu and Calladine [15], and described in the introduction to this paper. At the same time, the present solution has a rather strong dependence on the wedge angle θ, which is contrary to the observations made in reference [15]. Also, the magnitude of the cutting force determined by (1.28) is significantly lower than that observed in the experiments. Accordingly, frictional effects must be considered to determine if this will bring the theory closer to experiments.

1.7 The Contribution of Friction

Although bound theorems are not generally valid in the presence of friction, they appear to be so when, as here, the frictional forces are directly proportional to the applied load. As a result, it is valid to add the friction effects directly to the solution as it has been developed to this point.

The relative motion of the wedge with respect to the plate has two components. First, there is an in-plane sliding with the corresponding tangential velocity;

$$V_t = V\cos\theta \,. \tag{1.29}$$

Second, the out-of-plane curling of the flaps produces a vertical velocity which is approximately equal to the hinge line velocity V_n (for constant rolling radius),

$$V_n = V\sin\theta \,. \tag{1.30}$$

Therefore, the absolute magnitude of the sliding motion is equal to the wedge velocity, V,

$$\sqrt{V_t^2 + V_n^2} = V\,, \tag{1.31}$$

which is independent of the wedge angle θ. (see Figure 1.4)

The force of friction acts along the axis of the velocity vector in the direction opposite the sliding motion, and is inclined at an angle θ with respect to the plate. This explains why it is necessary to tilt the plate with respect to

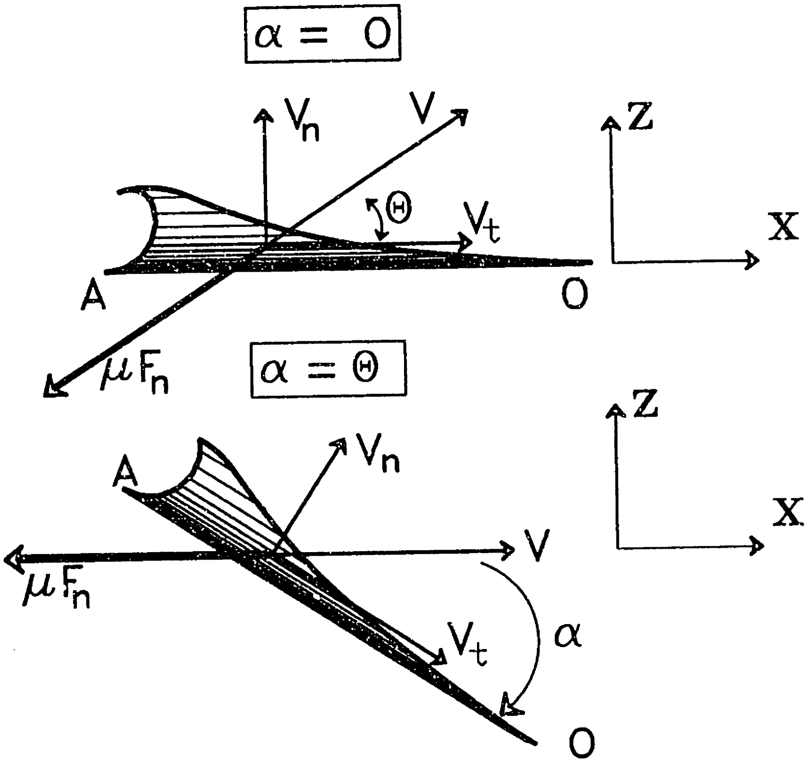

Figure 1.4 **The frcitional force is equilibrated only when the tilt angle α is equal to the wedge angle θ**

the wedge motion to ensure steady curling. Vaughan [7] and Lu and Calladine [15] introduced a small tilt angle $\alpha = 10°$ precisely for this reason. With no tilt angle the out-of-plane component of the frictional force opposes the curling process and tends to "open up" the already bent flaps. When the frictional force builds to a certain critical value (local peaks on Figure 5a of Reference [15]), the motion is reversed and the plate starts to curl in the opposite direction. This accounts for the alternating back-and-forth folding observed by Jones et al. [10] and Lu and Calladine [15], and may also explain the significant drop in the plastic work when a small tilt angle was present. Introduction of the tilt angle reduces or eliminates the reverse bending which has the effect of decreasing energy absorption since reverse bending takes more energy than "clean curling". It should be mentioned in passing that the tilt angle α also enters the solution through the modification of the membrane contribution, but this effect is not quantified here. As α increases the size of the plastic zone grows in the transverse direction and more of the plate in front of the wedge tip is "pre-stressed". Of course it is easier to cut a stressed strip than a slack one, and this phenomenon may affect energy dissipation.

Figure 1.4 shows that in order to prevent reverse bending the tilt angle should be greater than the wedge semi-angle, $\alpha > \theta$. Indeed, in every case where this condition was met, no bending reversal was reported in reference [15], and when $\alpha < \theta$ alternating bending occurred. In the limiting case, $\alpha = \theta$, reverse bending was observed in some of the tests.

The additional force due to friction, F_f, in the plate cutting process can be calculated from the work balance equation;

$$F_f V = 2 F_n \mu V, \tag{1.32}$$

where $F_n = (F_p/2) \sin\theta$ is the normal component of the plastic resistance force. The frictional force then becomes;

$$F_f = \frac{F_p \mu}{\sin\theta} . \tag{1.33}$$

The total resistance to the wedge in plate cutting is the sum of the plastic resistance force F_p, given by (1.28), and the frictional force F_f, given by (1.33).

$$F_c = F_p + F_f = 1.67\,\sigma_o\,(\overline{\delta}_t)^{0.6}\,\ell^{0.4}\,t^{1.6}\,g(\theta)\ . \qquad (1.34)$$

where,

$$g(\theta) = \frac{1}{(\cos\theta)^{1.2}}\left[(\sin\theta)^{0.4} + \frac{\mu}{(\sin\theta)^{0.6}}\right]. \qquad (1.35)$$

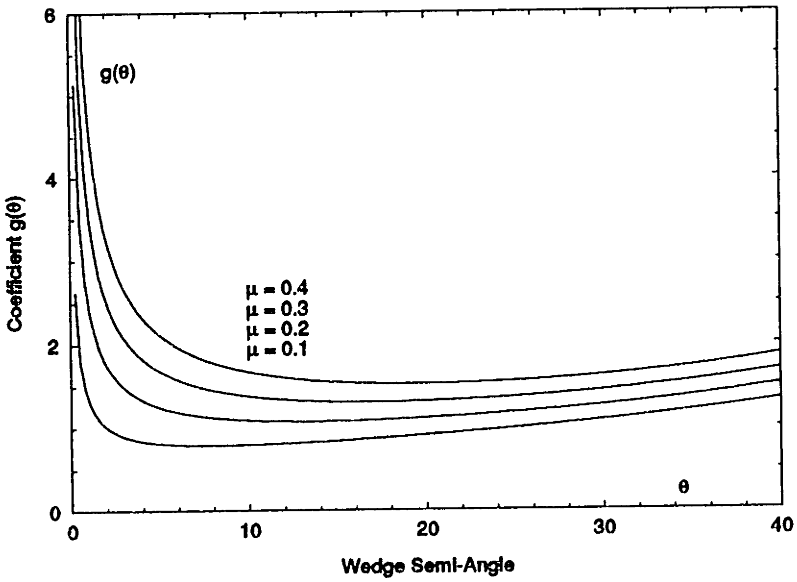

Figure 1.5. **Plot of the function g(θ) showing weak dependence on the wedge semi-angle.**

A plot of the function g(θ) (Figure 1.5) reveals that the cutting force depends very weakly on the magnitude of the wedge semi-angle, particularly in a certain range. For example, with $\mu = 0.3$, the difference in $g(\theta)$ between $\theta = 10°$ and $\theta = 20°$ is less than 2%. This is in perfect agreement with the experimental observations of Lu and Calladine who reported this difference to be about 5%.

Because of this weak dependence on θ, it is reasonable to simplify the expression for cutting force, (1.34), by evaluating it at the minimum value of the function $g(\theta)$ for each value of μ plotted in Figure 1.5. The approximate angle to minimize $g(\theta)$ is defined by;

$$\sin\theta_{\min} = \frac{3\mu}{2}\,, \tag{1.36}$$

and the corresponding minimum function g is

$$g(\theta)_{\min} = \left[\left(\frac{3}{2}\right)^{0.4} + \left(\frac{2}{3}\right)^{0.6}\right]\mu^{0.4} = 1.96\,\mu^{0.4}\,. \tag{1.37}$$

Equation (1.37) implies that, at the optimum angle $\theta_{\min}$, 60% of the plate resistance comes from plastic dissipation and the remaining 40% is due to friction. Again, this result is in agreement with the observations of Lu and Calladine who estimated the contribution of friction by measuring the ratio of the force of withdrawal to the force of penetration and found it to be $\eta = 0.4$.

Substituting (1.37) into (1.34), gives the practical expression for the approximate penetration force;

$$F_c = 3.28\,\sigma_o\,(\overline{\delta}_t)^{0.6}\,\mu^{0.4}\,\ell^{0.4}\,t^{1.6}\,. \tag{1.38}$$

Or, the non-dimensional penetration force;

$$\frac{F_c}{\sigma_o t^2} = C\left(\frac{\ell}{t}\right)^{0.4}, \tag{1.38a}$$

where,

$$C = 3.28\,\mu^{0.4}\ (\overline{\delta}_t)^{0.6}\,. \tag{1.38b}$$

1.8 Energy Absorption

The total work in the cutting process is made up of energy dissipated by plastic deformation and energy of friction. These two components have been expressed in terms of a single formula through the wedge angle minimization procedure. Earlier in the paper the fractional rate of the plastic energies of bending and membrane deformations were lumped into a single-term relationship by means of minimization with respect to the rolling radius. From the definition of work,

$$W = \int_0^{\ell} F(\ell)\, d\ell \,, \tag{1.39}$$

we can calculate the final expression for the work done in resisting the wedge in plate cutting;

$$W_c = 2.34\, \sigma_o\, \ell^{1.4}\, t^{1.6}\, \mu^{0.4}\, (\bar{\delta}_t)^{0.6} \,. \tag{1.40}$$

In dimensionless form the work is

$$\frac{W_c}{\sigma_o t^3} = C_1 \left(\frac{\ell}{t}\right)^{1.4} . \tag{1.40a}$$

These equations are identical in form to those proposed by Lu and Calladine (Equation (1.1) with n=1.4), and they give an explicit meaning to the numerical constant C_1,

$$C_1 = 2.34\, \mu^{0.4}\, (\bar{\delta}_t)^{0.6} \,. \tag{1.41}$$

For example, taking $\mu = 0.3$ (which is reasonable for copper - steel sliding contact [30]) and $\overline{\delta}_t = 1$, the constant given by (1.41) is $C_1 = 1.42$. This is in remarkably close agreement with the results of tests in copper sheets reported in Reference [15], where the constant was found to be $C = 1.4$ when the exponent was $n = 1.4$.

According to the present theory, the work of plate cutting is dissipated in the three primary mechanisms as follows;

Bending	24%,
Membrane	36%,
Friction	40%.

This result is independent of the values of μ and θ over a wide range of wedge angles in the vicinity of the optimum angle, θ_{min} given by (1.36). For larger or smaller angles the distribution may be different. Jones [10] estimated the plate bending energy to be only 10% of the total energy in experiments with zero plate tilt, $\alpha = 0$. His calculations, however, were based on measurement of the final distorted shape of the flap, and the minimum work paths he assumed may be very different from the actual loading path. In the alternating folding mode discussed earlier, some plate elements are bent and re-bent until the final shape is reached, and the contribution of bending is thus increased. Finally, it should be noted that while the relative ratio of contributing energies is fixed, the magnitudes of each component grows with the cut length according to $\ell^{1.4}$.

1.9 Discussion and Conclusions

A self-consistent theory has been developed for the plate cutting phenomenon which combines the effects of plasticity, fracture, and friction into a single-term formulation. Despite its simplicity, the theory describes all of the main features of the cutting process discussed in the comprehensive experimental paper by Lu and Calladine [15]. In particular, the present solution;

(i) Predicts correct functional dependence of the cutting force on plate thickness $t^{1.6}$, and length of cut $\ell^{0.4}$. Explicitly shows how the numerical constant in the Lu and Calladine formula depends on the COD and the friction coefficient.

(ii) Explains a weak dependence of the solution on the wedge angle θ.

(iii) Formulates and quantifies the effect of friction on the cutting force, and explains the significant drop in the force observed by Lu and Calladine [15] when the tilt angle α is added.

(iv) Demonstrates the correctness of the Lu and Calladine claim that a single term solution adequately describes the cutting process.

(v) Agrees with Atkins [17] point of view that a fracture parameter must enter the expression for the plate cutting force. The COD parameter $\overline{\delta}_t = (\delta_t/t)$ was used in the present analysis.

Comparison of the present theory to the experimental results presented in Reference [15] is shown in Figures 1.6 and 1.7. The plot of dimensionless force vs. length (Figure 1.6) shows that the shape of the theoretical curve generally agrees with the experimental data, and that a value of μ between 0.2 and 0.3 ($\overline{\delta}_t = 1$) gives best correlation with tests done on mild steel plates. Lu and Calladine also tested aluminum, brass, copper and dural plates, but no force-displacement diagrams were presented.

Figure 1.7 is a log-log plot of dimensionless energy for $\mu = 0.3$. Integration to work and the log-log representation reduces the scatter of the experimental data shown on Figure 1.6, and demonstrates that good correlation between the present theory and the results presented in Reference [15] is achieved when $\mu = 0.3$. Lu and Calladine used this plot and the least squares method to determine that the exponent n in the expression for energy is in the range $n = 1.2 - 1.4$. They further simplified their solution by choosing a single standard value of $n = 1.3$. In the present formulation the value of $n = 1.4$ for this exponent comes directly from the calculation of bending and membrane work.

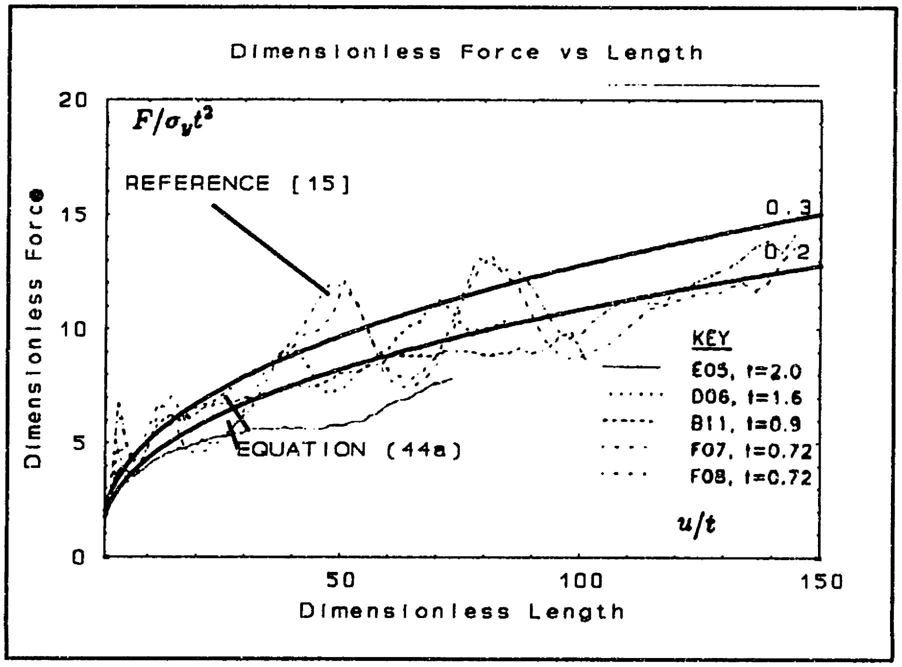

Figure 1.7 **Dimensionless force vs. length from present theory on top of experimental results from Reference [15]. (α=10° for experimental curves, μ=0.2 & 0.3 for theoretical curves.)**

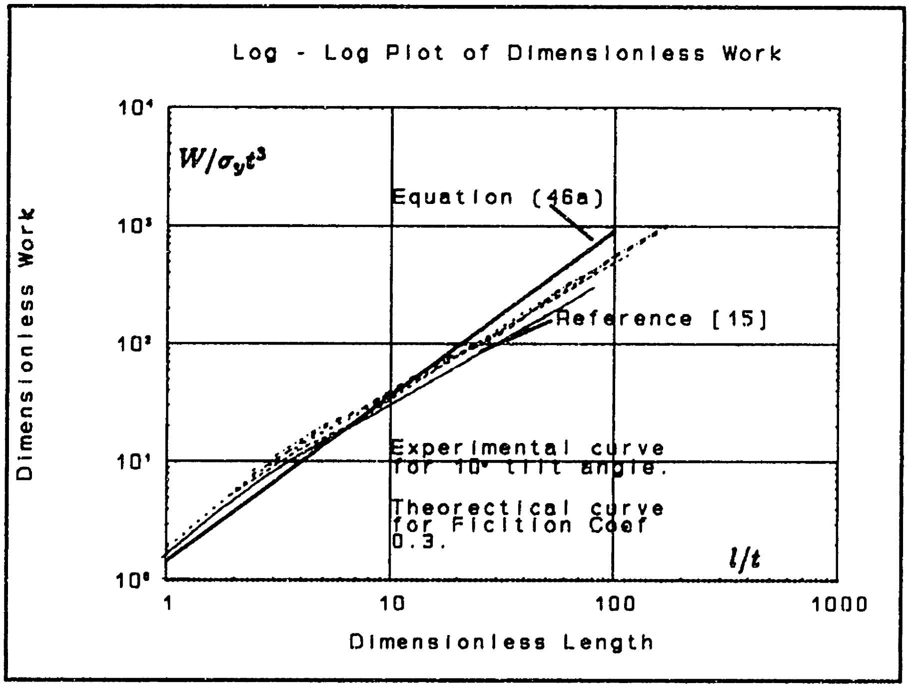

Figure 1.8 **Log-Log plot of dimensionless energy absorbed vs. length from theory on top of experimental results from Reference [15].**

Of course, since the constant C in Equation (1.40a) depends on both the friction coefficient and the dimensionless COD parameter, many combinations of $\overline{\delta}_t$ and μ will yield good correlation with the Lu and Calladine experiments. This is shown in Figure 1.8. In the absence of suitable experimental data the present analysis was conducted with $\overline{\delta}_t = 1$ and the friction coefficient was varied over the range $\mu = 0.1 - 0.4$. While this range of friction coefficient seems reasonable for steel to steel sliding contact based on numerous handbooks [30], more experimental data is needed to better determine both of these parameters.

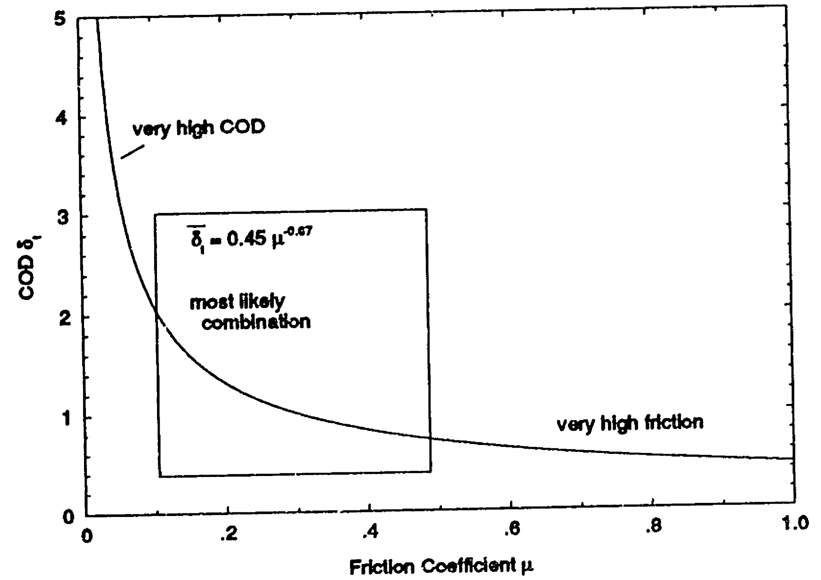

Figure 1.8. Combinations of μ and $\overline{\delta}_t$ which provide good correlation with experimental data of Reference [15].

One particularly important aspect for further experimental observation is the nature of the near-tip strain field and the crack geometry. Precise measurements are needed to validate or refute the assumption made in this analysis that the crack opening displacement parameter is constant throughout the cutting process, and to determine the size of the plastic membrane stretch zone. In the present formulation the near-tip membrane work is a function of the size of the plastic zone, and not of a material constant. As a result, the energy dissipated in the plastic zone increases with the cut length, specifically as $\ell^{0.4}$.

Atkins characterized the work contribution of the near-tip field by the "essential work of fracture" $\mathbf{R}_o = m\sigma_o\delta_t$, where $\mathbf{R}_o$ depends on tri-axiality [21]. This fracture parameter has been used in the past for steady state processes such as machining, tube inversion with splitting, or plate perforation by a constant width wedge. Initial plate indentation and cutting, however, is not a steady-state process (the resistance force is variable) and consequently $\mathbf{R}_o$ may or may not be constant. An important observation has been made here which may throw some light on this question. It has been shown that in addition to the far field flow (exclusively bending work) and crack tip flow (primarily membrane stretching) there is a third contribution in the so called "transition region" (double hatched area in Figure 1.2), which is characterized by combined bending and membrane stretching.

The principle of virtual work, Equation (1.2), is written by Atkins [21] in an alternative form,

$$Fdu = WdV + \mathbf{R}_0 dA \;, \tag{1.41}$$

where du, dV, and dA are respectively increment of wedge displacement, incremental volume of newly bent flaps, and increment of new surface, dA = t du. The statement of virtual work (1.42) is based on the premise that a clear distinction can be made between the near-tip and far fields, and here lies the major limitation of this particular approach. In the plate cutting process there is not any clear-cut boundary between these two fields because of the presence of the transition zone.

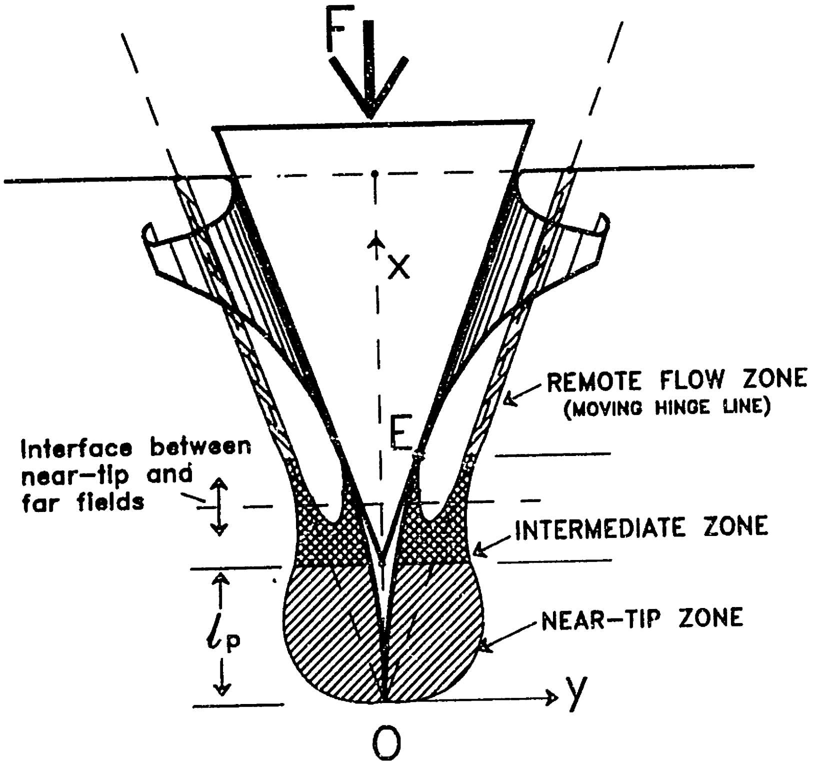

Figure 1.9. **Hypothetical boundaries of the plastically deforming zones in plate cutting experiments.**

This is illustrated in Figure 1.9, which shows the non-uniqueness of the position of the interface between the near-tip and remote fields. The work dissipated in the transition zone can be lumped together with either the near-tip or far-field work. In the present formulation this additional work is approximated and included in the calculation of the near-tip membrane work (as explained in Section 1.5). As a consequence, there is not a complete one-to-one correspondence between the $\dot{E}_m$ term in this formulation and the $\mathbb{R}_o dA$ term in Atkins' formulation, and not all of the membrane work can be identified with the work of fracture. This may explain why the work contribution of the near-tip field in our formulation is not a constant while it is sometimes taken to be [31].

The above discussion highlights the need for a better understanding of material resistance to cracking or cutting in terms of a more precise formulation of boundary conditions for the near-tip region from the remote field. Additional theoretical and experimental work is needed to establish the range of applicability of the hypothesis standing behind Equation (1.42).

One possible generalization of the present computational model is to introduce an additional free parameter to characterize the plate at the crack tip. In addition to the rolling radius, one could include, for example, the amount of lift w_t at the crack tip. This would allow minimization of the work functional over the space of two parameters (w_t, R), in much the same way as explained in Appendix A for the tube crushing problem. Such an approach could allow the size of the near tip plastic zone (or essential work to fracture) to be held constant, and the difficulty would then be shifted to the construction of the transition zone which connects the near-tip events with remote bending via ever increasing rolling radius.

III. Chapter 2

Plate Cutting Experiments and Formulation of the Steady State Problem

2.1 Introduction

When a plate is cut by a finite width wedge, the process involves two distinct stages; initiation, and steady state. During the initiation stage the cutting force increases with the length of the cut, as was described in Chapter One and observed experimentally by Lu and Calladine [15]. At some point, however, the cutting process which involves a finite width wedge must transition to steady state, and the cutting force will become constant. The length of the cut at the point that the transition to steady state occurs is defined here as the critical cut length, or critical length ℓ_{cr}. The objective of the plate cutting experiments reported in this chapter is twofold;

1. To verify the closed form solution derived in Chapter One for the force during the initiation stage, and

2. To determine the critical length at which the process transitions to the steady state stage so that a method of estimating the steady state

cutting force can be developed.

When a plate is cut by a "wide" wedge, the cylindrical flaps of the plate in the wake of the wedge may undergo transverse tearing at some characteristic interval due to longitudinal stretching, depending on the ductility of the material. A "narrow" wedge will stretch the plate as well, but not enough to tear it. This wide wedge mode has been observed in actual ship groundings, and a theoretical expression for the force to tear the plate transversely is derived in this chapter.

The literature on steady state plate cutting is virtually non-existent, but the research is vital to the development of a practical damage prediction model for ships in high energy groundings. The empirical formulations for plate cutting force of both Vaughan [40], and Lu and Calladine [15], are based on experiments which involve the initiation phase only. These experiments did not drive the wedge far enough into the plate to observe the transition to steady state. Lu and Calladine did report one steady state experiment, but they did not include the results of that experiment in their empirical analysis.

2.2 Theory

2.2.1 Steady State Plate Cutting Theory

During the initiation phase of the plate cutting process the radius of the flaps in the wake of the wedge grows with the cut length as described by Equation (1.25), and the flaps form at an angle equal to the wedge angle. At some point, however, the process transitions to steady state, and the flaps become constant radius parallel to the axis of the wedge. This hypothetical steady state cutting mode is shown in Figure 2.1. When the transition to steady state occurs, the cutting force becomes constant.

Common sense dictates that the process must transition to steady state, because for a finite width wedge the cutting force can not grow unbounded. At some point it takes more energy to continue to increase the radius of the flaps than to bend them parallel at a constant radius. The length of the cut at this point is the critical length.

As mentioned above, one of the primary objectives of the experiments reported here is to determine the critical length. Once the critical length ℓ_{cr} has been determined, the closed form solution developed in Chapter One can be used to estimate the constant steady state cutting force F_c by evaluating Equation (1.38) at $\ell = \ell_{cr}$;

$$F_c = 3.28\,\sigma_o\,(\bar{\delta}_t)^{0.6}\,\mu^{0.4}\,(\ell_{cr})^{0.4}\,t^{1.6}\ . \qquad (2.1)$$

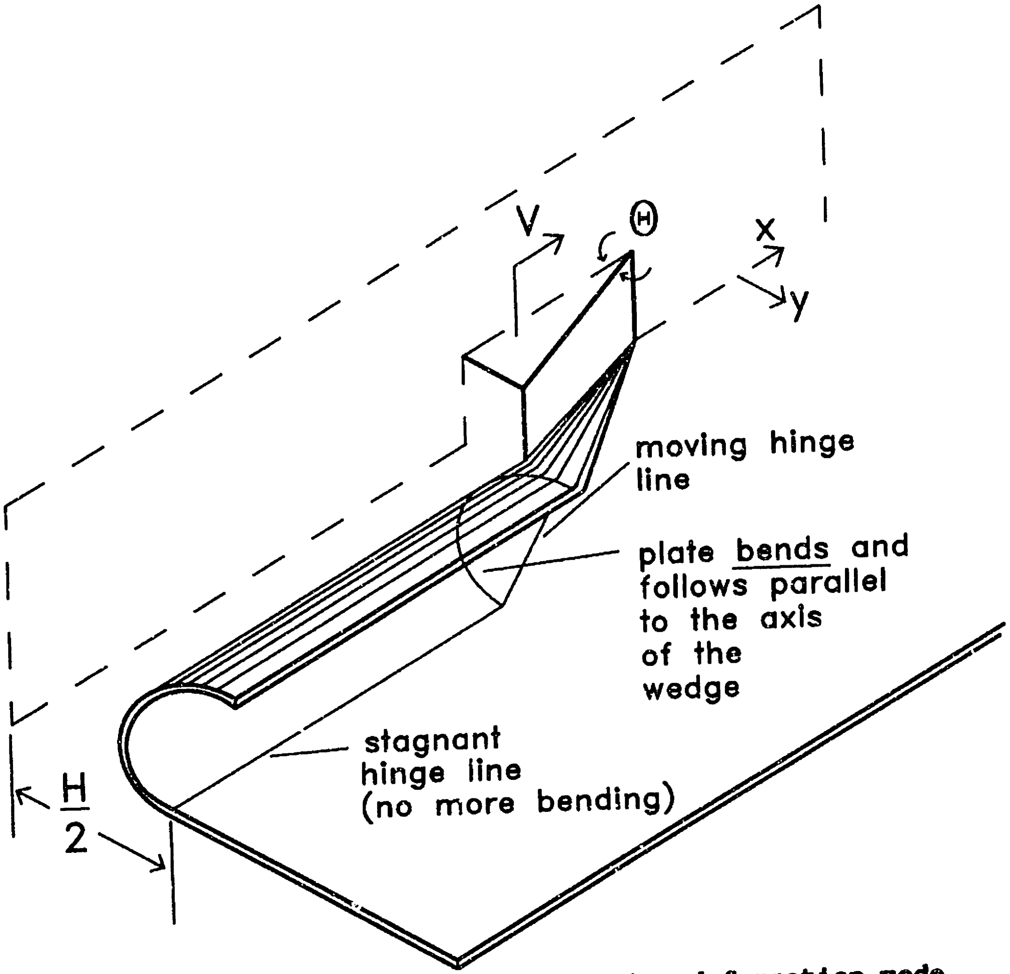

Figure 2.1 Steady state plate cutting deformation mode.

The transition to steady state is a complex geometrical and mathematical problem which involves a change of energy absorbing modes at a bifurcation point in the cutting process. As such, it is extremely difficult to formulate a closed form solution for the steady state cutting force. In fact, a secondary objective of these experiments is to simply observe the steady state mode in an effort to develop a kinematic model on which to base such an analysis. It can be theorized however, that the critical cut length at which the transition occurs is a function of the wedge geometry, and therefore can be defined as

$$\ell_{cr} \equiv r\,\ell^{*}\,, \tag{2.2}$$

where r (r ≥ 1) is an experimentally determined coefficient, and ℓ^{*} is the length of the cutting wedge from the tip to the mid point of the base (as shown in Figure 2.2). If r = 1, for example, the cutting process transitions to steady state after the wedge has traveled a distance into the plate equal to its own length. Substituting (2.2) into (2.1) the approximate expression for the steady state cutting force becomes

$$F_c = 3.28\,\sigma_o\,(\overline{\delta}_t)^{0.6}\,\mu^{0.4}\,(r\ell^{*})^{0.4}\,t^{1.6}\,. \tag{2.3}$$

In the one experiment reported by Lu and Calladine [15] which did reach steady state, the plot of cutting force vs. length appears to level out when the cut length is about equal to twice the wedge length. From this data alone, it may be reasonable to theorize that the coefficient r is of order 2. This seems to make sense intuitively since one would not expect the plate in the wake of the wedge to be spread much wider than the wedge itself before the transition to steady state occurs. If r were of order 10 for example, the wake width would be 10 times the wedge width when the transition occurred and the amount of energy involved in stretching and bending the plate flaps would be extreme. From this simple analysis, an experimental hypothesis is formed.

Hypothesis #1; The plate cutting process will transition to steady state

> when the cut length is approximately equal to twice the wedge length ℓ^*. The constant steady state plate cutting force can be estimate by Equation (2.3) with $r = 2$.

This hypothesis is fully confirmed by the series of plate cutting experiments using aluminum and steel plates to be described in Section 2.4.

2.2.2 Plate Tearing Theory

The closed form solution for the plate cutting force developed in Chapter One accounts for the transverse stretching of the plate in the near-tip region. In steady state cutting, however, the plate also undergoes longitudinal stretching in the far field region due to the angle at which the flaps are formed. If the cutting wedge is narrow enough, the plate flaps will stretch longitudinally and then bend parallel to the wedge axis as described above, and shown in Figure 2.1. In the narrow wedge case, the membrane energy involved in the longitudinal stretching is small. For a wider wedge, however, the longitudinal stretching exceeds the critical strain to rupture ε_{cr}, and the plate flaps will tear transversely at some characteristic interval λ. The wide wedge mode is shown in Figure 2.2a, where λ is the wave length at which the transverse tears occur along the length of the flaps.

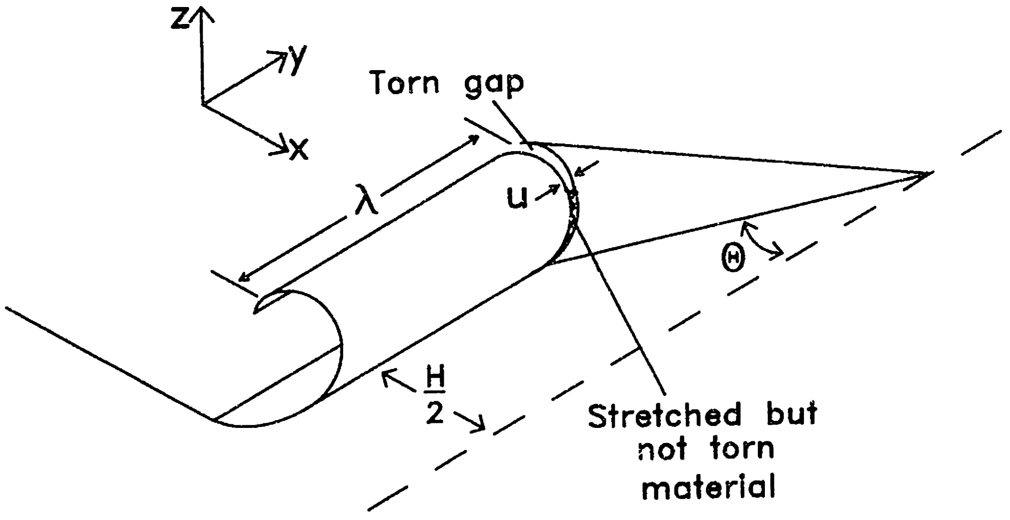

Figure 2.2a

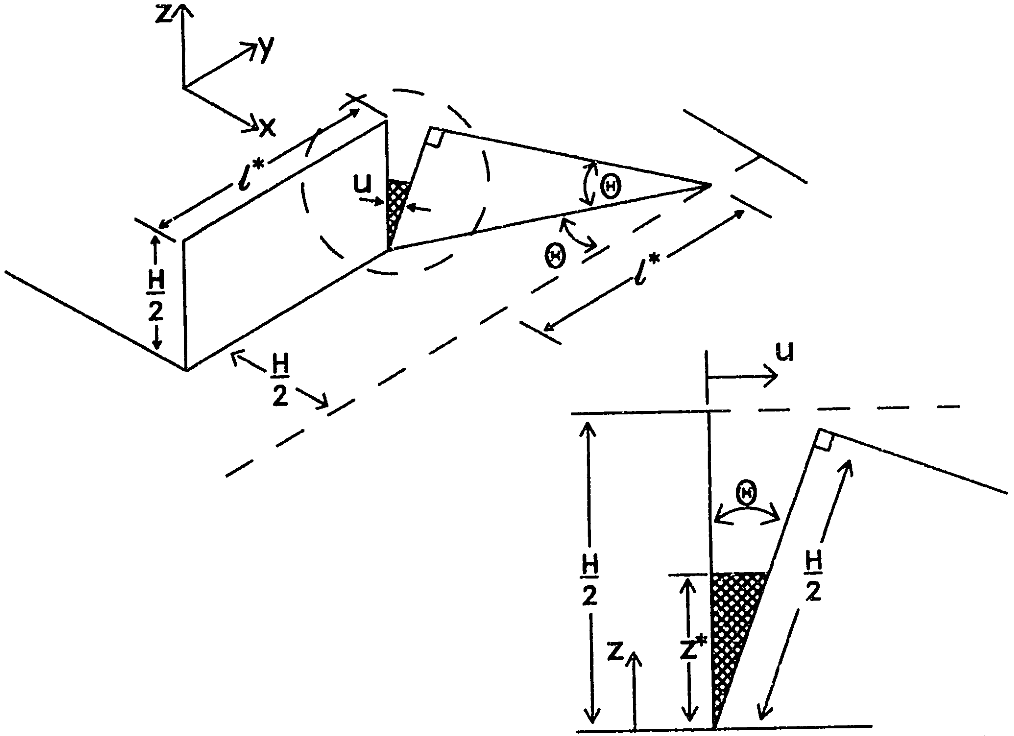

Figure 2.2 a) Transverse tearing of the plate flaps in the wake of a wide wedge. b) Idealized model of the plate tearing with detail of the torn gap.

The energy involved in tearing the flaps is significant, and the associated force must be accounted for. The force required to tear the flaps transversely is defined here as the plate tearing force, F_T. It must be added to the plate cutting force F_c in order to obtain the full solution for the wide wedge problem.

The solution for the plate tearing force generally follows Wierzbicki's tearing model [34] [35], and is very similar to the girder tearing solution presented in Appendix E. Figure 2.2b is the idealized model of the steady state, "wide wedge" deformation mode used in the following analysis. Notice that in the model the wave length λ has been chosen to be equal to the wedge length ℓ^*. There is some experimental evidence to indicate that the wave length (distance between transverse tears) is equal to the wedge length or some multiple thereof, but the exact value of λ is not critical because the distance over which the longitudinal straining takes place falls out of the solution, as will be shown later.

The force to tear the plate flaps can be found from the related membrane energy through the principle of virtual work;

$$F_T \ell^* = E_m \quad . \tag{2.4}$$

It is shown in [34] and [36] that the fracture energy at the tip of the transverse tear is an order of magnitude smaller than the membrane energy in the region around the tear, and accordingly the fracture energy has been left out of Equation (2.4). The bending energy term has also been left out of Equation (2.4) because there is no bending associated with the longitudinal stretching and transverse tearing of the flaps. The bending energy to form the flaps themselves has already been accounted for in the narrow wedge solution presented in Chapter 1.

In the plane strain rupture condition the membrane energy is given by;

$$E_m = t\int_S \sigma_o \epsilon_{cr}\, dS \,, \tag{2.5}$$

where the integral is taken over the torn area of the plate,

$$S = \lambda\left(\frac{H}{2} - z^*\right) . \tag{2.5a}$$

The integrated area, S, is shown in the insert of Figure 2.2b, which details the gap area of the flap. Notice that the tear does not extend all the way down the plate, but is assumed to start only at the point at which the longitudinal strain is equal to the critical strain to rupture, ε_{cr}. The role played by the material parameter ε_{cr} in this analysis is similar in concept to that of the COD in the analysis of the crack near the wedge tip discussed in Chapter One. Both are material parameters which are used to determine where the plate will separate.

The longitudinal strain in the plate flap can be found as a function of the distance z shown in Figure 2.2b;

$$\epsilon = \frac{u}{\lambda} = \frac{u}{\ell^*} = \frac{z\tan\theta}{\ell^*\cos\theta}\,, \tag{2.6}$$

where $u = z\tan\theta/\cos\theta$ is the distance at the gap area between the portion of the flap which is parallel to the axis of the wedge and the portion which follows the angle of the wedge, and λ has been assumed equal to ℓ^*. The point z^*, at which the strain is equal to critical strain to rupture and the plate flap begins to tear, is found by setting Equation (2.6) equal to ε_{cr};

$$z^* = \frac{\epsilon_{cr}\,\ell^* \cos\theta}{\tan\theta} \,. \tag{2.7}$$

From the geometry of the wedge,

$$\ell^* = \frac{H}{2\tan\theta}\,, \tag{2.8}$$

where H is the wedge width and θ is the wedge semi-angle. Substituting (2.8) into (2.7), the point at which the flap begins to tear can be found as a function of the wedge geometry,

$$z^* = \frac{\epsilon_{cr} H \cos\theta}{2\,(\tan\theta)^2} \,. \tag{2.9}$$

Equation (2.5) can now be restated with the appropriate limits of integration;

$$E_m = t\int_0^{\ell^*}\int_{z^*}^{\frac{H}{2}} \sigma_o \epsilon_{cr}\, dz\, dy \,. \tag{2.10}$$

Integrating (2.10) and simplifying, the final expression for the membrane every associated with tearing one flap is,

$$E_m = t\,\sigma_o \epsilon_{cr} \ell^* \left(\frac{H}{2}\right)\left[1 - \frac{\epsilon_{cr}\cos\theta}{(\tan\theta)^2}\right]. \qquad (2.11)$$

The tearing force is found by substituting (2.11) into (2.4) and eliminating the characteristic wave length (chosen to be ℓ^*) from both sides,

$$F_T = t\,\sigma_o \epsilon_{cr} \left(\frac{H}{2}\right)\left[1 - \frac{\epsilon_{cr}\cos\theta}{(\tan\theta)^2}\right]. \qquad (2.12)$$

Equation (2.12) is the force to tear one flap to the point z^*. Of course in steady state indentation of a wide wedge into a plate both flaps will tear, and the expression for the tearing force which must be added to the cutting force is;

$$F_T = t\,\sigma_o \epsilon_{cr} H\left[1 - \frac{\epsilon_{cr}\cos\theta}{(\tan\theta)^2}\right]. \qquad (2.13)$$

Equation (2.13) is similar in form to the tearing force used in by Wierzbicki et al. in [34] and [35], but it differs because that model assumed that the tear extends all the way down the flap, while the present analysis allows for some portion of the flap the stretch but not tear. Wierzbicki's model also assumed that plate tearing was the only significant energy absorbing mechanisms involved in steady state deformation of the plate, while the present theoretical analysis includes both plate cutting and plate tearing.

It is of interest to analyze Equation (2.9) further in order to determine when the plate flaps will tear, and when they will simply bend in one piece; i.e. what is the "narrow" wedge and what is the "wide" wedge? The flaps will not tear if the strain never reaches the critical value ε_{cr}. This will be the case when the critical distance z^* is equal the entire flap height (H/2) (see Figure E2). Setting Equation (2.9) equal to (H/2) and simplifying yields the condition for which no tearing will occur,

$$\frac{(\tan\theta)^2}{\cos\theta} = \epsilon_{cr} . \qquad (2.14)$$

From Equation (2.14) it is apparent that <u>the difference between a narrow wedge and a wide wedge is not a function of wedge width at all, but a function of the wedge semi-angle θ</u> and the material parameter ε_{cr}. Dropping the cosine term in the denominator of Equation (2.14), an approximate expression for the critical wedge angle can be found,

$$\theta_{cr} \approx \arctan(\sqrt{\epsilon_{cr}}) . \qquad (2.15)$$

Equation (2.15) gives a simple way to predict the occurrence of transverse tearing of the plate flaps in the wake of a wedge. Wedges with semi-angle $\theta < \theta_{cr}$ will not cause the tearing and therefore the tearing force given by (2.13) need not be added. This theoretical analysis leads to a second experimental hypothesis.

Hypothesis #2; The "wide wedge mode" will be observed when the wedge semi-angle $\theta \geq \theta_{cr} \approx \arctan(\sqrt{\varepsilon_{cr}})$. The additional force required to tear the plate flaps transversely can be approximated by Equation (2.13) so that the total force when a plate is cut by a wide wedge is the sum of the plate cutting force (2.3) and the plate tearing force (2.13).

2.3 Experimental Apparatus and Test Specimens

The experiments were designed to test the two hypotheses stated in the previous section. Tests specimens were mounted in a rigid frame and placed in an INSTRON model 8500 dynamic testing system. A wedge mounted on the crosshead of the machine was then driven through the plate at a constant speed, and the load and crosshead displacement and cutting force were automatically recorded. The apparatus is shown in Figure 2.3 below. Details of the frame and wedges are included in Appendix C.

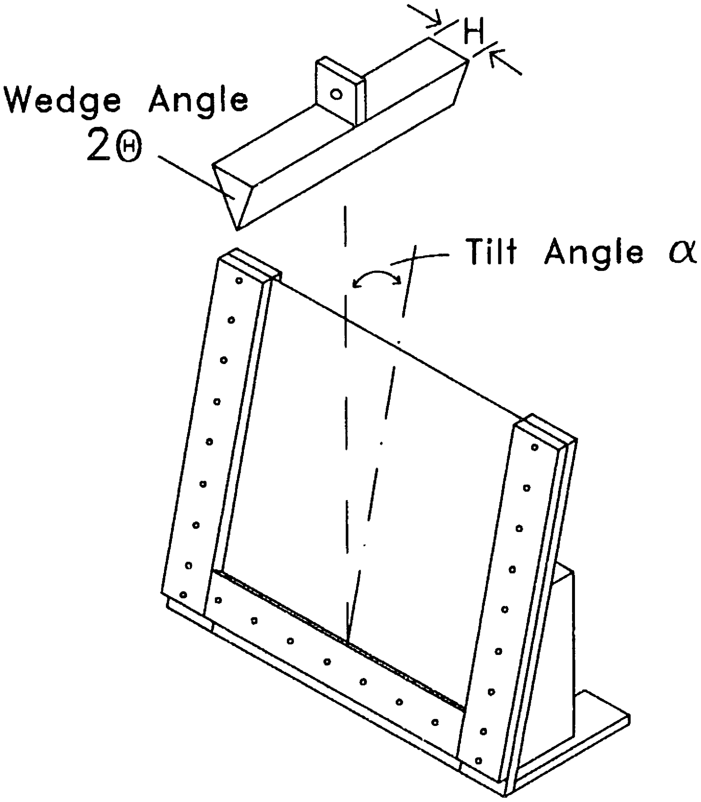

Figure 2.3 Apparatus used for steady state plate cutting experiments.

The frame was made from 1/2 inch thick, 2 inch wide mild steel plate, to hold a test specimen 19" by 16.5" (482.6mm x 419.1mm). The exposed section of test specimen was 14" x 14" (355.6mm square). The tests specimens were designed significantly larger than those used by Lu and Calladine [15] to allow the cutting process to reach steady state. Holes were drilled on the frame and the tests specimens to allow mounting with 1/4" bolts. The frame itself was mounted on an angled supports, which in turn mounted to the testing machine. Two sets of fixed angle supports were available, $\alpha = 10°$ and $\alpha = 20°$.

Three different cutting wedges made of cold rolled mild steel were used in the eight experiments reported here. The significant geometric characteristics of these wedges are summarized in Table 2.1 below. Construction details of the wedges are provided in Appendix C.

Table 2.1 **Characteristics of the Cutting Wedges Used**

Wedge #	**Semi-angle θ (deg)**	**Length ℓ^* (mm)**	**Width H (mm)**
1	20°	93	70
2	20°	100	75
3	30°	100	75

Table 2.2 **Test Specimen Specifications**

Specimen #	Material	Thickness t (mm)	σ_o (MPa)
5	3003 AL	0.7937	114.5
1	3003 AL	1.5875	113
7	3003 AL	0.7937	113.25
2	3003 AL	1.5875	114.25
13	ASTM A366	1.94	228
19	ASTM A366	2.00	225.5
14	ASTM A366	1.97	228
20	ASTM A366	2.00	226

***NOTE: Specimen numbers correspond with the full list of test specimens provided in Appendix D.**

The test specimens were aluminum and mild steel plate cut to size from larger sheets. The aluminum specimens were 3003 alloy, 1/16" and 1/32" nominal thickness. The steel specimens were ASTM A366 Grade C cold rolled structural carbon steel, 16 gauge and 14 gauge nominal thickness. The actual thicknesses of each specimen was measured by micrometer. Each specimen was drilled to fit the mounting frame and slotted to 1/4" depth in the middle of the upper edge to facilitate initiation of the cutting process. The specifications for the eight specimens used in the tests reported here are provided in Table 2.2.

The yield strength of each specimen was determined using Brinell Hardness for the aluminum specimens [ASTM E10-61T], and by the Rockwell Method for the steel specimens [ASTM E18-61].

Each experiment was conducted with a crosshead displacement rate of 20 mm/min and a data sampling rate of 1 point/sec. Forces were measured in kilo-newtons using a 100 kN load cell. The stroke of the testing machine was limited to 100mm, so that each specimen had to be cut in three consecutive strokes. No attempt was made to lubricate the cutting wedges, and the values for friction coefficient used in the following calculation were chosen to be consistent with common practice [30].

2.4 Representative Test Results

Table 2.3 lists the conditions under which each test was conducted. The eight experiments reported here involved two different wedge semi-angles, three wedge lengths, four plate thicknesses, and two materials. Only one tilt angle, $\alpha = 20°$, was tested.

Table 2.3 Test Conditions

Test #	**Specimen #**	**Wedge #**	**Figure #**
1	5	1	2.4
2	1	1	2.5
3	2	3	2.6
4	7	3	2.7
5	13	2	2.8
6	19	2	2.9
7	14	3	2.10
8	20	3	2.11

**NOTE: All tests were conducted at* $\alpha = 20°$

Test #1 (AL, $\theta = 20°$, $\ell^* = 93$ mm, $t = 0.794$ mm)

The results of Test #1 are shown in Figures 2.4 and 2.5. This is the test condition for which the kinematic model of Chapter One was developed, and which most closely matches the previous plate cutting work of Vaughan [7], and Lu and Calladine [15]. The first part of the plot, labeled OA, is the initiation portion of the cutting process during which the force increases with length. This looks very similar to the results presented in [15] for a mild steel plate under the same conditions. During this phase the flaps in the wake of the wedge continued to form at an angle equal to the wedge angle, and the radius of the flaps increased with cut length as expected. Equation (1.38) is also shown in Figure 2.4. It generally follows the trace of the experimental data throughout the initiation portion of the process. The values of μ and $\overline{\delta}_t$ used in plotting Equation (1.38) were chosen to be 0.2 and 1.0 respectively. These values are used consistently throughout this section of the paper.

The second part of the trace, AB, is the steady state portion of the process. The cutting force no longer increases with length, but remains essentially constant as the wedge continues to penetrate the plate. Notice that the process appears to transition to steady state shortly after the cut length is equal to twice the wedge length ($r = 2$). Notice too, that Equation (1.38) gives a good estimate of the steady state cutting force when evaluated at $\ell = 2\ell^*$. This is shown by the plot of Equation (2.3) with $r = 2$.

This particular test specimen showed the most obvious transition to steady state in terms of physical kinematics. When the cutting wedge was about 200 mm (or twice its length) into the plate, the flaps noticeably began to bend, to be parallel to the axis of the wedge rather than remain at 40°. The parallel flaps can be seen in the photograph of Figure 2.5. The transition to steady state was gradual, and continued throughout the remainder of the experiment.

As the wedge approached the bottom of the test specimen, and the lower edge of the support frame, the cutting force increased sharply, and the plate appeared to begin buckling ahead of the wedge tip. This was caused by the rigid boundary condition at the bottom edge of the plate, which interfered with the cutting process. As a result, the trace was stopped at ℓ = 300 mm.

Test #2 (AL, $\theta = 20°$, $\ell^* = 93$ mm, t = 1.587 mm)

Test #2 is identical to Test #1 except that the specimen is twice the thickness. The results are shown in Figures 2.6 and 2.7. Again, the portion OA of the plot is the initiation phase of the cutting process, and AB is the steady state phase. Notice that the process appears to transition to steady state about when ℓ = 200 mm (again, slightly after $\ell = 2\ell^*$), and that Equation (2.3) evaluated at r = 2 gives a good estimate of the steady state cutting force.

The photograph of Figure 2.7 shows that the flaps of the plate did begin to bend parallel to the axis of the wedge, but not as noticeably as in Test #1.

Test #3 (AL, $\theta = 30°$, $\ell^* = 65$ mm, t = 1.587 mm)

This test involves a wedge angle ($\theta = 30°$) greater than any reported in previous plate cutting experiments [2] [7] [15]. It was intended to induce the "wide wedge" mode described in Section 2.2. The results are shown in Figures 2.8 and 2.9.

Figure 2.8 shows that the trace of the cutting force during initiation is much flatter when $\theta = 30°$, than when $\theta = 20°$. It will be shown that this result is consistent for all of the tests involving the 30° wedge. As a result, Equation (1.38) does not follow the experimental trace as well here, as in the tests involving the 20° wedge. This is understandable, since the theory of Chapter One was developed from the experimental results of [15], which do not include any wedges with $\theta > 20°$. As a result Equation (1.38) is most applicable within the range $10° < \theta < 20°$. Figure 2.8 shows, however, that Equation (1.38) does provide a good estimate for the cutting force during initiation even for larger wedge angles.

Despite its flat nature during the initiation phase, the experimental trace of Figure 2.8 shows a definite transition to steady state, this time just before the cut length is twice the wedge length. Equation (2.3) evaluated at $r = 2$, gives an estimate of the steady state cutting force which is approximately 11% higher than the actual recorded force. Again, the theoretical curve is computed using a coefficient of friction $\mu = 0.2$ for consistency. If a value of $\mu = 0.15$ is used instead, Equation (2.3) falls right on the experimental trace at $\ell = 2\ell^*$.

Figure 2.8 also shows that the boundary effects caused by the support frame are observed much sooner in the process when $\theta = 30°$ than when $\theta = 20°$. In this case it is the sides of the frame, not the bottom, which interfere with the cutting process. As the wedge travels through the plate the moving hinge lines in the center of the flaps migrates toward the edges of the plate. At some point the ends of the hinge furthest from the origin of the cut reach the sides of the frame, and can go no further. When this happens the flaps of the plate near the tip of the wedge begin to knuckle, and the force increases sharply as shown in Figure 2.8. The knuckle that forms can be seen in the photograph of Figure 2.9. The other tests involving the 30° wedge were stopped before this knuckle became obvious.

The "wide wedge" mode, which includes transverse tearing of the flaps, was not observed during this test. This is understandable, since the 3003 aluminum is quite ductile and the critical strain to rupture, ε_{cr}, is very high (approximately 0.6). No tests were conducted to determine the value of ε_{cr} for this material.

Test #4 (AL, $\theta = 30°$, $\ell^* = 65$ mm, t= 0.794 mm)

Test #4 is identical to Test #3 except that smaller plate is used. The results are shown in Figures 2.10 and 2.11. The same general trends are observed. The initiation phase of the process has a flatter trace, but is still adequately described by Equation (1.38). The transition to steady state appears to occur slightly before $\ell = 2\ell^*$, and Equation (2.3) evaluated with r = 2 gives an estimate for the steady state force which is approximately 11% higher than that observed experimentally. Again, the plate tearing associated with a wide wedge was not observed.

Test #5 (Steel, $\theta = 30°$, $\ell^* = 65$ mm, $t = 1.47$ mm)

Test #5 involved steel plate, and there were some obvious physical differences from the tests on aluminum plate observed during the experiments. The amount of lift in the near-tip zone was significantly less in the steel plate than in the aluminum plate. As a result the direction of crack propagation at the wedge tip was more along the axis of the wedge. In the aluminum plate, the lift at the wedge tip was so pronounced that the crack actually propagated down into the plate, in a direction perpendicular to the undisturbed surface. In the steel plate the lift was much less significant, and the crack ran mostly along the same axis as the undisturbed plate. The difference in the degree of lift can best be seen by comparing the photograph of Figure 2.5 with the photograph of Figure 2.19.

The cut edge of the aluminum plate was bent along the length of the flap about a line parallel to, and about 2 mm away from, the axis of symmetry (center of the wedge). The edge also showed obvious signs of thinning and stretching. The same was not true with the steel plate. In the steel specimens, flaps in the wake of the plate remained cylindrical and smooth all the way to the cut edge, they did not have the extra bend in them. While there was some thinning of the steel plate near the cut edge, it was much less pronounced, and more difficult to detect. The cut edge of the steel plate did have an obvious bevel caused by the motion of the wedge, which was not apparent in the aluminum specimens.

Finally, although the force traces for all of the steel specimens indicate that the process did transition to steady state, the transition was much more difficult to detect by simply watching the kinematics. It was not apparent during the experiments that the flaps of the steel plate were bending to become parallel to the wedge axis, although subsequent measurement of the cut specimens indicate that this bending did actually begin.

Figures 2.12 and 2.13 show the results of Test #5. The general trends are the same as for the aluminum plate. Equation (1.38) adequately describes the initiation phase, the transition to steady state appears to occur slightly after $\ell = 2\ell^*$, and Equation (2.3) evaluated with $r = 2$ gives a good estimate of the steady state cutting force. The transverse tearing of the plate flaps described in Section 2.2 was not observed, despite the fact the $\theta = 30°$.

Test #6 (Steel, $\theta = 30°$, $\ell^* = 65$ mm, $t = 2.0$ mm)

This test condition is the same as Test #5 but the steel plate is thicker. The results are shown in Figures 2.14 and 2.15. In this case, the cutting process appears to transition to steady state when $\ell = 160$ mm, or about $2.5\ell^*$. Equation

(2.3) evaluated with $r = 2$ under-predicts the actual steady state cutting force by about 10.5%. Again, transverse tearing of the flaps was not observed.

Test #7 (Steel, $\theta = 20°$, $\ell^* = 100$ mm, $t = 1.47$ mm)

Test #7 used wedge #3, which has a 20° angle, but a longer length ($\ell^* = 100$ mm) than the 20° wedge used with the aluminum specimens. The results are shown in Figures 2.16 and 2.17. It is difficult to tell from the trace exactly where the transition to steady state occurs, but it is apparent that the critical length is approximately equal to $2\ell^*$, and that Equation (2.3) evaluated with $r = 2$ gives a good estimate of the steady state cutting force.

Equation (1.38) does not follow the experimental trace of the initiation portion of the curve (OA) as well in this case, as it did for the 20° wedge in the tests with aluminum. One possible explanation for this is that the 1/4 inch slit at the top of the plate, which is provided to enhance initiation, was not pre-cut straight. As a result, the wedge turned slightly as it entered the plate, and the cut was non-symmetric. Lu and Calladine [15] observed this same result when they introduced a small rotation angle β, which caused the cutting edge of the wedge to be non-perpendicular to the surface of the plate.

Test #8 (Steel, $\theta = 20°$, $\ell^* = 100$ mm, $t = 2.0$ mm)

Test #8 is identical to Test #7, but with the thicker steel plate. The results are very similar, and are shown in Figures 2.18 and 2.19. The transition to steady state appears to occur just about when $\ell = 2\ell^*$, and Equation (2.3) overestimates the steady state force by less than 5%. This particular cut was unique because the wedge removed a strip of plate material equal in width to the width of the wedge tip (about 1 mm) as it cut the plate. The strip can be seen in the photograph of Figure 2.19. In every other test, the material directly in front of the wedge was stretched transversely until it tore, approximately in the middle of the very narrow region at wedge tip. In Test #8 the plate tore in two places, on either side of the wedge tip, and the narrow strip was removed. It is interesting that this different cutting mode did not result in a significant change if the cutting force, and it supports the claim made in Chapter One that any kinematically compatible model of the cutting process will yield a good approximate expression for the force.

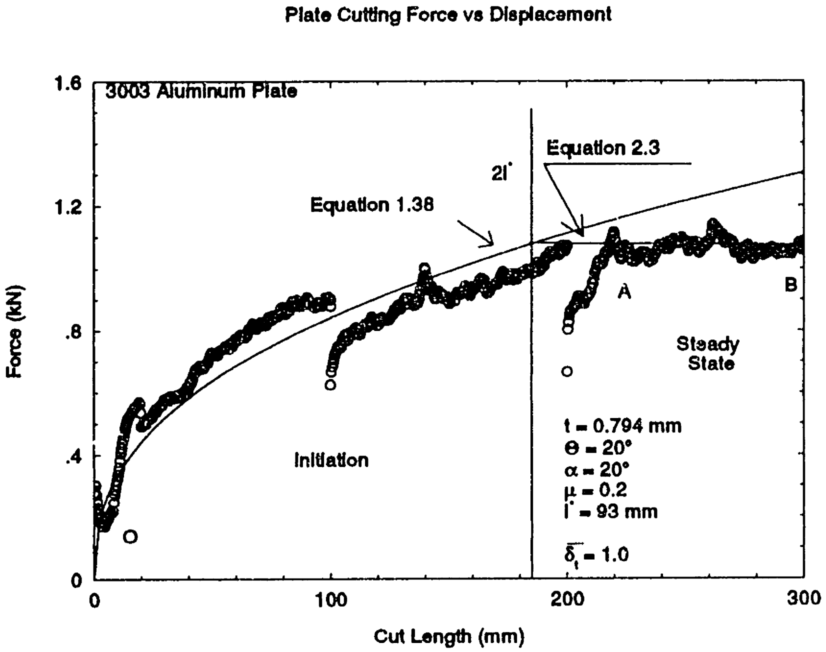

Figure 2.4 Test #1 results.

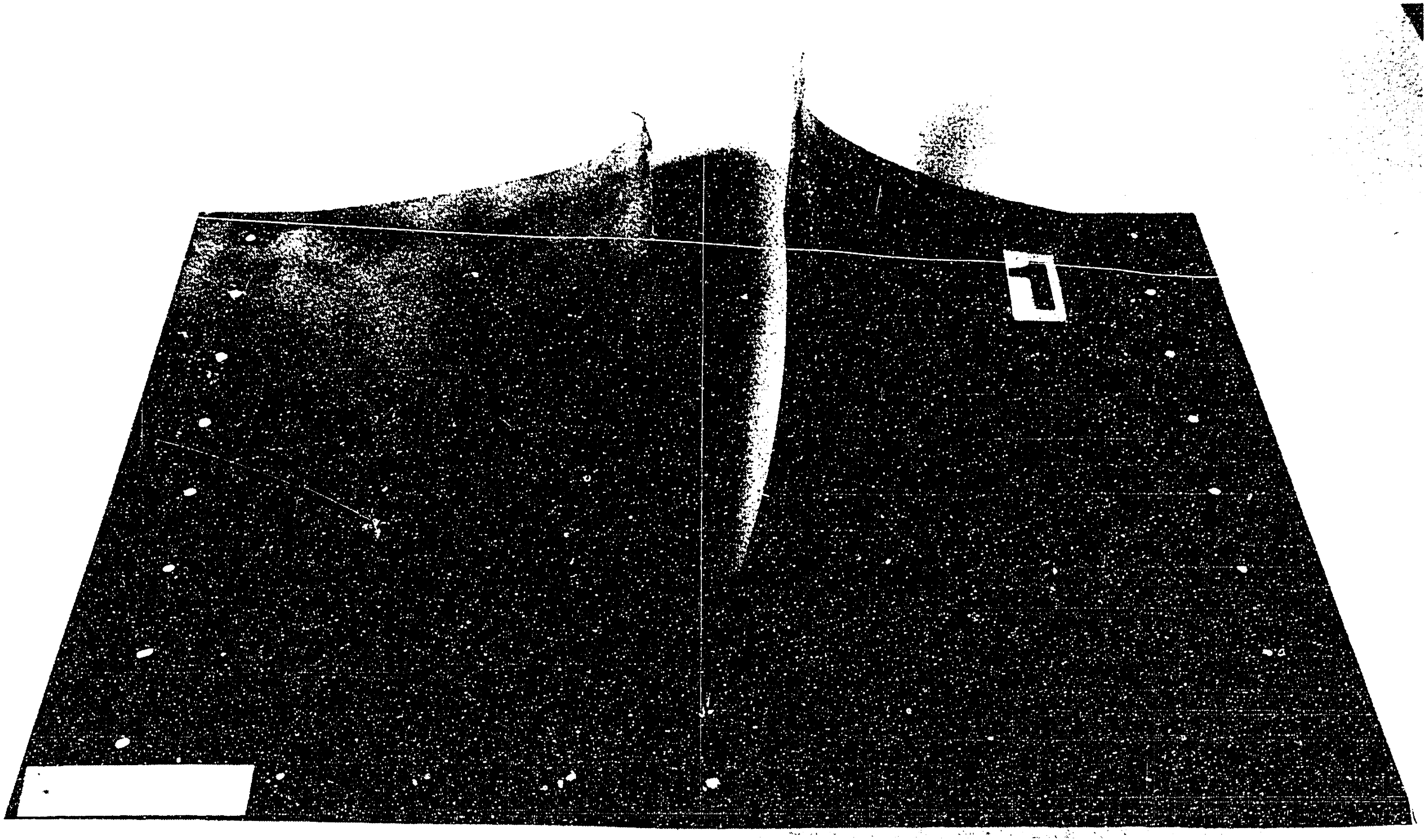

Figure 2.5 Test #1 speicmen photograph.

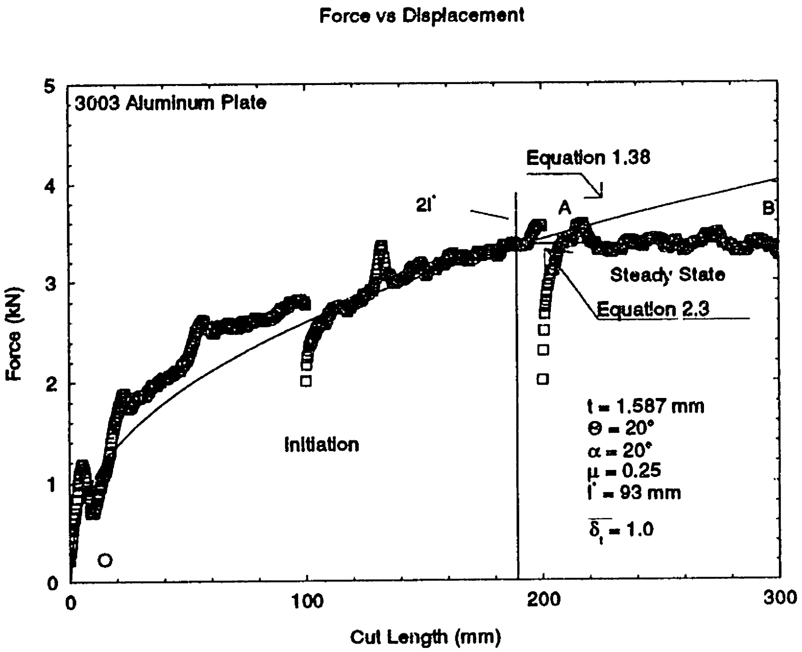

Figure 2.6 Test #2 results.

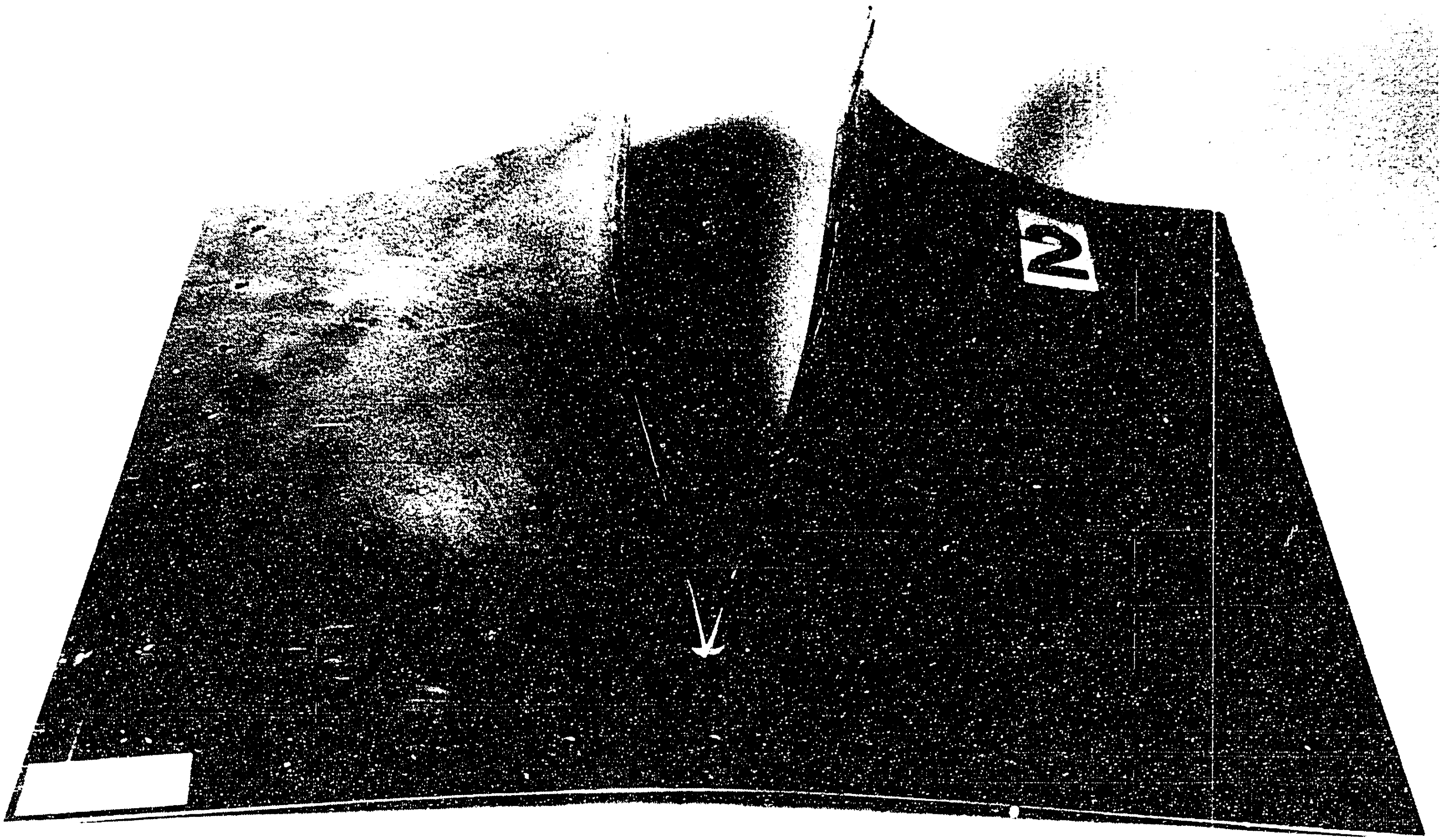

Figure 2.7 Test #2 specimen photograph.

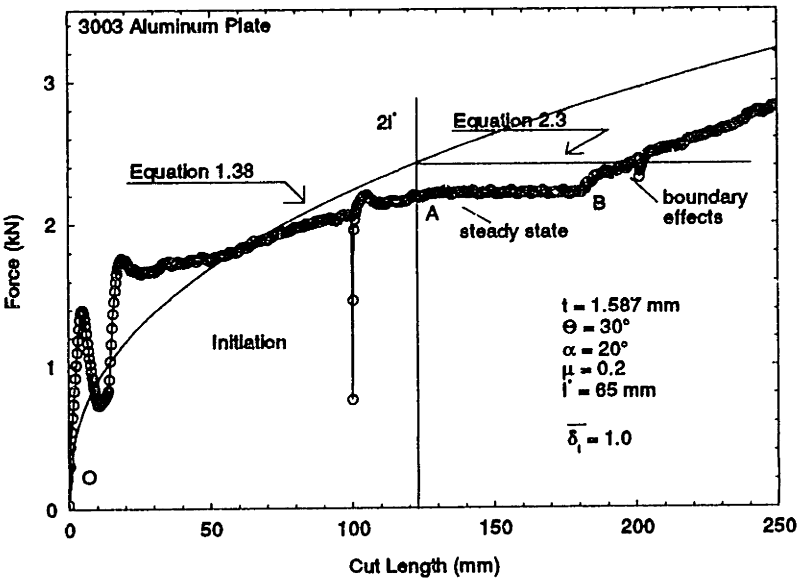

Figure 2.8 Test #3 results.

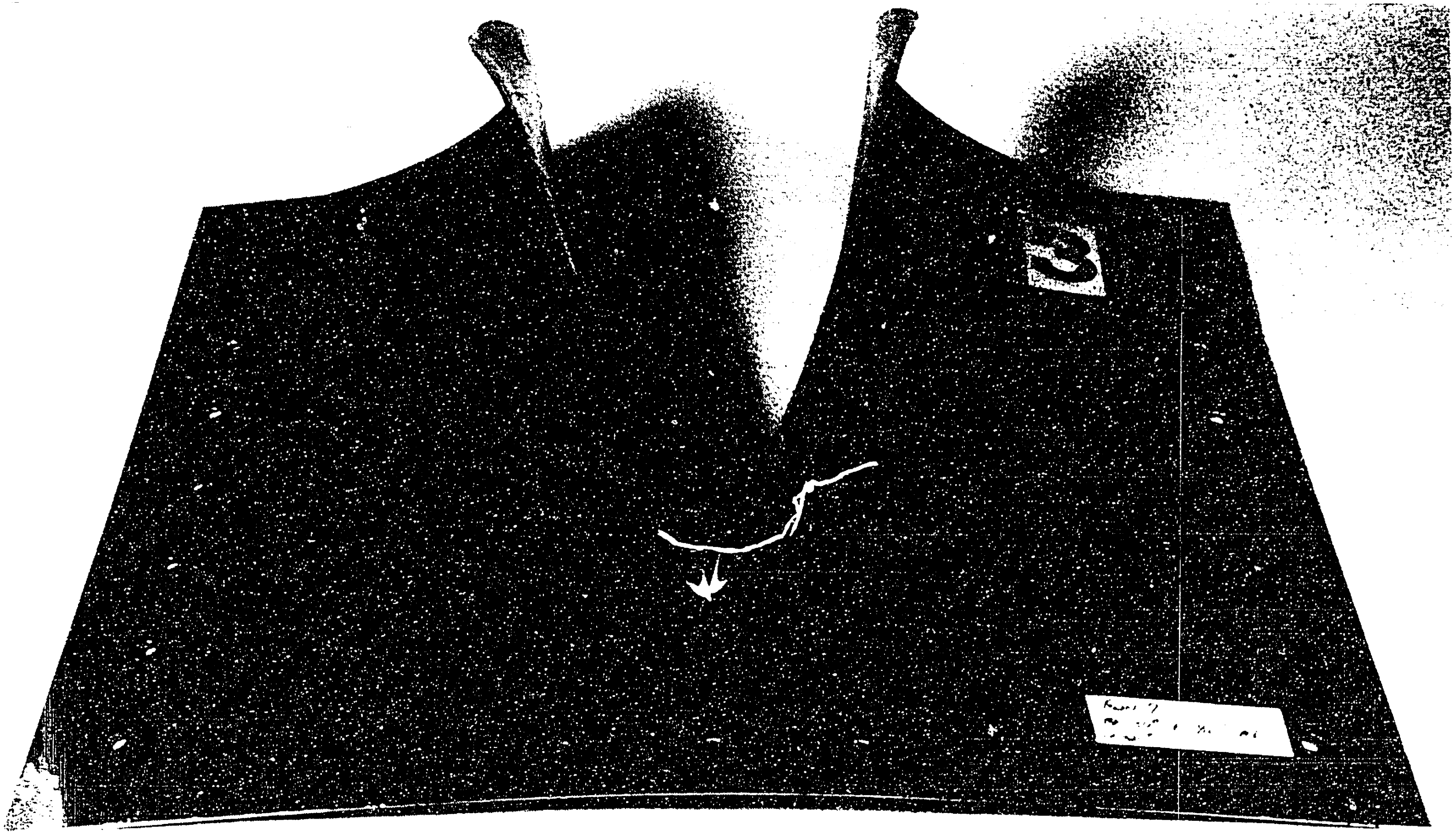

Figure 2.9 Test #3 specimen photograph.

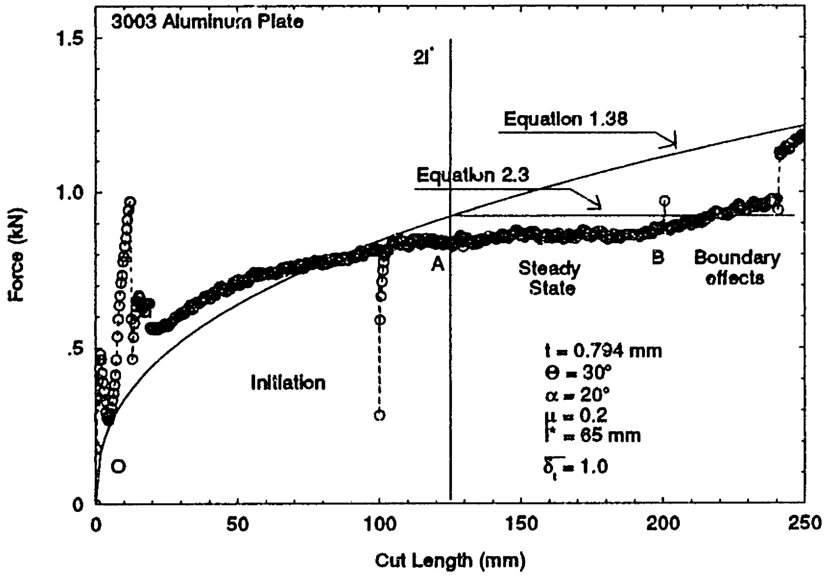

Figure 2.10 Test #4 results.

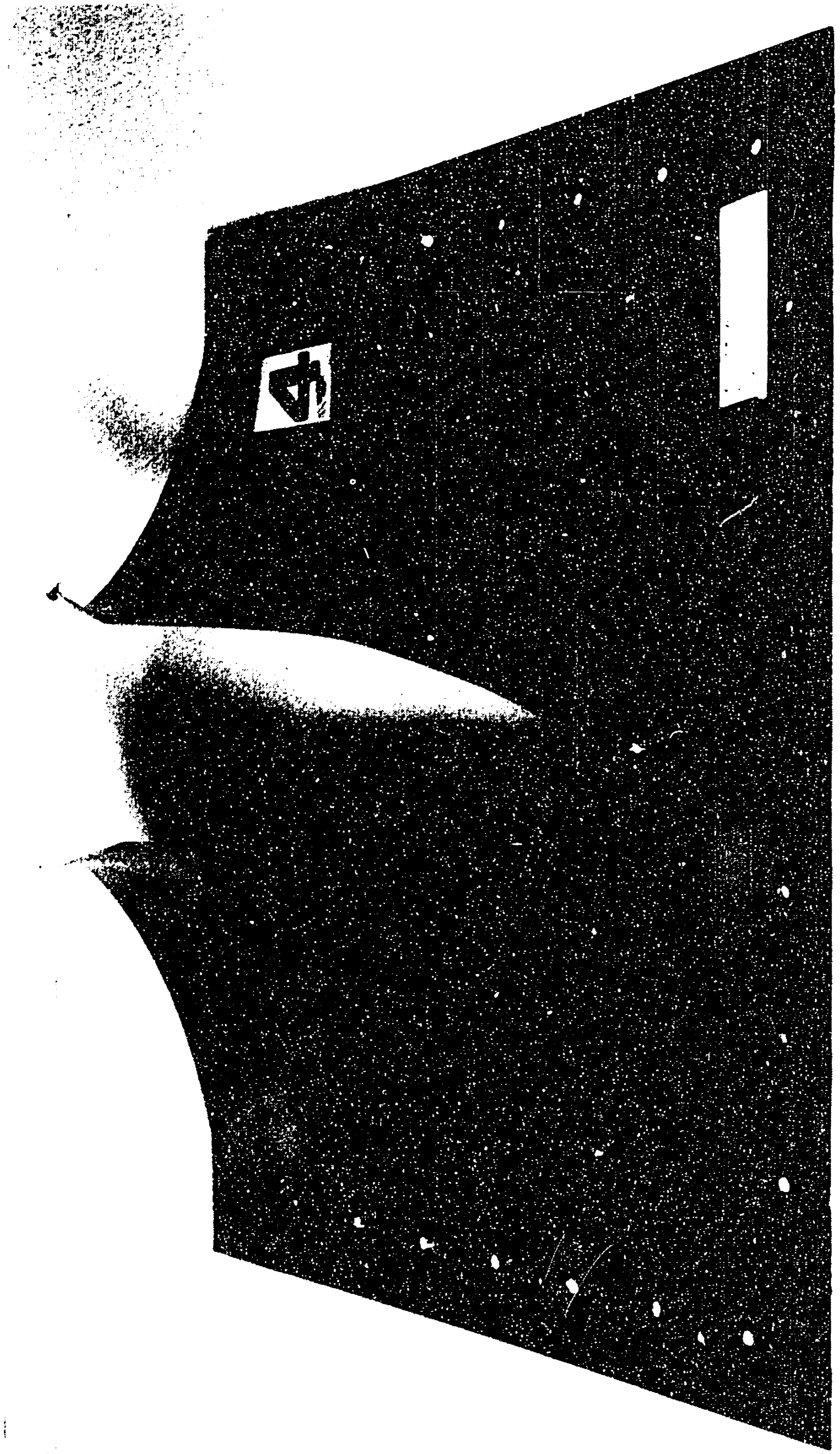

Figure 2.11 Specimen #4 photograph.

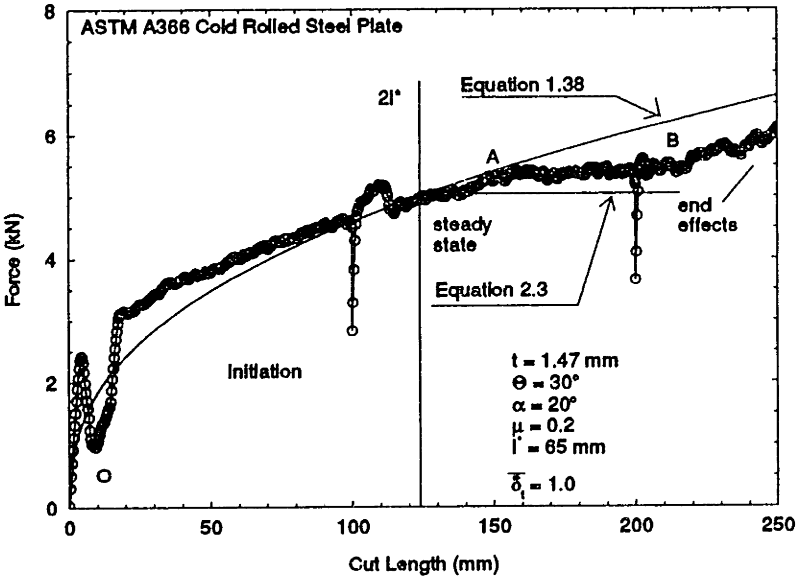

Figure 2.12 Test #5 results.

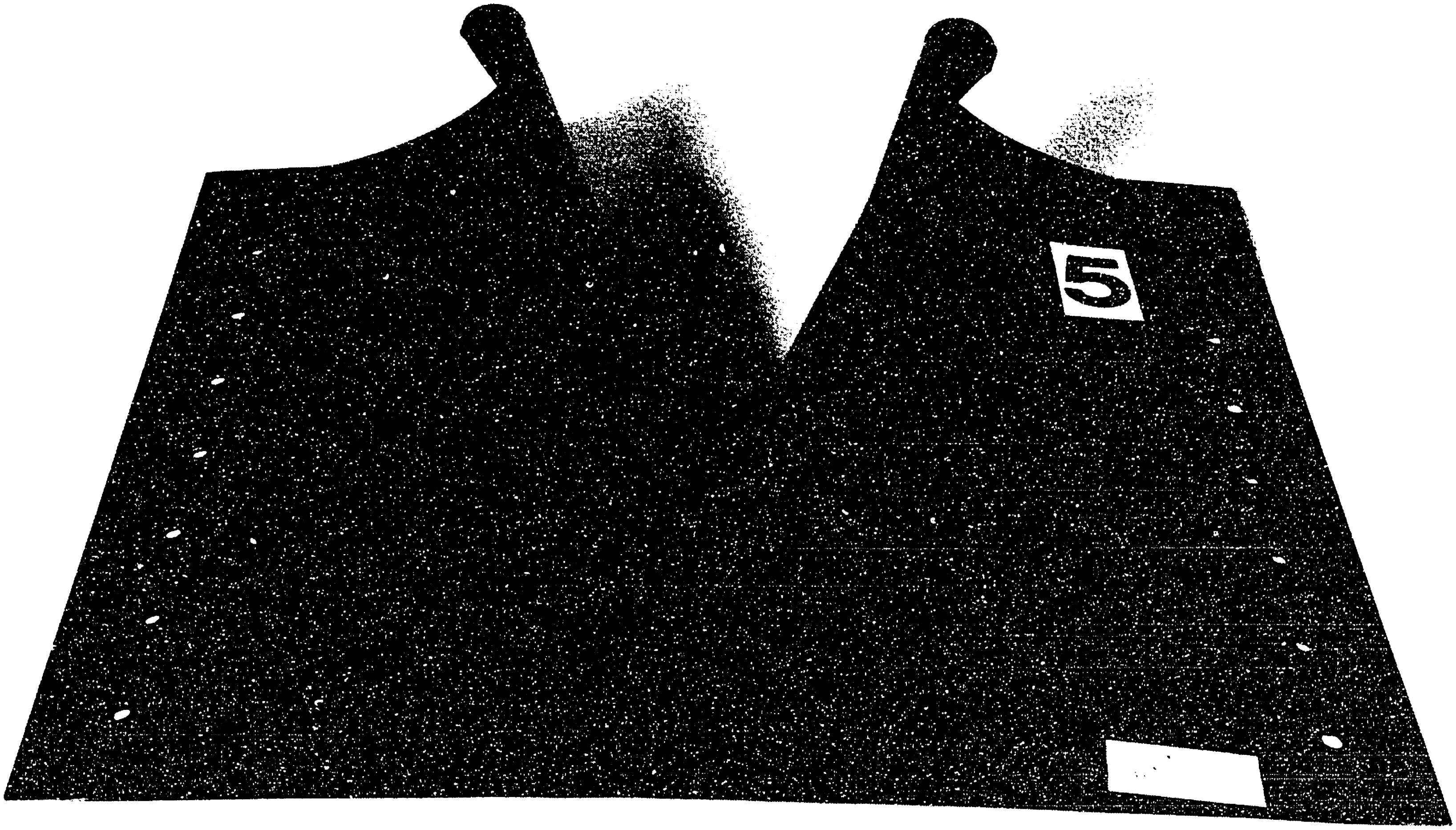

Figure 2.13 Test #5 specimen photograph.

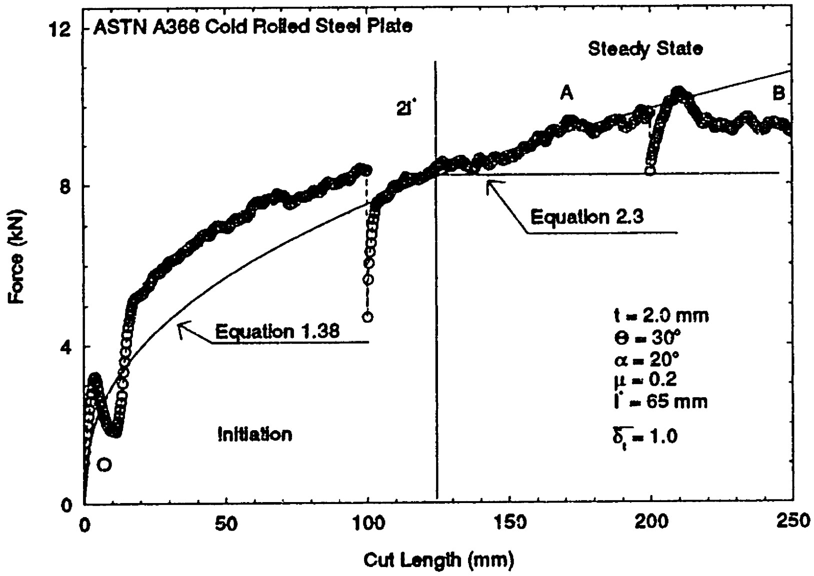

Figure 2.14 Test #6 results.

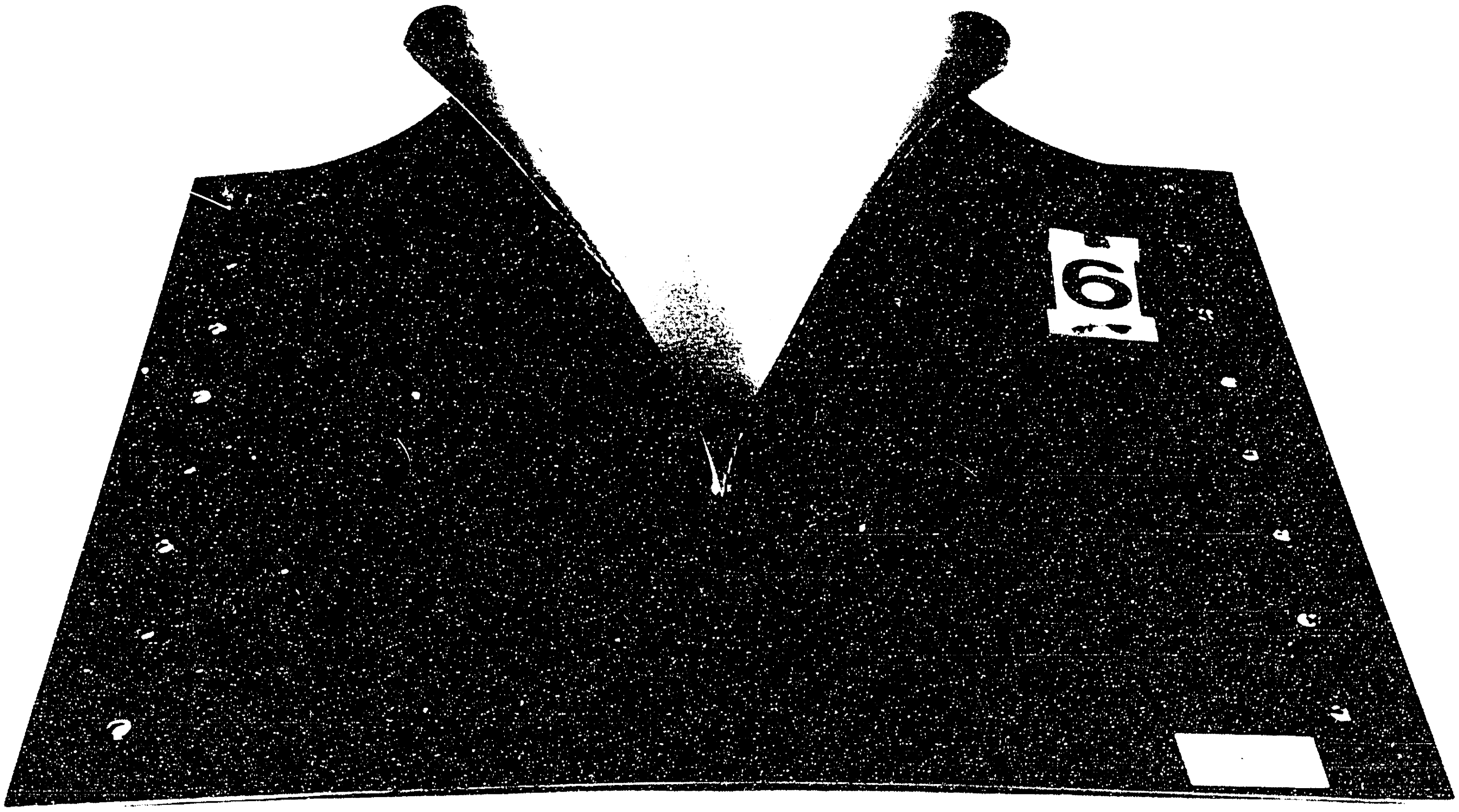

Figure 2.15 Test #6 specimen photograph.

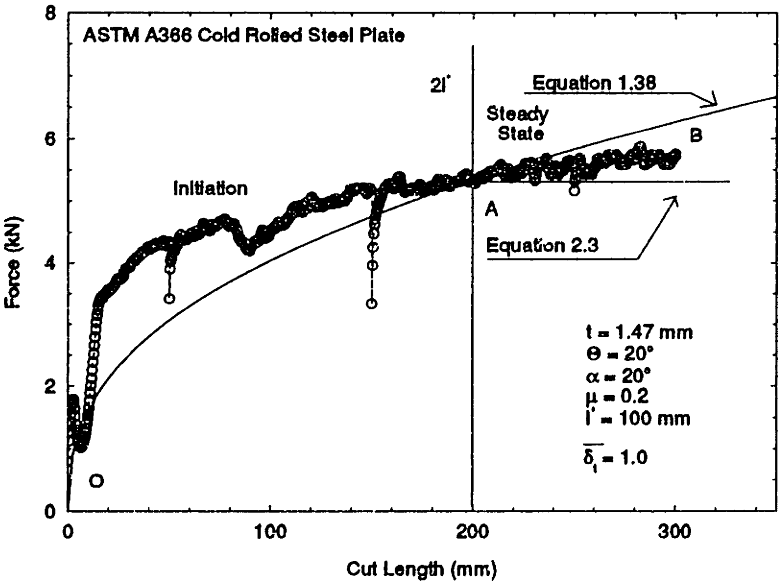

Figure 2.16 Test #7 results.

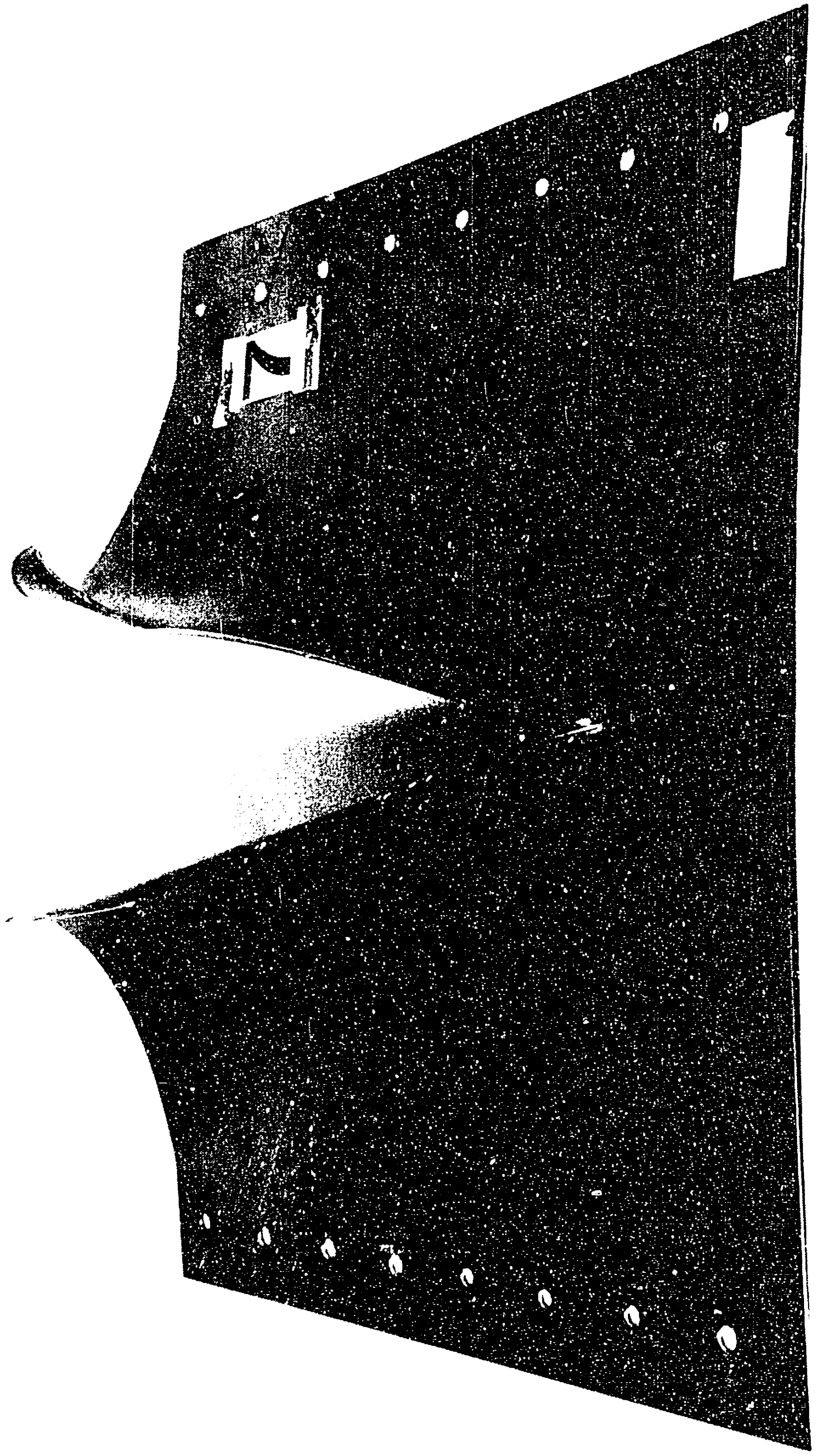

Figure 2.17 Test #7 specimen photograph.

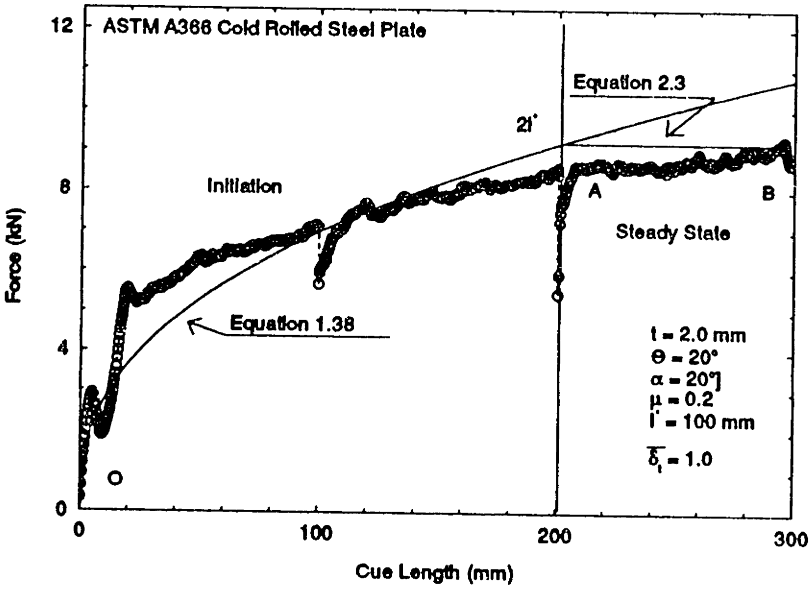

Figure 2.18 Test #8 results.

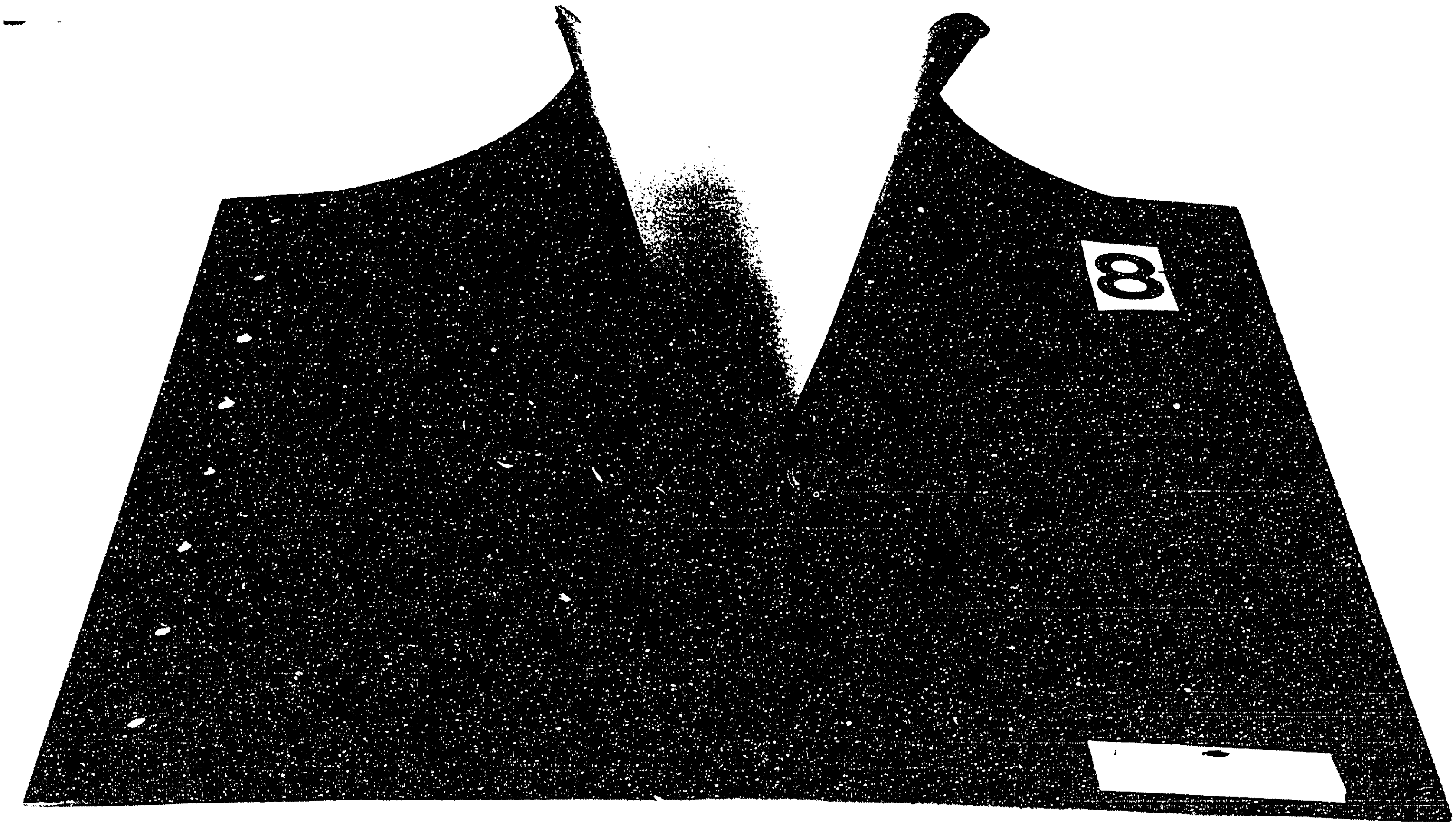

Figure 2.19 Test #8 specimen photograph.

2.5 Discussion

2.5.1 Initiation of Plate Cutting

One of the primary objectives of the plate cutting tests was to confirm the theoretical analysis of the initiation portion of the plate cutting process presented in Chapter One. Confirmation is accomplished in two ways: 1) comparison of the closed form solution for the cutting force (Equation (1.38)) with the experimental data, and 2) validation of the major assumptions made in constructing the kinematic model used in Chapter One, through observation of the actual kinematics of the cutting process.

The test results (Figures 2.4 - 2.12) show that Equation (1.38) yields a very good approximation of the actual cutting force during initiation, throughout the range of plate thicknesses, wedge angles, and materials tested. In general, Equation (1.38) seems to describe the tests which involve a 20° semi-angle wedge better than those with the 30° semi-angle wedge. As noted earlier, this is to be expected since the kinematic model used in the derivation of Equation (1.38) is based on previous experiments using narrow wedges, $\theta < 20°$, only. It is shown in Chapter One that the closed form solution is most applicable within the range $10° \leq \theta \leq 20°$, but these tests results indicate that Equation (1.38) is adequate for wedge semi-angles up to 30° as well.

Nearly every major feature of the kinematic model proposed in Section 1.3 was observed during the plate cutting tests. The photographs of Figures 2.20 and 2.21 are of the specimen used in Test #6, taken from behind (looking in the direction of the wedge motion) and from the side (perpendicular to the axis of symmetry). The flaps of the cut plate in the wake of the wedge can be seen in these photographs to be inclined cylinders with helical cross-sections, not variable radius cones. Accordingly, the cut edge of the plate formed a modified helical line, and touched the wedge at only one location, as theorized in Figure 1.1.

The plastic hinge line in the center of the cylindrical flaps could be seen moving outward as the wedge progressed downward into the plate. In fact, as explained earlier, some of the tests were limited in duration (cut length) because when the end of the moving hinge line furthest from the wedge tip reached the side of the support frame the deformation mode changed, and the cutting force increased sharply. This result may be significant for the application of these experiments to ship grounding, because it indicates that when a stiffened plate is cut by a wedge the deformation mode can be quite different. A plate of infinite width will allow the flaps to grow unrestricted (during initiation) in a manner that will result in minimum required cutting force. When the plate is rigid at its boundaries, however, the kinematics of the problem will change at some point as the hinge lines approach the boundaries. At that point, the closed form solution of Chapter One is no longer applicable. Of course, interference will only happen in the stiffened plate if the geometry of the

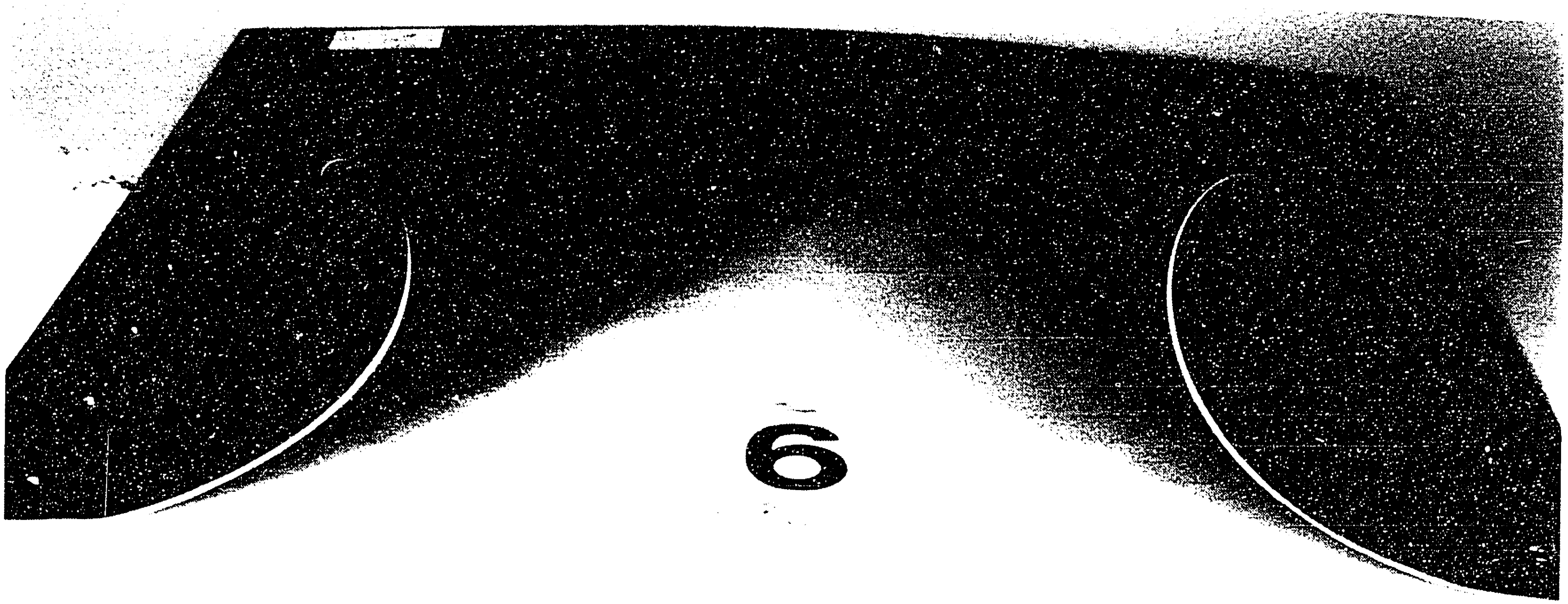

Figure 2.20 Photograph of test specimen #6 taken from behind showing variable radius flaps which form in the wake of the wedge.

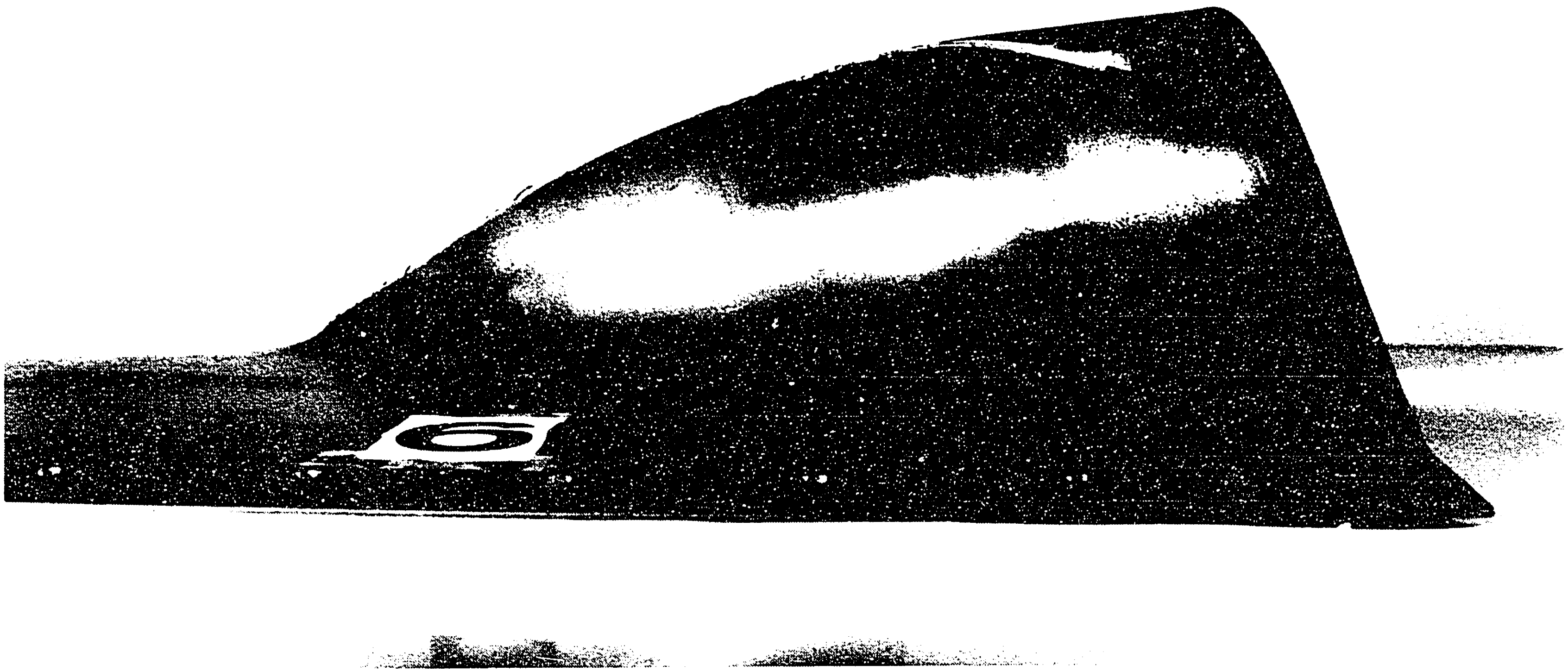

Figure 2.21 Photograph of test specimen #6 taken from the side showing the cut edge of one flap.

wedge and the girder spacing is such that the hinge line reaches the boundaries before the process enters steady state and the flaps become parallel to the axis of the wedge.

The most obvious difference between the observed kinematics and the hypothetical kinematic model of the cutting process was that in all eight tests the crack originated exactly at the tip of the wedge. In the model of Chapter One, a small gap exists between the two. This may not be so much a departure from the theory as it is a special case. When the wedge tip and crack tip coincide, the length of the plastic membrane zone ahead of the wedge can be precisely determined from the geometry of the problem, and the fracture parameter δ_t is not needed. This will be true when the material has sufficient fracture toughness to resist tearing in the near tip zone all the way up to the wedge tip.

The key to determining the applicability of the present model is to determine if the plate is actually torn due to transverse stretching, or cut due to longitudinal shearing by the wedge. The difference between the two is illustrated in Figure 2.22. When the rounded wedge penetrates the plate the tip of the crack is some small distance ahead of the wedge and the crack propagation is cause by the transverse separation of the plate by the wedge. When a very sharp wedge penetrates the plate the tip of the wedge cuts the plate directly ahead of it in a metal removing or machining type of process. It is apparent that in at least one case (Test #8) the crack in the plate was caused by cutting the pre-stressed membrane zone

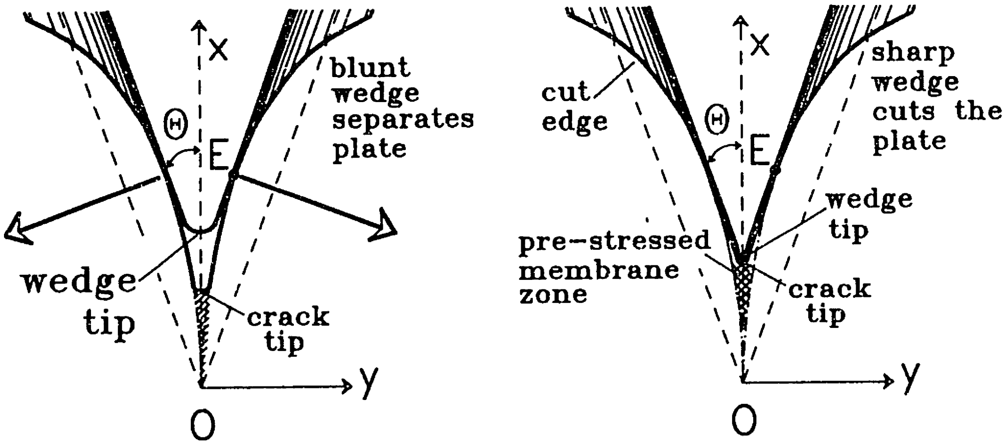

Figure 2.22 Comparison of a blunt wedge to a sharp wedge in plate cutting experiments.

ahead of the wedge tip, rather than by transverse tearing of the near-tip zone. The existence of a machining like process is evidenced by the strip of material removed by the wedge (see Figure 2.11). It is interesting to note that Equation (1.38) still adequately predicted the cutting force in this case, even though the mechanics of the process were significantly different from those for which the theory was developed.

The above discussion points out the need for further plate cutting experiments which are designed to ensure that the near tip zone is torn, not cut. In a ship grounding, it is likely that the reef will not be as sharp as the wedges used here, and as a result the plate will crack due to separation, not due to cutting. This is the mechanism which the present experiments were intended to investigate, but it appears likely that the sharp wedges used here actually resulted in some combined action of transverse tearing and longitudinal cutting in the near tip zone. The same is true of the experiments of Reference [15], since the tip of the wedge always coincided with the tip of the crack is those tests as well [45]. Future experiments should be conducted with blunt or rounded wedges to ensure that the near-tip zone is torn, not cut. Additionally, less ductile material may yield better and more realistic results, even with the sharp wedges. The 3003 aluminum used in these tests was chosen for its availability in thin sheets and its low yield strength, but its high ductility is not desirable since the mild steel normally used in ship construction is not extremely ductile. Likewise, the ASTM A366 steel used here was chosen because it was the only steel readily available in small thicknesses, but it too may be more ductile than is desired.

The possibility that these tests results will not scale with thickness, or do not apply to all materials, should not be overlooked. In the derivation of Chapter One it was assumed that the dimensionless crack tip opening parameter, $\overline{\delta}_t = \delta/t$, is approximately equal to 1. Since this parameter can be thought of as a toughness/thickness ratio, the value of 1.0 is reasonable for the high toughness, low thickness materials tested here. When thicker plates of less tough material (mild steel) are cut, $\overline{\delta}_t$ may be significantly less than 1.0, and other thickness effects may be observed. One of the recommendations in the conclusions of Chapter One was that more experimentation be conducted to determine the relationship between plate thickness and toughness so that a reasonable value of $\overline{\delta}_t$ can be established.

2.5.2 Steady State Plate Cutting

The second major objective of these tests was to determine the critical length at which the plate cutting process transitions to steady state, and to develop a method of predicting the steady state cutting force. Hypothesis #1 of Section 2.2 theorized that the critical length is approximately equal to twice the wedge length, $\ell_{cr} = 2\ell^*$, and that the steady state cutting force is given by Equation (2.3), evaluated with $r = 2$. For the most part, this theory is validated by the test results.

Figures 2.4 thru 2.11 all clearly show that the plate cutting process does leave the initiation phase and transition to steady state; that is, that the cutting force becomes essentially constant at some point after the shoulder of a wedge has penetrated the plate. These plots also show that the transition consistently occurs when the cut length is approximately equal to twice the wedge length. Figure 2.22 is a dimensionless plot of cutting force vs. cut length, which summarizes all of the experimental data presented in the previous section. In this plot, the cut length has been normalized with the wedge length, so that a reasonable value of the experimental coefficient use in Equation (2.3), $r = (\ell_{cr}/\ell^*)$, can be determined. The trend in Figure 2.12 is evident, and suggests that, within the range of parameters tested here, it is reasonable to approximate the critical length by $\ell_{cr} = 2\ell^*$. Substituting $r = 2$ into Equation (2.3), the approximate expression for the steady state cutting force

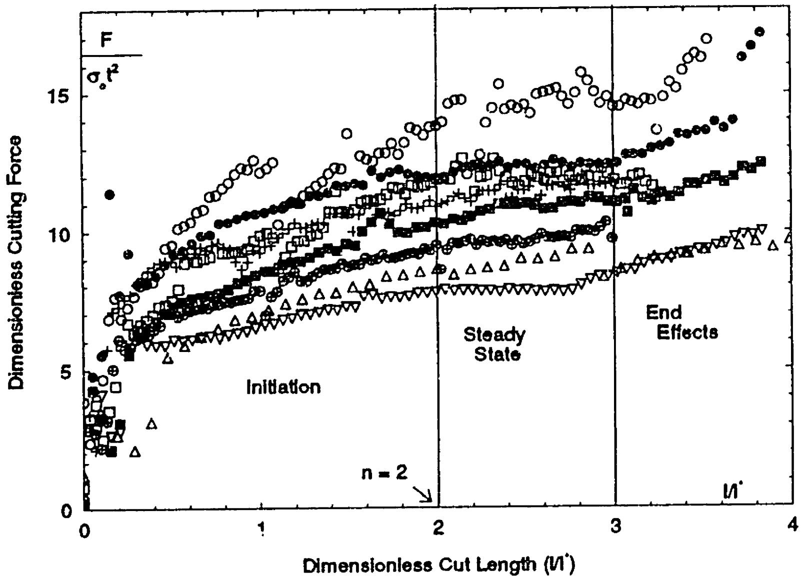

Figure 2.23 **Dimensionless plot of force vs. cut length for tests #1 thru #8.**

becomes;

$$F_c = 4.328\,\sigma_o\,(\overline{\delta}_t)^{0.6}\,\mu^{0.4}\,(\ell^*)^{0.4}\,t^{1.6}\;. \qquad (2.16)$$

Although the transition to steady state appears apparent from the force trace data, it was not so apparent from the observed kinematics. According to the theory of Section 2.2, when the cutting process enters steady state the flaps of the plate in the wake of the wedge will bend parallel to the axis of symmetry, at a width equal to or slightly greater than the maximum wedge width. In this way, the radius of the flaps becomes constant in the wake of the wedge, and the force can become steady. Of the tests presented here, only Test #1 (Figure 2.4) readily displayed this steady state mode. In that test, which involved the 20° wedge cutting the thinner of the two aluminum plates, the flaps began to bend when the wedge was about 200 mm into the plate, and they were almost parallel by the time the wedge reached 300 mm (at which point the test was stopped). One could see the flaps bending parallel as the wedge progressed.

In the other tests the transition was not so obvious, although measurement of the specimens indicate that the flaps began to bend parallel to varying degrees. Three general trends were apparent from these measurements;

1) The thinner the plate the more parallel the flaps became before the test was ended.

2) Plates cut with the 20° wedge displayed the steady state mode more (flaps became more parallel) than those cut with the 30° wedge. This was true despite the fact that the 30° wedge was the shortest, and that the cut length in these specimens was the longest in terms of number of wedge lengths (ℓ_{max}/ℓ^*).

3) The flaps of the aluminum specimens were bent parallel more than those of the steel specimens.

It is apparent from these observations that the transition to steady state is a gradual process, and that the "transition length" depends on both material and geometric parameters. Had the cutting process been allowed to continue undisturbed, every specimen would have eventually displayed the steady state mode with the flaps in the wake of the wedge being parallel. In one test on very thin aluminum plate (not included in Section 2.4) using the 20° wedge, the flaps bent parallel immediately after the shoulder of the wedge passed the $2\ell^*$ point, and remained parallel for the rest of the cut. In this case the transition length was very short, and the cutting process was truly in steady state. In Test #6, which involved the thickest steel plate and the 30° wedge, the flaps had just slightly begun to bend parallel before the test was stopped. Here, the transition length was much longer, and although initiation was clearly ended, steady state could not have been fully reached.

It is interesting to re-evaluate the force trace data (Figures 2.4 - 2.11) in light of the above discussion. Clearly, the cutting process must be thought of in three distinct stages, not two as previously stated. These stages are initiation, transition, and steady state. The experimental data presented here seems to indicate that the *transition* to steady state begins when the cut length is twice the wedge length. The transition length depends on the geometric and material parameters. The force will only become truly steady once this transition is complete. It is interesting to note, however, that the experimental data shows that the cutting force increases only slightly, if at all, during the transition. As a result, the force predicted by Equation (2.16) is still a very good estimate of the steady state force.

Further experimental work will be required to more fully investigate the transition phase of the cutting process, and to quantify the parameters which control the transition length. Larger specimens should be cut, and the experiments should be carried out until the steady state deformation mode is physically displayed. The parametric study must include the full range of plate thicknesses and wedge angles. The results of such a study may very well conclude that the best estimate of the steady state cutting force is given by Equation (2.16) with a slightly modified coefficient to account for the small increase in force during the transition period.

2.5.3 Transverse Tearing in the Wide Wedge Mode.

The transverse tearing of the flaps, which is predicted in Section 2.2 to occur when a plate is cut by a wide wedge, was not observed in any of the experiments. As a result, Hypothesis #2 could not be confirmed. There are two possible explanations for the apparent discrepancy between the theory and the experimental observations.

First, the wedge may not have been wide enough. According to Equation (2.15) the critical wedge semi-angle above which the transverse tearing begins is a function of the critical strain to rupture, ε_{cr}. For a wedge with a 30° semi-angle to cause transverse tearing, the plate material must have $\varepsilon_{cr} < 0.34$. Although no tests were conducted to determine the critical strain to rupture of the specimens used in these experiments, the supplier of the aluminum lists $\varepsilon_{cr} \approx 0.6$, and many tests on similar steel have shown $\varepsilon_{cr} \approx 0.4$ [30]. It is interesting to note, that in the cases of ship grounding when the transverse tears in the flaps of the plate have been observed, often an additional observation made is that the plate material is quite brittle. Clearly, tests should be conducted on specimens which have a lower critical strain to rupture, less ductility, and greater thickness.

A second possible explanation for the fact that transverse tearing of the flaps did not occur is that the characteristic length λ may not be $\lambda = \ell^*$ as assumed in the theoretical analysis, but $\lambda = 2\ell^*$ or $3\ell^*$. This would mean that the tests were not carried out far enough for the tearing to begin. The difference in the assumed wave length does not fundamentally change the theoretical analysis of section 2.2.2, but it would change Equation (2.13) slightly.

The fact that Hypothesis #2 could not be confirmed is considered a significant shortcoming of the present experimental program, and it points out the need for further experimentation. Nevertheless, the theoretical analysis of plate tearing presented in Section 2.2.2 is at least as good as what has been proposed in recent literature [34] [35] [40], and will be considered adequate for application to the ship grounding problem in Chapter 3 until it can be improved upon through experimentation.

2.6 Conclusions

A method of estimating the steady state cutting force when a plate is cut be a wedge has been developed. The approximate steady state force is given by Equation (2.16).

The theoretical force to tear the flaps of the plate in the wake of the wedge transversely is given by Equation (2.13). This transverse tearing will occur only when the wedge semi-angle is greater than the critical wedge angle θ_{cr}, given by Equation (2.15). Although the "wide wedge" mode was not observed in the tests reported here, the theoretical analysis is based on the essential concepts of structural mechanics, and is adequate for practical application to the ship grounding problem.

Further experimental work is required to specifically address the following aspects of plate cutting;

1) Cut the plate with a blunt or rounded wedge so the near-tip zone is torn transversely, not sheared longitudinally.

2) Cut larger specimens so that the process has a chance to truly enter steady state. Conduct a parametric study to determine which factors control the transition length, and how much the force increases during transition.

3) Design an experiment specifically to test Hypothesis #2 give in Section 2.2. This may require the use of less ductile material and/or wider wedges. The experiments should be designed so that the same material is cut in the "narrow wedge" mode and then in the "wide wedge" mode so that Equation 2.13 can be verified.

IV. Chapter 3
Damage Prediction Model for Unidirectionally Stiffened Double Hull (USDH) Vessels.

3.1 Introduction

As stated earlier, much of the motivation behind the experimental and theoretical work on the cutting of plates by a wedge is the development of an effective damage prediction model for vessel groundings. In this chapter, the analysis and results of Chapters One and Two are employed to formulate a method of calculating the work done by the horizontal resisting force of the bottom plate during a steady state, high energy grounding of a Unidirectionally Stiffened Double Hull (USDH) vessel. The work is then set equal to the kinetic energy of the vessel to determine the longitudinal extent of damage in the steady state grounding mode. The steady state problem is an important part of the overall grounding process, and it has not been thoroughly addressed in previously published models.

In their first report on high energy groundings [34], Wierzbicki et al. broke the analysis into four basic steps;

i) Outer dynamics;

ii) Initiation of local damage;

iii) Interaction between the overall ship motion and localized damage; and,

iv) Steady state grounding.

The "outer dynamics" of the grounding problem refers to the rigid-body motion of the vessel over an object without regard for permanent damage to the bottom structure. Analysis of the outer dynamics resolves the horizontal and vertical contacts forces between the ship and the grounding bottom at any time during the event. The contact forces depend on the global parameters of the vessel and the reef, and not on the type of hull construction. A complete analysis of this part of the grounding event is presented in [34], and is valid for the present analysis. Among the parameters determined form the outer dynamics problem is the extent of global lift (Δ_L) of the vessel due to the vertical force of the contacting bottom.

The initiation of local damage refers to initial denting or penetration of the hull after contact with the rock. McKenney [36] addressed initiation for the USDH by considering the static stranding situation in which the penetration depth depends on the global reaction force and the geometry of the impacting rock. His analysis can be used to estimate the penetration depth for the steady state phase.

Peer [37] addressed the interaction between global motion and local deformation by coupling Wierzbicki's steady state grounding model with the friction and lift forces at every point along the vessel's length. Coupling of the global and local effects accounts for the fact that as the ship moves over an obstacle the relative magnitudes of energy dissipated by lift, friction, and steady state structure damage changes.

It is the steady state portion of the grounding event which is the focus of the present formulation. Wierzbicki [34] [35] approximated steady state damage propagation as a series of re-initiations of local damage caused by pressing a rock into the ship hull at a given location. For the USDH hull then, Wierzbicki's approach would consist of successive application of McKenney's model [36]. The force resisting steady state grounding is approximated from the local force-deformation characteristics of the hull girder.

Vaughan [1] formulated an empirical method for analysis of steady state grounding based on Minorsky's [5] work on ship collisions. He divided the grounding energy into surface and volume based components corresponding to the energy due to tearing or fracture and the energy due to plastic bending respectively. Vaughan [6] and Jones and Jouri [10] empirically determined proportionality constants for each energy term from an analysis of the plate cutting experiments of Akita and Kitamura [4]. Vaughan,s empirical analysis was used by Det norske Veritas (DnV) as part of their comparative study of various Very Large Crude Carrier (VLCC) designs [41], and by David Taylor Research Center (DTRC) for their Collision and Grounding Assessment for Double Hull Tankers prepared for the U. S. Coast Guard.

An improved method of estimating the steady state resisting force of the bottom and inner bottom plate has been developed using the equations presented in Chapter Two. These equations have, in turn, been incorporated into Wierzbicki's damage prediction model [35] to produce a model which is greatly enhanced over the empirical method of Vaughan [40]. Application of the wedge indentation analysis is particularly appropriate for the problem of grounding on narrow rigid reefs where plate tearing and bending is the primary mode of energy absorption. The narrow reef scenario is the one for which most of the existing steady state damage prediction models have been developed [1] [2] [34] [35] [41]. Of course, as a practical matter, major longitudinal and transverse members will also be damaged, and will absorb a significant amount of energy in the process. The work done in deforming the longitudinal girders is not neglected in the present formulation, but is included in an approximate way.

The Unidirectionally Stiffened Double Hull (USDH) construction type has been chosen for the present model for two reasons. First, because of the simple construction (see Figure 3.2 for a typical USDH section) there are no longitudinal stiffeners or transverse members, and as a result it is reasonable to expect that plate tearing and bending is the primary mode of energy dissipation. Furthermore, for the narrow reef, the side girders will provide nearly rigid support for the plate panels, making the analysis of Chapters One and Two particularly applicable. When the breadth of damage does include two or more girders the additional work to remove those members can be adequately estimated.

Additionally, as outlined in [37] and [39], USDH construction has several distinct advantages over traditional double hull construction which may make it the preferred double hull in the future. Design, fabrication, maintenance, repair, inspection, and cargo capacity are all enhanced with the USDH over traditional construction. It should be noted here that the present model can easily be adapted to describe steady state grounding of conventional double hull or single hull vessels as well. The longitudinal stiffeners which are used in these other construction types can simply be "smeared" in to the bottom and inner bottom plates through the use of equivalent thickness. The resulting thicker plate is then analyzed using the exact same equations to be developed in this chapter. The concept of equivalent thickness has been used often in the past [34] [35] [40] [41] [42], and is generally considered an adequate means of accounting for the stiffeners. In Section 3.7, the present damage prediction model is applied to a single hull, mid-deck vessel for the purpose of performance comparison.

3.2 Formulation of the Problem

Consider an USDH tank vessel of mass M running onto a narrow rigid reef at velocity V_o, as shown in Figure 3.1a. The reef is originally a height Δ_r above the baseline of the vessel and first contacts the ship bottom near the bow. The reef geometry is as shown in Figure 3.1b, where α is the sloping angle, β is the spreading angle and θ is the wedge angle at the front of the rock. The distance ℓ^* is the wedge length of the idealized reef, and has the same meaning as the ℓ^* defined in Chapter 2.

When the bow of the vessel hits the reef, the reaction force has both vertical and horizontal components. As a result of the horizontal force, the ship will actually be lifted the distance Δ_L. The amount of lift may be quite substantial near the bow of the vessel, and the damage to the bottom structure is limited to crushing without penetration.

As the vessel travels over the reef, however, the local reaction force between the ship and the reef will increase to the point that one or both of the hulls is penetrated. When the bottom plate ruptures, the penetration depth Δ differs from the reef height Δ_r by the amount of lift Δ_L, so the $\Delta_r = \Delta + \Delta_L$. The transition between "ride over" with no penetration which occurs near the bow, and steady state damage with full penetration which occurs later, is the initiation and development of localized damage stage of the grounding event. It is a complex problem because it involves changing

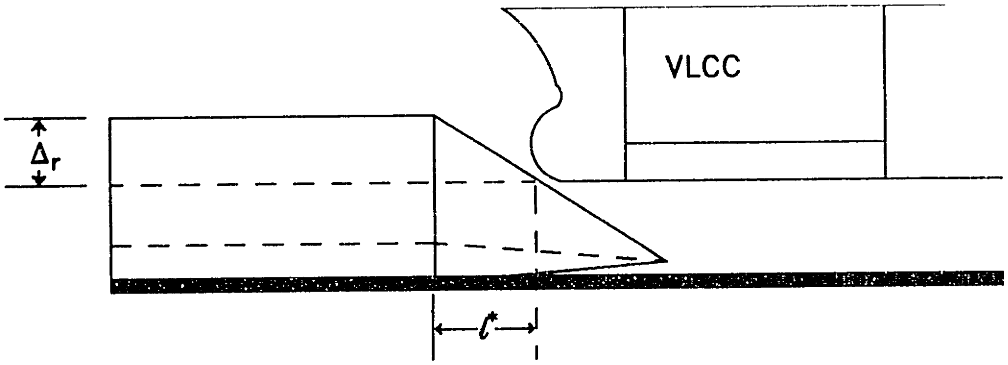

Figure 3.1a

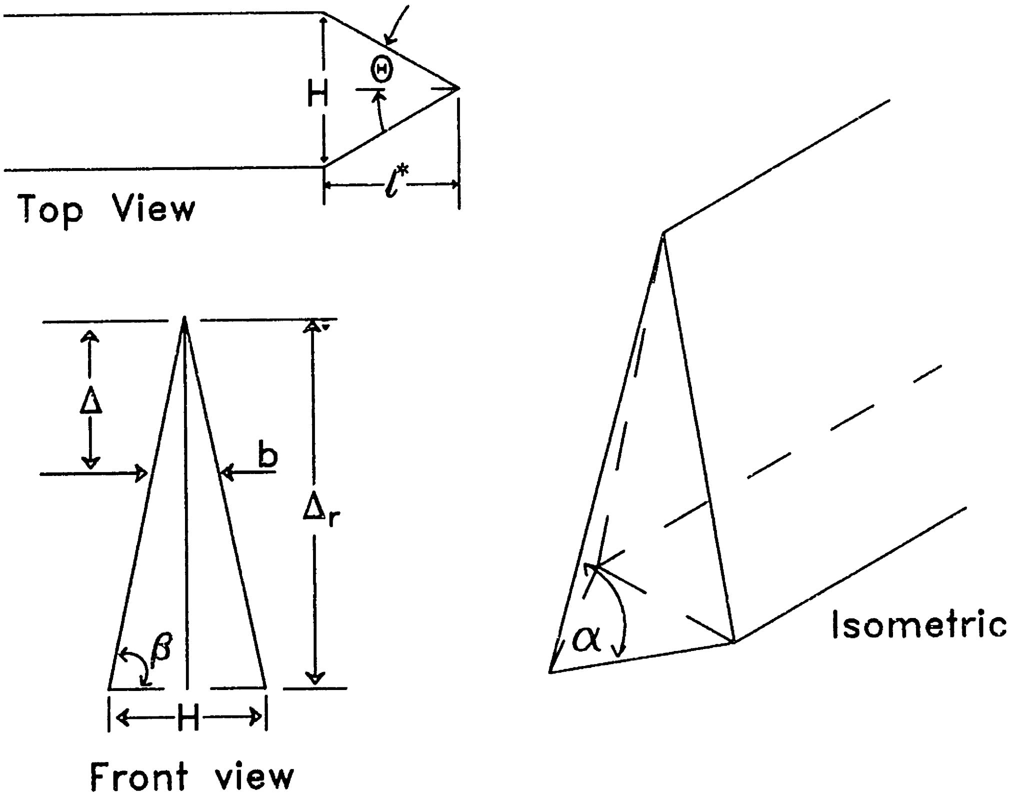

**Figure 3.1. a) Typical grounding scenario for a VLCC.
b) Reef geometry**

geometries and varying ratios of horizontal, vertical, and frictional forces. As such it requires separate analysis and is not specifically addressed here. It should be noted that very little analysis of this part of the grounding problem can be found in the literature, perhaps because for large vessels the transition stage is thought to be a relatively small part of the overall event.

Once the bottom plate has been penetrated and the maximum vertical extension of the rock into the hull has been reached, steady state grounding can be assumed. As the vessel continues to move over the reef, the breadth of damage in the bottom and inner bottom plates, and the number of girders removed, depends on the geometry of the rock and the dimensions of the hull.

For the present analysis, the penetration depth Δ (and thus the breadth of damage) is considered constant throughout the steady state stage, and is not coupled to the global motion of the vessel. Constant penetration depth during steady state grounding is not a bad approximation, especially locally where it has been shown that the relative magnitudes of lift and friction along the length of one cargo tank change gradually [35] [37]. The steady state model developed here could be easily coupled to global motion in an approximate way by calculating Δ at discreet points along the length of the vessel (at the center of each tank for example) using Peer's analysis [37] and then varying the penetration depth linearly between those points.

The following additional assumptions are made in the present analysis;

i) The reef penetrates the hull at or near the centerline of the vessel and travels directly aft so that non-symmetric loading or moments are not considered.

ii) The rock material is rigid and does not crush during the grounding process so that the rock height and wedge angle θ remain constant throughout.

iii) The bottom of the vessel is locally flat.

iv) The reef is sufficiently "sharp" to cause penetration of the hull; the "rideover" mode is not considered.

3.3 Steady State Deformation of the Plate

In Chapter Two, expressions were derived for the steady state resisting force of the plate for two deformation modes: penetration by a narrow wedge, and penetration by a wide wedge. Here those equations are used to estimate the steady state resisting force of the bottom and inner bottom plates in grounding by determining the wedge lengths in both plates as a function of local penetration depth Δ, and the specific geometry of the rock and hull. Once the local wedge lengths have bee determined, the horizontal resisting force of the plates can be expressed as a function of the penetration depth and a simple parameter Λ, which characterizes the reef.

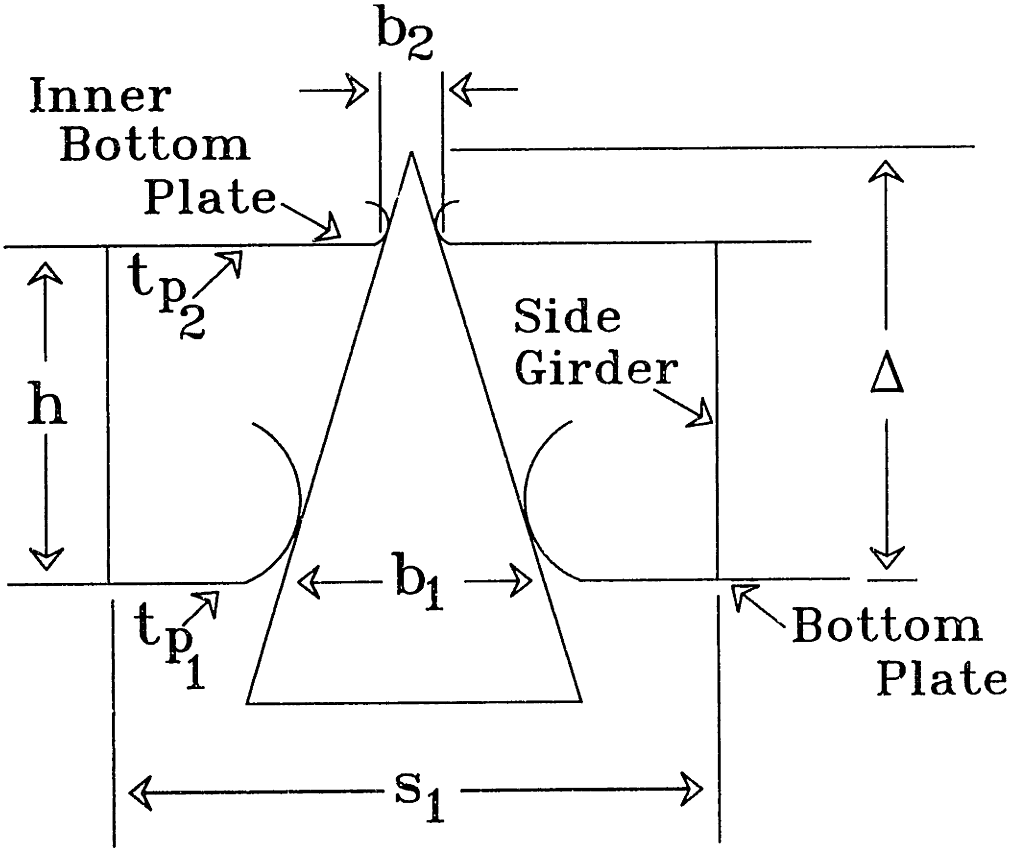

Figure 3.2 Damage to USDH extending to plate only.

3.3.1 Local Breadth of Damage

Figure 3.1 defines the geometry of the reef to be used in this analysis. Notice that Δ_r is the height of the rock above the baseline of the vessel before the grounding, and that H is the maximum breadth of the rock at a depth equal to the draft of the vessel before the grounding. These parameters are used to characterize the rock because they are what would most likely be available from bottom surveys of specific waterways.

Figure 3.2 shows the local geometry of the USDH section once it has been penetrated by a rock and local damage of the plates has reached steady state. Notice that the distance Δ is the local penetration depth of the rock into the hull. It differs from Δ_r by the distance Δ_L, which is the local lift of the vessel. As mentioned above, the lift is not calculated here. It is assumed that Δ has been determined by the method outlined in [34] or [37] at the specific location for which steady state analysis is desired.

The local breadth of the reef at any distance d from the top can be related to the maximum breadth H by

$$b = \left(\frac{d}{\Delta_r}\right) H. \tag{3.1}$$

The breadth of damage in the bottom plate is then

$$b_1 = \left(\frac{\Delta}{\Delta_r}\right) H \quad (\Delta > 0). \tag{3.2}$$

The breadth of damage in the inner bottom plate is

$$b_2 = \left\{ \begin{array}{cc} 0 & (\Delta < h) \\ \left(\frac{\Delta - h}{\Delta_r}\right) H & (\Delta > h) \end{array} \right\} \tag{3.3}$$

where h is the double bottom spacing.

3.3.2 Wedge Length

Consider again the reef geometry shown in Figure 3.1. The wedge angle θ is constant throughout the entire height Δ_r of the rock, but the wedge length ℓ^* decreases with height because of the sloping angle α. Although the value of ℓ^* at any distance from the top of the rock can be expressed directly as a function of α, it is more convenient in this formulation to express it as a function of the wedge angle θ, and local reef breadth b instead. In terms of these parameters, the wedge length at any distance d from the top of the rock is

$$\ell^* = \frac{1}{2}\left[\frac{b}{\tan\theta}\right] . \tag{3.4}$$

Substituting (3.2) and (3.3) into (3.4), the expressions for the wedge length in the bottom plate is

$$\ell_1^* = \frac{1}{2}\left(\frac{\Delta}{\Delta_r}\right)\left(\frac{H}{\tan\theta}\right) \quad (\Delta > 0) \tag{3.5}$$

and in the inner bottom plate,

$$\ell_2^* = \frac{1}{2}\left(\frac{\Delta - h}{\Delta_r}\right)\left(\frac{H}{\tan\theta}\right) \quad (\Delta > h) . \tag{3.6}$$

3.3.3 Plate Cutting Force

The steady state force to cut a plate and bend it into cylindrical flaps in the wake of the reef is given by Equation (2.16). When $\theta < \theta_{cr}$ the flaps will not tear transversely, and Equation (2.16) fully describes the resisting force of the plate. The coefficient $r = 2$ has been incorporated into Equation (2.16) because experiments indicated that the cutting process enters steady state when the cut length is twice the wedge length. Here, however, r will be left a variable to enhance the generality of the model allow for the possibility that future experiments and theoretical analysis will show that r is not constant for all materials and wedges, as discussed in the conclusions of Chapter 2. The steady state force is then given by Equation (2.3);

$$F_p = 3.28\,\sigma_o\,(\overline{\delta}_t)^{0.6}\,\mu^{0.4}\,t^{1.6}\,(r\ell^*)^{0.4}\,. \tag{3.7}$$

which is simply Equation (1.46) evaluated at $\ell = (r\ell^*)$.

Equation (1.46) has been optimized for the range of wedge semi-angles $5° \le \theta \le 25°$ through the minimization of the function $g(\theta)$ described in section 1.7. The elimination of the dependence of the force on the wedge angle θ was an appropriate and effective simplification in the development of the closed form solution, especially in the light of the limited range of wedge angles used in experiments [2] [15]. Here, however, it is better to express $g(\theta)$ explicitly in the formulation so that the model will be better able to accommodate a larger range of wedge semi-angles ($5° \le \theta \le 40°$).

Figure 1.6 shows that the cutting force can increase by a factor of 1.3 when θ is increased from 20° to 40°. Additionally, the present model already has a dependence on θ in the calculation of wedge length (Equation (3.4)) so that no significant simplification is achieved by the elimination of g(θ).

Equation (1.42) is the cutting force with g(θ) expressed explicitly. When evaluated at $\ell = (r\ell^*)$, this equation gives the steady state force

$$F_p = 1.67\,\sigma_o\,(\bar{\delta}_t)^{0.6}\;t^{1.6}\;(r\ell^*)^{0.4}\;g(\theta)\;, \tag{3.8}$$

where g(θ) is given by Equation (1.41) and re-stated for convenience here:

$$g(\theta) = \frac{1}{(\cos\theta)^{1.2}}\left[(\sin\theta)^{0.4} + \frac{\mu}{(\sin\theta)^{0.6}}\right]. \tag{3.9}$$

Substituting the expression for ℓ_1^* (3.5) into (3.9), the steady state force in the bottom plate is

$$F_{p1} = 1.265\,\sigma_o\,(\bar{\delta}_t)^{0.6}\,r^{0.4}\,t^{1.6}\left[H\left(\frac{\Delta}{\Delta_r}\right)\right]^{0.4} g(\theta) \tag{3.10}$$

Similarly, the steady state force in the inner bottom plate is

$$F_{p2} = 1.265\,\sigma_o\,(\bar{\delta}_t)^{0.6}\,r^{0.4}\,t^{1.6}\left[H\left(\frac{\Delta - h}{\Delta_r}\right)\right]^{0.4} g(\theta)\;. \tag{3.11}$$

Because the wedge length ℓ^* is expressed in terms of the wedge angle θ, the dependence of the force on θ is changed slightly from (3.9) so that now;

$$g'(\theta) = \frac{1}{(\cos\theta)^{1.6}}\left[(\sin\theta)^{0.8} + \frac{\mu}{(\sin\theta)^{0.2}}\right]. \qquad (3.12)$$

Further simplification can be accomplished by defining a non-dimensional constant Λ which describes the aspect ratio of the reef;

$$\Lambda \equiv \frac{H}{\Delta_r}. \qquad (3.13)$$

Now, the resisting force in the bottom plate for penetration by a narrow wedge is

$$F_{p1} = 1.265\,\Lambda^{0.4}\,\sigma_o\,(\bar{\delta}_t)^{0.6}\,r^{0.4}\,(t_{p1})^{1.6}\,(\Delta)^{0.4}\,g'(\theta) \qquad (0 \le \Delta), \quad (3.14)$$

Analogously, the narrow wedge force in the inner bottom plate is

$$F_{p2} = 1.265\,\Lambda^{0.4}\,\sigma_o\,(\bar{\delta}_t)^{0.6}\,r^{0.4}\,(t_{p2})^{1.6}\,(\Delta - h)^{0.4}\,g'(\theta), \quad (h \le \Delta) \quad (3.15)$$

3.3.4 Plate Tearing Force

When the reef wedge angle θ is greater than θ_{cr} the reef is considered wide, and the plate flaps in the wake of the reef will tear transversely at a characteristic interval λ. This tearing force F_T, described by Equation (2.13), must be added to the force given by (3.14) and (3.15). Substituting

Equations (3.2) and (3.3) for the breadth of damage in the bottom and inner bottom plates into equation (2.13), and employing the reef aspect ratio Λ, the additional force to tear these flaps is;

$$F_{T_1} = t_{p_1} \sigma_o \epsilon_{cr} \Delta \Lambda \left[1 - \frac{\epsilon_{cr} \cos\theta}{(\tan\theta)^2} \right] , \qquad (\theta > \theta_{cr}) . \qquad (3.16)$$

$$F_{T_2} = t_{p_2} \sigma_o \epsilon_{cr} (\Delta - h) \Lambda \left[1 - \frac{\epsilon_{cr} \cos\theta}{(\tan\theta)^2} \right] , \qquad (3.17)$$

$$(\theta > \theta_{cr} \ \wedge \ \Delta > h) .$$

Of course the total resisting force of the plate in the steady state mode is the sum of (3.14), (3.16), (3.17) and (3.18) as they apply given the geometries of the reef and the hull.

3.4 Steady State Deformation of the Longitudinal Girders

In most groundings, the steady state damage will extend beyond just the bottom plate to include one or more sets of girders. The geometry of this situation is shown in Figure (3.3). It is assumed that the girders begin to deform as soon as the breadth of the rock in the bottom plate b_1 equals the girder spacing s_1. The girder will be forced outward and bent about a hinge a distance τ up from the bottom plate, where $0< \tau \leq h$ is the height at which the local rock width b is precisely equal to s_1. The transverse deformation causes strain along the length of the girder to the point that critical strain ε_{cr} is reached and the girder will tear and form a "flap". As the vessel continues over the reef the pattern of "torn flaps" will continue at some characteristic wave length in a manner very similar as that for the transverse tearing of the bottom plate by a wide wedge discussed in Chapter 2. This deformation mode is shown schematically in Figure 3.3, and with more detail in Appendix E, Figure (E1).

The steady state resisting force of one longitudinal girder in this deformation mode is calculated in Appendix E, and is given by;

$$F_g = t_g \sigma_o \epsilon_{cr} \tau \, , \qquad (3.18)$$

where τ is the height to which the girder is torn.

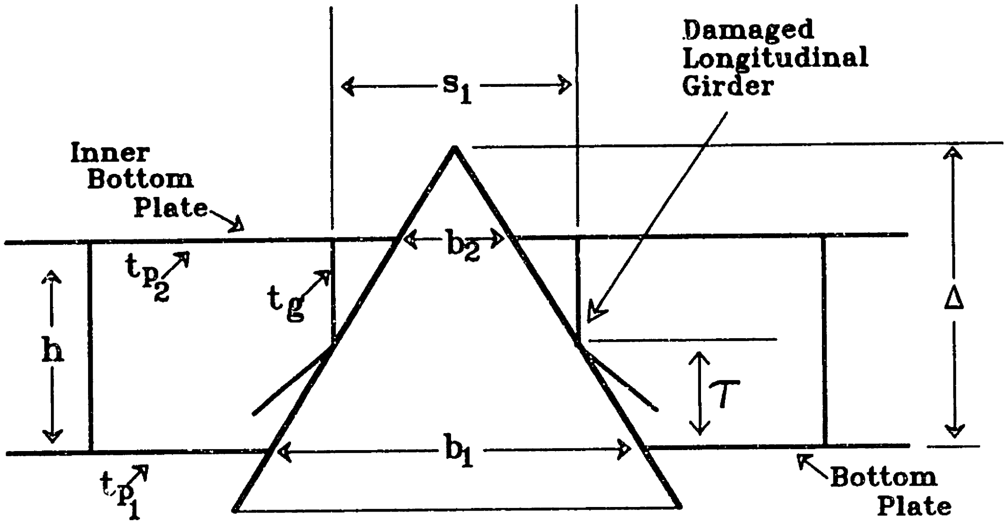

Figure 3.3 Damage to USDH extending to the longitudinal girders.

Because the damage is assumed to be symmetric about the centerline of the vessel, the girders are damaged in sets and Equation (3.18) must be multiplied by 2 to find the steady state force for a set of girders. The geometry of the reef and hull enter the solution by solving for the number of damaged girder sets k, and the distance τ for each girder set.

The number of damaged girder sets damaged is found from the geometry of the rock and the hull;

$$k = \left\{ \begin{array}{ll} 0 & (b_1 < s_1) \\ \frac{1}{2}\left[\frac{\Delta\,\Lambda}{s_1} + 1\right] & (b_1 \geq s_1) \end{array} \right\}, \tag{3.19}$$

where k is rounded down to the nearest integer.

The distance τ is different for each damaged girder set and it decreases with the transverse distance from the point of penetration. For example, at the first set of damage girders,

$$\tau_1 = \Delta - \frac{s_1}{\Lambda},$$

and at the second set,

$$\tau_2 = \Delta - \frac{3\, s_1}{\Lambda}.$$

In general, at the mth set of damaged girders,

$$\tau_m = \Delta - \frac{(2m-1)\, s_1}{\Lambda} \qquad (m=1,2,3\ldots) \tag{3.20}$$

Of course, τ can not be greater than the hull spacing at any of the damaged girder sets so that Equation (3.20) is subject to restriction;

$$\tau_m = \left\{ \begin{array}{ll} \Delta - \dfrac{(2m-1)\, s_1}{\Lambda}, & \left(\Delta < h + \dfrac{(2m-1)\, s_1}{\Lambda}\right) \\ h, & \left(\Delta \geq h + \dfrac{(2m-1)\, s_1}{\Lambda}\right) \end{array} \right\}. \tag{3.21}$$

Combining (3.18), (3.19), and (3.21) the total force to deform the longitudinal girders is given by;

$$F_g = \sum_{m=1}^{k} 2\, t_g \sigma_o \epsilon_{cr} \tau_m . \tag{3.22}$$

3.5 Total Resisting Force and Longitudinal Extent of Damage

In general, the total resisting force F for the USDH is found by summing the contributions of cutting of the inner and outter bottom plates, tearing of the inner and outter bottom plate, and tearing of the longitudinal girders,

$$F = F_{P_1} + F_{P_2} + F_{T_1} + F_{T_2} + F_g \ . \tag{3.23}$$

where the conditions on Δ, Λ, and θ are as previously stated, This force is constant for a given steady state scenario, but the magnitude of the constant force depends on the geometry of the hull and the reef, determined by the parameters, Λ and θ. For a given hull and reef, the magnitude of the steady state force depends primarily on the penetration depth Δ. As a result, the total force of resistance is quite cumbersome to list explicitly for the general case, but it lends itself readily to computerization. Specific cases will be evaluated latter.

The longitudinal extent of damage is found by equating the kinetic energy of the vessel when it entered steady state grounding to the work done by the plate and girders. Since the resisting force F is assumed constant, the longitudinal extent of damage S_{max} is readily evaluated;

$$S_{\max} = \frac{M V^2}{2 F} \ , \tag{3.24}$$

where M and V are the mass and velocity of the vessel and F is the total force from Equation (3.23), in consistent units.

3.6 Results

Results of the model are presented here in dimensionless plots for a typical USDH tank vessel. The exact equations used to generate these plots are presented in Appendix G. For all the plots the free parameters in the model were chosen to be consistent with Chapters One and Two as follows;

$\overline{\delta}_t = 1.0,$

$\mu = 0.3,$

$r = 2,$

$\varepsilon_{cr} = 0.2.$

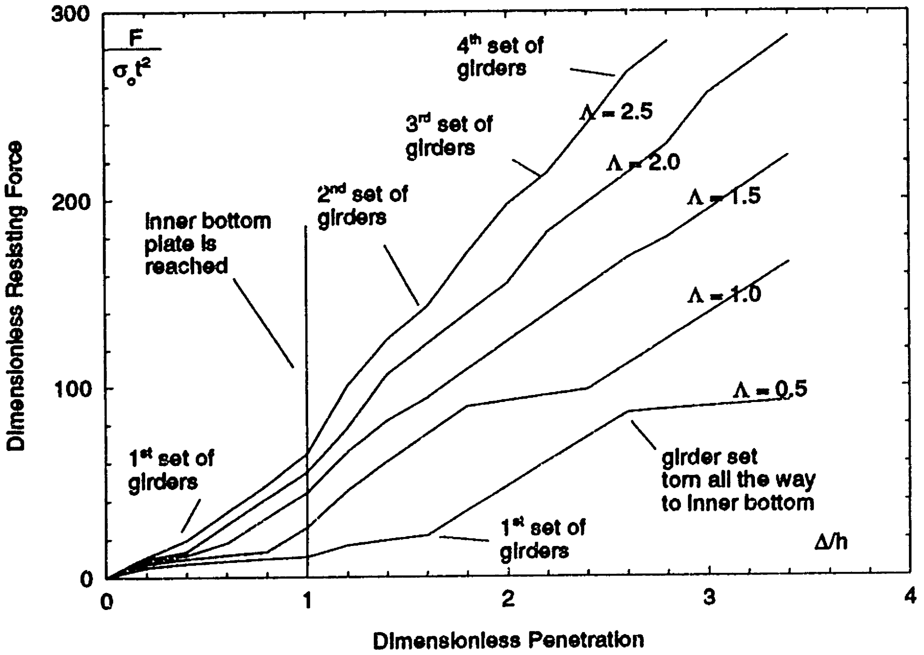

Figure 3.4 Dimensionless horizontal resisting force vs. dimensionless penetration depth for a typical USDH vessel at various reef aspect ratios, Λ.

Figure 3.4 is a plot of the dimensionless horizontal resisting force versus dimensionless penetration depth (Δ/h) for five values of the reef aspect ratio Λ. All of these curves show step increases in the force when the dimensionless penetration depth is equal to 1. This reflects the additional contribution of the inner bottom plate which begins when the penetration depth Δ is equal to the double bottom spacing h. The other step increases on these curves occur each time the rock reaches a set of longitudinal girders and additional resistance is added. The plot shows that it is the aspect ratio of the reef compared with that of the hull (Λ vs. s_1/h) which determines whether the reef will reach the inner bottom plate or the girder first when the penetration depth is increased. Specifically, when;

i) $\Lambda < s_1/h$ the inner bottom will contribute to the resisting force before the girders are reached;

ii) $\Lambda > s_1/h$ at least one set of girders will be damaged before the inner bottom plate is, and;

iii) $\Lambda = s_1/h$ the first set of girders will be reached at the same penetration depth as the inner bottom plate.

For the calculation carried out in Appendix F, the ratio $(s_1/h) = 0.8$. The $\Lambda = 0.5$ curve on Figure 3.4 shows a small increase at $\Delta/h = 1$ due to the penetration of the inner bottom plate, and then the first girder set is reached when dimensionless penetration has increased to about 1.6.

By contrast, the plot for $\Lambda = 2.5$ shows that the first girder set is damaged when the dimensionless penetration is only about 0.4, well before the inner bottom plate is damaged.

It is interesting to note that $\Lambda = 2.5$ is the reef aspect ratio for which the IMO has evaluated alternative tank vessel designs [41] [42]. A reef of this shape results in minimum longitudinal extent of damage in the inner bottom since two set of girders are damaged before the inner bottom is reached, and the resisting force of the USDH structure is highest.

The curve corresponding to $\Lambda = 0.5$ on Figure 3.4 best shows the effect of tearing a girder set on the total resisting force. For a reef of this aspect ratio only one girder set is damaged over the dimensionless penetration range plotted. Notice the steep increase in slope of the force curve when the reef just reaches the girder. This slope remains relatively constant until the penetration has increased to the point that the girder is torn through its entire height, h. The force curve then levels out at a higher value.

Figure 3.5 is a dimensionless plot of resisting force vs. penetration depth for three different wedge angles at $\Lambda = 2.0$. Holding Λ constant means that the breadth of damage is

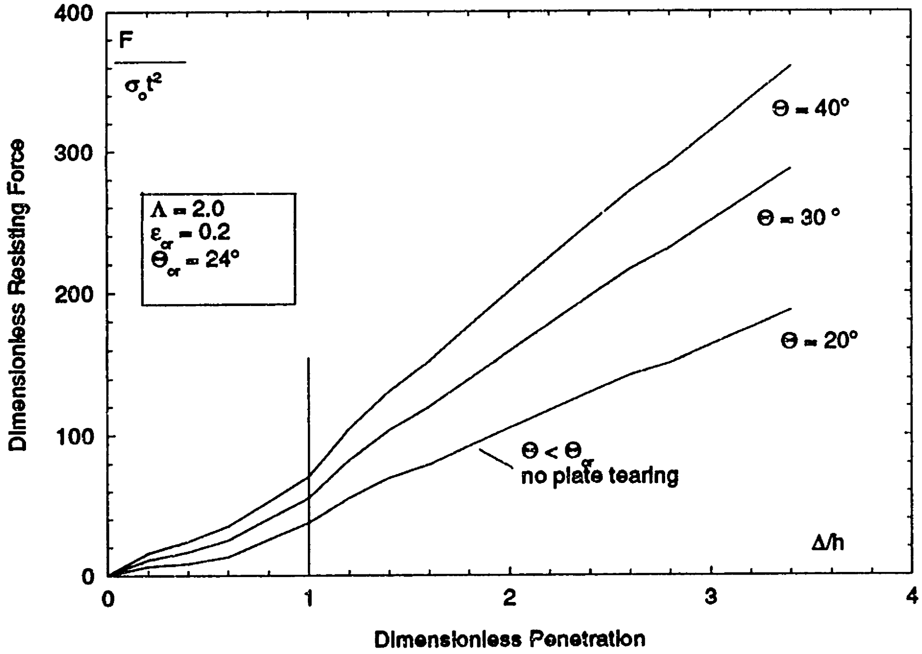

Figure 3.5 **Dimensionless horizontal resisting force of a typical USDH vessel vs dimensionless penetration depth at three different reef wedge angles, θ.**

constant for a given penetration depth in all three cases, but the wedge length ℓ^* increases with θ. As expected, the total force increases with the reef wedge angle not because more girder sets are damaged (the number of girders set is constant for all curves in Figure 3.5), but because both the cutting force and the tearing force of the plate are increased. In Figure 3.5, the value of critical strain to rupture ε_{cr} is 0.2, so that $\theta_{cr} \approx 24°$. This means that the force to tear the plate transversely is not included in the $\theta = 20°$ curve while it is in the other two, which accounts for the large jump in force between $\theta = 20°$ and $\theta = 30°$ curves. A complete discussion of the relative contributions of the three forces is below.

3.7 Discussion

3.7.1 General

The primary refinement which the model developed in this chapter offers over Wierzbicki's previous models [34] [35] is the application of the steady state plate cutting solution to damage prediction. It also revises the plate tearing model [34] [35] to reflect the fact that the plate does not tear transversely in every case, and to include the use of the material parameter ε_{cr} in determining the extent of those tears when they do occur. Like the past models [34] [35], the present model offers substantial additional advantages over Vaughan's method [40] because it specifically addresses the energy absorbing contributions of each structural member, rather than lumping them together empirically. As a result, this model is more general, and applicable over a wider range of reef and hull geometries. The objective of the analysis in this section is to determine how much improvement the present model offers over Vaughan's method in practical application, and to define the range of parameters for which it is most applicable.

3.7.2 Comparison to Vaughan's Method

In two recent comparatives studies conducted by DnV [41] and by DTRC [42], damage assessment for tank vessels was conducted using similar methods, both based on the method of Vaughan [40]. In this section the model used in those studies is compared to the model developed here, via a damage assessment of the 39000 DWT USDH tank vessel detailed in Appendix G.

Vaughan's energy equation from Reference [40] is

$$W_s = 352\, V_s + 126\, A_s, \qquad (ton\text{-}knots^2)\ , \qquad \textbf{(3.25)}$$

where W_s is the work of the ship, V_s is the volume of displaced material, A_s is the area of torn material, and the coefficients 352 and 126 include all of the other parameters of the problem such as wedge angle, friction coefficient, and material constants. In both [41] and [42] Equation (3.25) is expanded for application to double hull vessels;

$$W_s = L_d\,[352\,(b_1\, t_{pe_1} + b_2\, t_{pe_2}) + 126\,(t_{pa_1} + t_{pa_2})] \qquad \textbf{(3.25)}$$

where L_d = longitudinal length of damage (m)
b_1 = breadth of damage in bottom plate (m)
b_2 = breadth of damage in inner bottom plate (m)
t_{pe1} = equivalent thickness of bottom plate (mm)
t_{pe2} = equivalent thickness of inner bottom plate (mm)
t_{pa1} = actual thickness of bottom plate (mm)
t_{pa2} = actual thickness of inner bottom plate (mm)

Equation (3.25) uses equivalent plate thickness in order to account for the longitudinal stiffeners which are damaged by the reef. This method has been widely used in the past, and is generally accepted as valid [34] [35] [40] [41] [42]. For the problem under consideration here, however, the equivalent thickness concept does not apply since the USDH vessel does not have any longitudinal stiffeners. One could argue that the longitudinal girders of the USDH vessel should be incorporated into (3.25) through use of equivalent thickness. That is not done here, however, because it is unclear how the longitudinal girders have been accounted for in the practical application of Vaughan's method in the past. There is no specific mention of the longitudinal girders, and no indication of their inclusion into (3.25), in either the comparative study conducted by DnV [41] or the damage analysis for double hull tankers conducted by DTRC [42], both of which use Vaughan's method.

The coefficients of Equation (3.25) include important material parameters, but the specific value of those parameters for which the empirical coefficients were derived is not known. These parameters are expressed explicitly in the present model, and the values used for this comparison are listed below;

$\sigma_o = 300$ MPa

$\varepsilon_{cr} = 0.2$

$\mu = 0.3$

$\overline{\delta}_t = 1.$

Figure 3.6 compares the total resisting force predicted by Equation (3.25) (Vaughan) to that predicted by the present model as a function of penetration depth Δ and wedge angle θ, for a constant value of reef aspect ratio Λ. Holding Λ constant ensures that the breadth of damage at a given penetration depth is the same for all four curves plotted. Notice that at large reef wedge semi-angles there is good correlation between the present model and Equation (3.25), but at the smaller wedge angles there is considerable difference between the two. Vaughan's method is insensitive to wedge

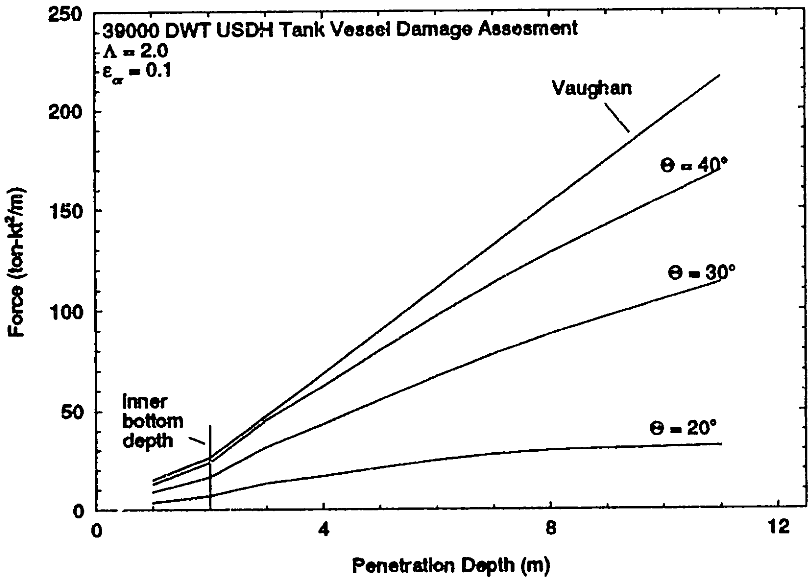

Figure 3.6 **Comparison to Vaughan's Method; resisting force vs. penetration depth for various reef wedge semi-angles, θ.**

angle, while the present model has dependence on θ in both the plate tearing and plate cutting forces explained in Section 3.3. Figure 3.6 shows that the effect of reef wedge angle is significant, and suggests that the present model may offer substantial improvement over the existing models for cases when the wedge semi-angle is less than about 30°.

Figure 3.7 compares the longitudinal extent of damage predicted by Vaughan's method with that of the present model at various penetration depths. The force curve corresponding to θ = 40° was used for this plot. At this wedge angle there is good correlation between the two models. Figure 3.8 shows that when smaller wedge semi-angles are considered the difference between the two models is more pronounced and Vaughan's method substantially under-predicts the damage.

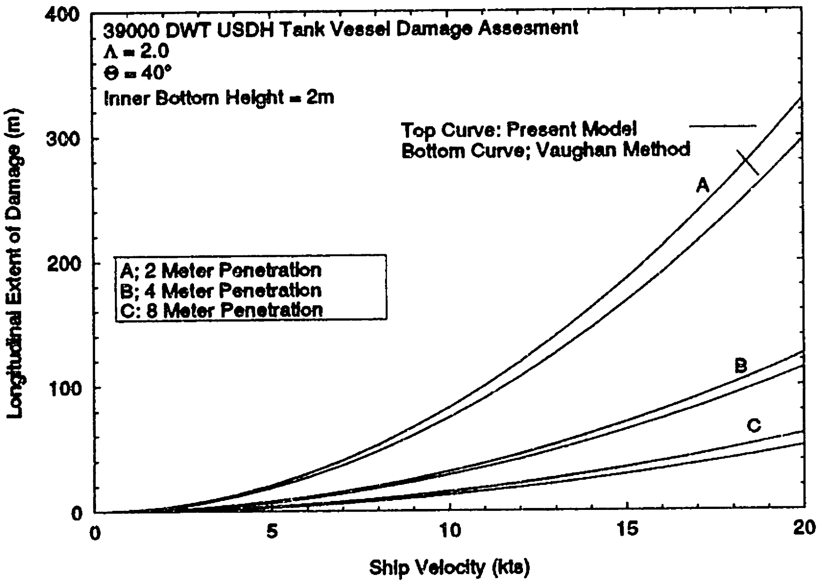

Figure 3.7 Comparison to Vaughan's Method; Length of damage vs. ship speed at θ = 40°, for various reef aspect ratios Λ.

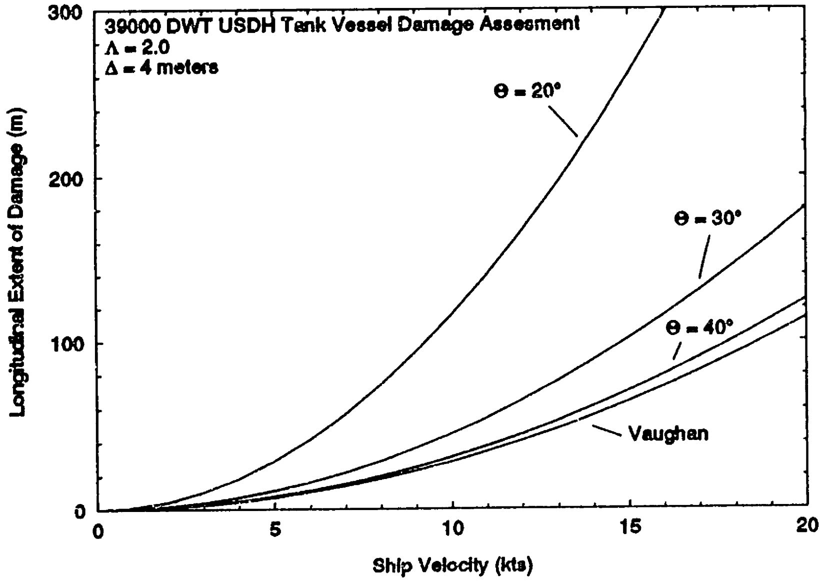

Figure 3.8 Comparison to Vaughan's Method; Length of damage vs. ship speed for various reef wedge semi-angles, θ.

3.7.3 Model Limitations and Range of Application

One distinct advantage that the present model has over past models is that it accounts for each energy absorbing mechanism separately, rather than lumping them together into a single term. The three primary mechanisms in the model are plate cutting, plate tearing, and girder tearing. It is instructive to examine to relative contribution of each of these mechanisms to the total energy absorption over a range of reef parameters. By doing so one can determine how much and under what conditions this new model improves upon the past models. For example, since the girder tearing model used here is not dependent on the wedge semi-angle θ, the fact that Vaughan's method is insensitive to θ is not important when girder tearing dominates the total energy absorption. When girder tearing dominates, therefore, the present model may not offer a great deal of improvement over Vaughan's method. By contrast, when plate cutting and tearing dominate the steady state energy absorption the dependence on θ becomes very important, and the advantage of the present model over Vaughan's method is significant.

Figures 3.9 through 3.11 show how the steady state force is partitioned between the three primary mechanisms as a function of penetration depth, for various values of Λ and constant wedge angle $\theta = 25°$. Several trends are apparent. In all three plots the girder tearing dominates at higher values of dimensionless penetration. For values of Δ/h less than about 1.5 the contributions of the three mechanisms are

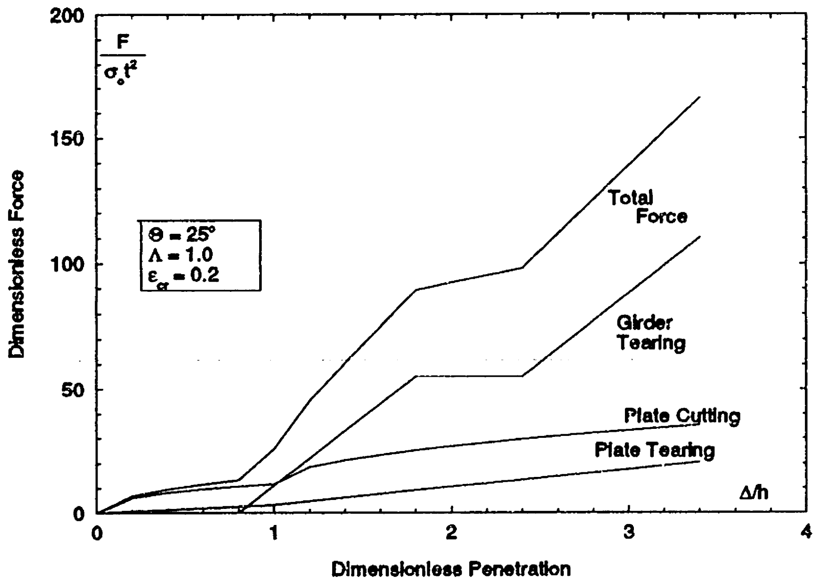

Figure 3.9 Contribution of the three primary mechanisms at $\Lambda = 1.0$

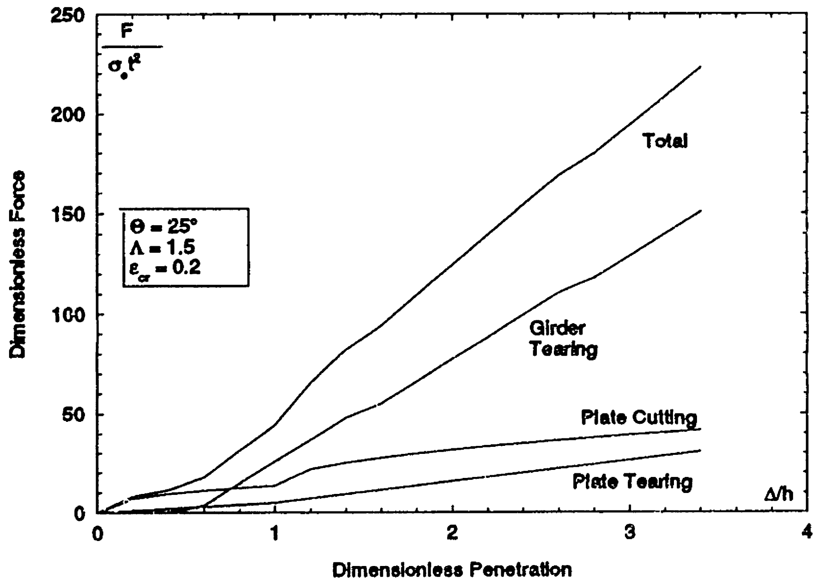

Figure 3.10 Contribution of the three primary mechanisms at $\Lambda = 1.5$

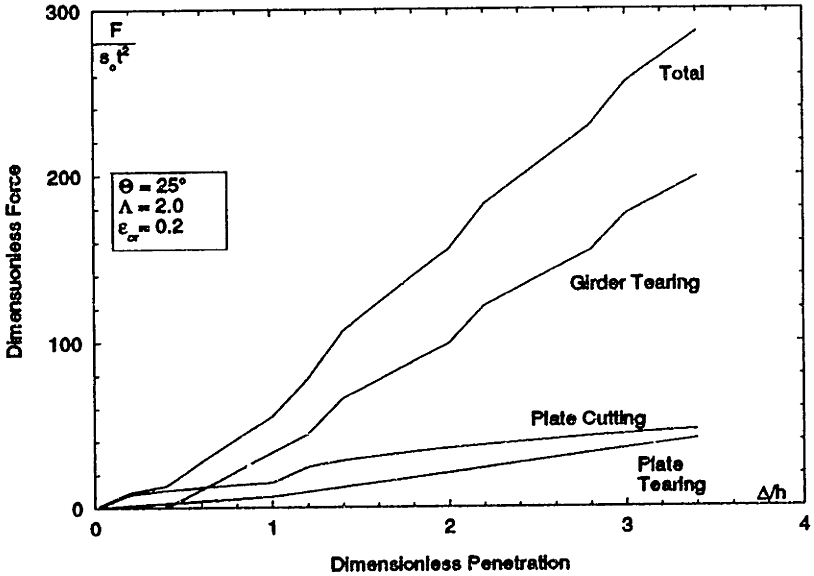

Figure 3.11 Contribution of the three primary mechanisms at $\Lambda = 2.0$

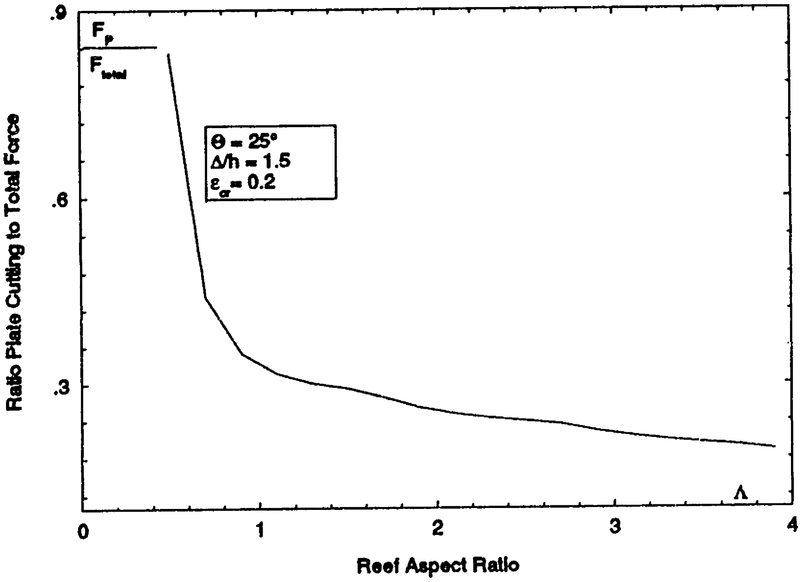

Figure 3.12 Relative contribution of plate cutting force to the total force as a function of reef aspect ratio Λ.

relatively the same. As the reef aspect ratio Λ is increased the girder tearing becomes even more significant, and the relative magnitudes of plate cutting and plate tearing remain constant.

As mentioned above, the present model refines Wierzbicki's past models [34] [35] primarily through the application of the steady state plate cutting solution. Accordingly, the greatest improvement over past models will be realized when analyzing grounding scenarios for which plate cutting is a significant mode of energy dissipation. Figures 3.9 - 3.11 show that the plate cutting force is approximately equal in magnitude to girder tearing and plate tearing forces when dimensionless penetration is less than about 2.0, and Λ is less than about 1.5. Above these values of Λ and Δ/h, plate cutting plays a smaller role in the overall resisting force of the hull structure. Figure 3.12 is a plot of the ratio of plate cutting force to the total force as a function of reef aspect ratio Λ, which helps to establish the range of maximum applicability for the present model. When $\Lambda = 1.5$ the plate cutting accounts for about 30% of the energy absorption, which is large enough to make the improvements offered by the present model important. At values of Λ greater than about 2.5, or Δ/h greater than about 2, the model is not necessarily incorrect, but its advantage over Vaughan's method is diminished.

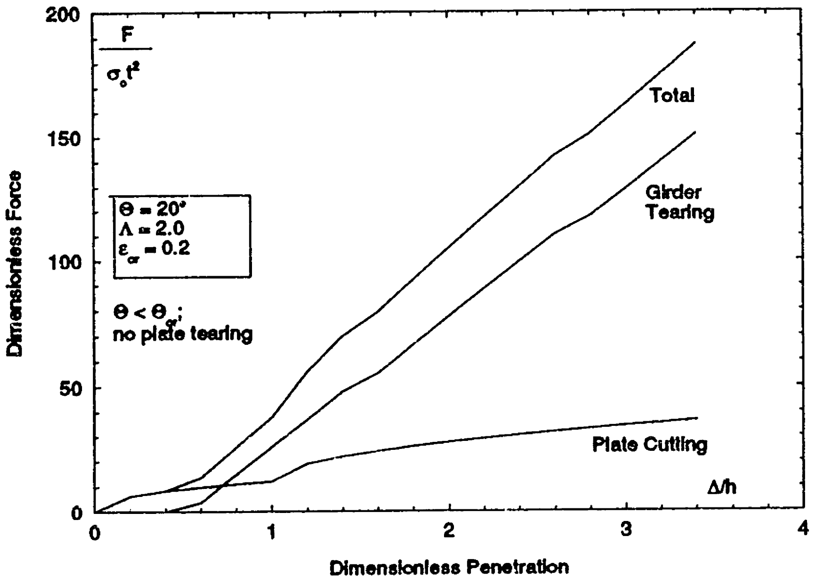

Figure 3.13 Contribution of the three primary mechanisms at $\theta = 20°$.

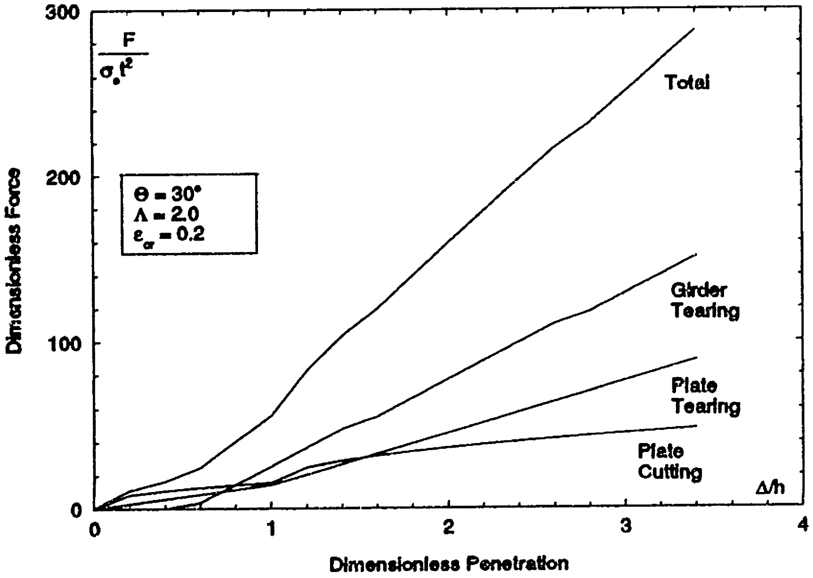

Figure 3.14 Contribution of the three primary mechanisms at $\theta = 30°$.

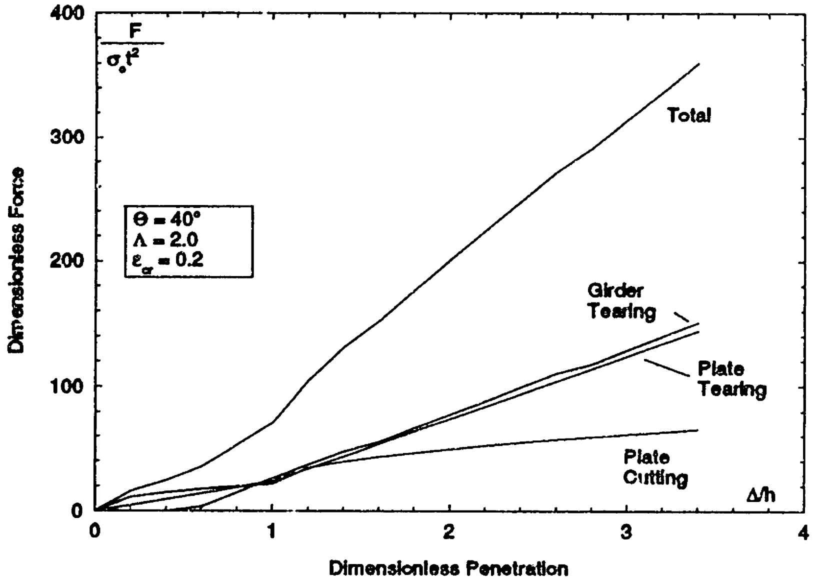

Figure 3.15 Contribution of the three primary mechanisms at $\theta = 40°$.

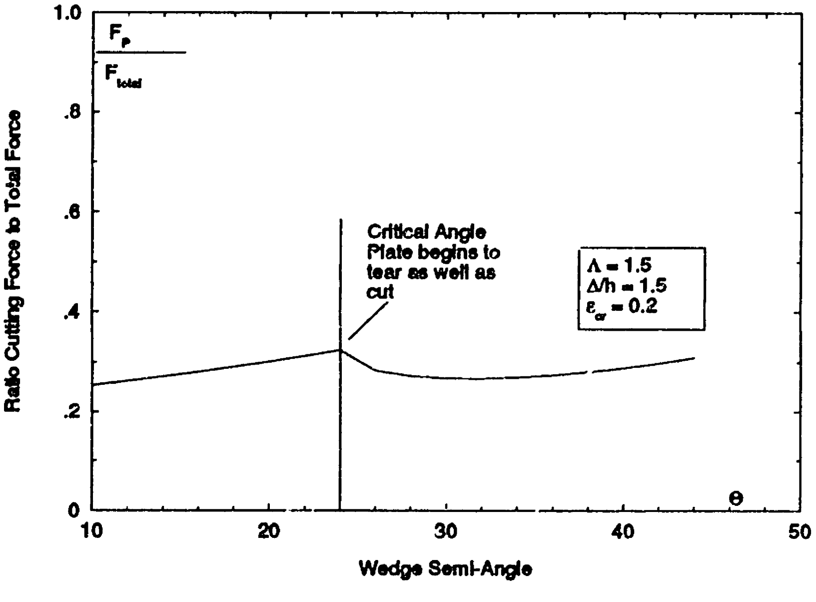

Figure 3.16 Ratio of plate cutting force to total force as a function of wedge semi-angle θ

Figures 3.13 through 3.15 show the contributions of the three primary mechanisms for various values of wedge angle at $\Lambda = 2.0$. Notice that the relative magnitude of the plate cutting force for a given value of Λ is almost constant over the range of wedge angles. This trend is shown in detail in Figure 3.16, which is the ratio of plate cutting force to total force as a function of θ. Of course, the theoretical and experimental analysis of Chapters One and Two were conducted for smaller wedge semi-angles, $10° < \theta < 30°$, and the model is most applicable within this range.

3.7.4 Application to Comparative Studies

Although the model presented here is formulated for a USDH tank vessel, the same principles and basic equations for plate cutting force, plate tearing force, and girder tearing force can be applied to any hull configuration. For a conventional double hull tanker, for example, the longitudinal stiffeners can be "smeared" to equivalent thicknesses and the model applied as described above. For a single hull vessel, the formulation is identical but a bit less complicated since the hull cell aspect ratio (s_1/h) does not enter. The damage prediction model presented here can, then, be used for comparative studies similar to those reported in References [41] and [42]. When this is done, the shortcomings of Vaughan's method for the purpose of conducting comparative studies becomes more apparent.

Consider, for example, a comparison of a mid-deck tanker to a double hull tanker for the purpose of determining relative performance in grounding. It is the ratio of the length of damage in the mid-deck tanker to the length of damage in the double hull tanker (for a given grounding scenario) that is critical to the comparative study. For clarity, the above ratio will be called the "damage ratio."

$$Damage\,Ratio = \frac{length\ of\ damage\ in\ mid\text{-}deck\ vessel}{length\ of\ damage\ in\ double\ hull\ vessel}$$

The model developed here has been used to determine the damage ratio for the USDH vessel detailed in Appendix F. The grounding scenario under consideration involves 4 meter penetration by a reef of aspect ratio $\Lambda = 2.0$. The damage ratio for the given scenario is shown as a function of reef wedge angle in Figure 3.17. Vaughan's method was also used to determine the damage ratio, and it too is plotted on Figure 3.7. The figure shows that, for a given penetration depth and reef geometry, Vaughan's method will predict the same relative performance of the two vessels over the entire range of reef semi-angles. The calculations done with the present model show that this result is misleading. As the reef semi-angle is varied, the relative performance of the mid-deck tanker to the double hull tanker (in terms on length of damage) changes, up to 25%, depending on the specific reef geometry and penetration depth examined.

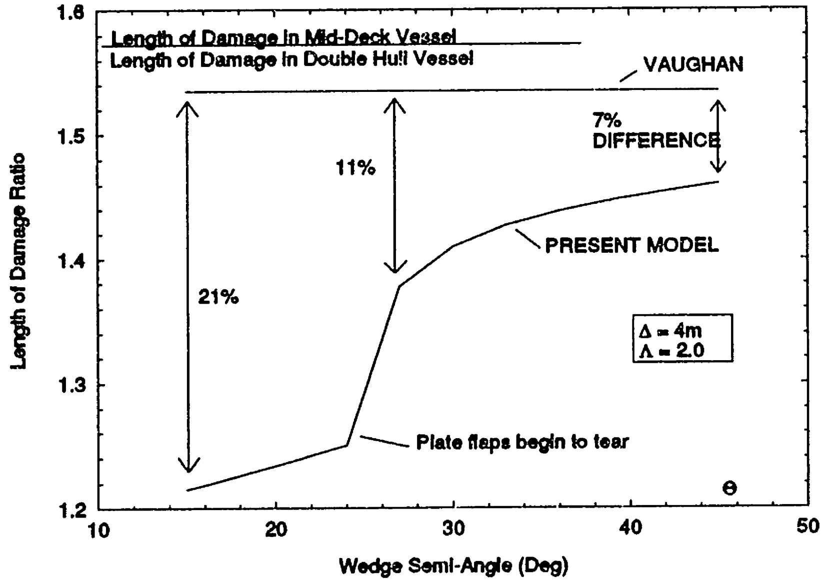

Figure 3.17 Relative performance of mid-deck tanker to double hull vessel as predicted by Vaughan, and by the present model.

It should be mentioned here that the recent comparative studies conducted for the IMO employ Vaughan's method, and that the results of those studies should be considered valid only for a small range of reef wedge semi-angles, $\theta \approx 45°$.

The general trend holds over the entire range of penetration depths, reef aspect ratios, and hull cell ratios. When smaller reef wedge semi-angles of less than 40° are considered, Vaughan's method not only over predicts absolute performance, it incorrectly predicts relative performance. For grounding scenarios in which the plate cutting and tearing modes are significant relative to the total energy absorption (for example, low aspect ratio reefs and small penetration depths) the present model will yield a substantially more realistic estimate of the damage ratio.

3.8 Conclusions

The damage prediction model developed in this chapter offers significant improvement over past damage prediction methods for the analysis of groundings on narrow, low aspect ratio reefs which involve relatively low dimensionless penetration depths. For other scenarios the model is applicable, but offers no real improvement over past methods. Analysis of groundings on wide (high reef wedge angle) or blunt (high reef aspect ratios) reefs requires a different type of model, since the primary energy dissipation modes in these scenarios does not include plate cutting or tearing, but is dominated by girder crushing, plate buckling, and plate shearing.

It is apparent from the results presented in this chapter that the existing damage prediction methods are insufficient for the purpose of conducting comparative studies over a wide range of parameters. The recent comparative studies which employed Vaughan's damage prediction method [40] should be reconsidered in light of the present analysis.

V. Conclusions

Application of steady state plate cutting mechanics to the problem of ship grounding has significantly enhanced the state-of-the-art damage prediction models for large tank vessels. Vaughan's method [40] of damage prediction is based on plate cutting experiments which involved the initiation rather than steady state mode. His empirical approach lacks generality and sensitivity to some important parameters of the problem, among the most significant of which are the wedge semi-angle θ and the materials flow stress. Wierzbicki's previous analyses [34] [35] have estimated the energy absorption of the plate with a simple tearing model only. The mechanics of plate cutting were not included. The damage prediction model developed here includes both plate tearing and plate cutting, and is based on both theoretical and experimental analysis.

The kinematic model developed in Chapter One is a simple but extremely useful representation of the plate cutting process, which allows a single term closed form solution for the cutting force to be developed for the first time. Previous analyses of plate cutting have been empirical, and as such they lack generality and are not as readily applied to ship grounding.

The steady state plate cutting experiments presented in Chapter Two, while limited in scope, are extremely important because they emphasis the fundamental difference between the steady state and initiation problems. The subsequent formulation of an approximate expression for the total resistance of a plate to the horizontal indentation of a wedge significantly contributes to the state of the art in damage prediction. This analysis recognizes for the first time that the plate resists the wedge indentation through two primary mechanisms; plate cutting and plate tearing. The plate cutting involves transverse membrane stretching in the region near the wedge tip, and plastic bending of the plate flaps in the wake of the wedge. The plate tearing involves longitudinal tearing and rupture of the plate flaps. The relative significance of these two contributions depends on the wedge geometry and material parameters.

The damage prediction model presented in Chapter Three is significant because it represents a different and relatively new approach to the problem of damage prediction for ships. It is not empirical, and it is not based on scale tests of hull sections. Instead, this analysis continues along the lines of Wierzbicki's [34 -38] work on grounding by using the fundamental concepts of plasticity and fracture mechanics to formulate a separate model of each of the primary energy absorbing mechanism involved, and then combining them for an overall model of a given hull section. The three mechanisms addressed are plate cutting, plate tearing, and girder tearing. The combination of these mechanisms through the geometries of the reef and the hull allow this model to be apply over a wide range of parameters, and make it very useful for comparative studies.

While the work reported here represents a significant advancement in damage prediction, much more work needs to be done. The need for an experimentally determined coefficient (r) in the formulation of the steady state plate cutting force is troubling. Further studies of the dependence of this coefficient on material and geometric parameters is needed. Ideally, a closed form solution for the steady state cutting force should be developed and confirmed through full scale tests.

Plate tearing in the "wide wedge" mode was not observed in the limited test program described here, although it has been in actual groundings. As a result the theoretical analysis of plate tearing presented in Section 2.2 could not be confirmed. While this analysis is based on fundamental mechanics, and improves the plate tearing models of [34] and [35], additional experiments which specifically address the wide wedge mode should be conducted.

The girder tearing model used here is also developed in an approximate way, and it too should be the subject of a series of experiments. Additionally, the interaction between these three mechanisms needs to be investigated, perhaps through a series of tests which involves cutting scale sections of a double hull. The focus of these experiments, however, must be on how the energy absorbing mechanisms interact, and not on developing an empirical method of predicting the resisting force. In this way, a method of combining the simple models of each structural member can be developed, and the overall damage prediction model will maintain generality.

The analysis of this entire thesis is applicable only to a certain class of grounding; those which involve relatively narrow and/or sharp reefs which penetrate and cut the plate. The problem of grounding on wide or blunt reefs, which may or may not penetrate the hull, and which primarily crush and shear the girders and plates, needs to be addressed separately. In fact, analysis of "blunt reef groundings" is currently underway at MIT.

Finally, work must be done on coupling the global forces of lift and friction with the steady state damage prediction. This is especially important for comparative studies because the local penetration depth of the reef into the vessel varies greatly with construction type.

VI References

1. Vaughan, H. "Bending and Tearing of Plate with Application to Ship-Bottom Damage." *The Naval Architect* 97. May 1978.

2. Jones, N. and W.S. Jouri. "A Study of Plate Tearing for Ship Collision and Grounding Damage." *J. Ship Research* 31. 253, 1987.

3. Akita, Y., N. Ando, Y. Fujita and K. Kitamura. "Studies on Collision-Protective Structures in Nuclear Powered Ships." *Nucl. Engn Design* 19. 368, 1972.

4. Akita, Y. and K. Kitamura. "A Study on Collision of Elastic Stem to a Side Structure of Ships." *J. Soc. Naval Architects of Japan*. 131. 307, 1972.

5. Minorsky, V.U. "An Analysis of Ship Collisions with Reference to Protection of Nuclear Power Plants." *J. Ship Research* 3. 1, 1959.

6. Vaughan, H. "The Tearing and Cutting of Mild Steel Plate with Application to Ship Grounding Damage." *Proc. 3rd Int. Conf. Mechanical Behavior of Materials*. Vol. 3. pp. 479-487. ed. K.F. Miller and R.F. Smith. Pergamon Press, Oxford 1979.

7. Vaughan, H. "The Tearing of Mild Steel Plates." *J. Ship Research* 24. 96, 1980.

8. Wosin, G. "Comments on Vaughan: The Tearing of Mild Steel Plates." *J. Ship Research* 26. 50, 1982.

9. N. Jones. "Scaling of Inelastic Structures Loaded Dynamically." *Structural Impact and Crashworthiness*." Vol. 1. pp. 45-74. ed. G.A.O. Davies. Elsevier Applied Science Publishers, Amsterdam 1984.

10. Jones, N., W.S. Jouri and R.S. Birch. "On the Scaling of Ship Collision Damage." Proc. 3rd Int. Congress on Marine Technology. pp. 287-294 Athens International Maritime Association of East Mediterranean. Phivos Publishing Co. Greece 1984.

11. Goldfinch, A.C. "Plate Tearing Energies." Part II Project, Engineering Department. Cambridge University, 1986.

12. Prentice, J. "Wedge Drop Test to Investigate Plate Tearing Characteristics." Part II Project. Engineering Department. Cambridge University, 1986.

13. Shu, D. "Energy Dissipation in Cutting Plates and Splitting Tubes." M. Sc. Thesis. Peking University, 1986. (in Chinese)

14. Atkins, A.G. "Scaling in Combined Plastic Flow and Fracture." *Int. J. Mech Sci* 30. 173, 1988.

15. Lu, G. and C.R. Calladine. "On the Cutting of a Plate by a Wedge." *Int. J. Mech. Sci.* Vol. 32, No. 4, pp. 295-313, 1990.

16. Atkins, A.G. "Note on Scaling In Rigid-Plastic Fracture Mechanics." *Int. J. Mech. Sci.* Vol. 32, No. 6, pp. 547-548, 1990.

17. Atkins, A.G. "Letter to the Editor." *Int. J. Mech Sci.* Vol. 33, No. 1, pp. 69-71, 1991.

18. Stronge, W.J., T.X. Yu and W. Johnson. "Long Strike Energy Dissipation in Splitting Tubes." *Int. J. Mech. Sci.* 25, 637-647, 1983.

19. Stronge, W.J, T.X. Yu and W. Johnson. "Energy Dissipation by Splitting and Curling Tubes." *Structural Impact and Crashworthiness*, Vol. 2, pp. 576-587. ed. J. Morton. Applied Science Publishers, London 1984.

20. Reddy, T.Y and S.R. Reid. "Axial Splitting of Circular Metal Tubes." *Int J. Mech. Sci.* 28, 111-131, 1986.

21. Atkins, A.G. and Y.W. Mai. Elastic and Plastic Fracture, pp. 312-316. John Wiley, Chichester, 1985.

22. Yu,T.X., D.J. Zhang, Y. Zhang and Q. Zhou. "A Study of the Quasi-Static Tearing of Thin Metal Sheets." *Int. J. Mech. Sci.* Vol. 30, No. 3/4, pp.193-202, 1988.

23. Wierzbicki, T. and W. Abramowicz. "On the Crushing Mechanics of Thin Walled Structures." *J. Applied Mech.* Vol. 50, No. 4a, pp. 727-734, 1983.

24. Wierzbicki, T. and W. Abramowicz. "Axial Crushing of Multicorner Sheet Metal Columns." *J. Applied Mech.* Vol. 56, No. 1, pp. 113-120, 1989.

25. Magre, G.L. and P.H. Thornton. "Design Consideration in Energy Absorption by Structural Collapse." SAX paper No. 78-434.

26. Parks, D.M., L.B. Freund and J.R. Rice. "Running Ductile Fracture in a Pressurized Line Pipe." *Mechanics of Crack Growth, ASTM STP 590.* American Society for Testing and Materials, Philadelphia, pp. 2543-262, 1976.

27. D.M. Parks and L.B. Freund. "Discussion of 'Steady-State Crack Propagation in Pressurized Pipelines Without Backfill' by M.F. Kanninen, et al." *J. Pressure Vessel Technology*, 98, pp. 323-324, 1976.

28. Parks, D.M. and L.B. Freund. "Analytical Interpretation of Running Ductile Fracture Experiments in Gas Pressurized Linepipe." *Crack Arrest Methodology Applications, ASTM STP 711*. ed. G.T. Hahn and M.F. Kanninen. American Society for Testing and Materials, Philadelphia, 1980, pp. 359-378.

29. Hopkins, H.G. "On the Behavior of Infinitely Long Rigid-Plastic Beams Under Transverse Concentrated Load." *J. Mech. Phys. Soilds*, Vol. 4, pp. 38-52, 1955.

30. Baumeister, T. ed. Marks' Standard Handbook for Mechanical Engineers. 8th ed., McGraw-Hill Book Company, New York, 1978.

31. Atkins, A.G. Private Communication, February 1992.

32. Jones, N. Private Communication, February 1992.

33. McClintok, F. Private Communication, February 1992.

34. Wierzbicki, T., E. Rady, D. Peer, and J.G. Shin. "Damage Estimates in High Energy Groundings of Ships." Joint M.I.T. - Industry Program on Safe Tankers, Report No.1, June 1990.

35. Wierzbicki, T., D. Peer, and E. Rady. "The Anatomy of Tanker Grounding." Joint M.I.T. - Industry Program on Safe Tankers, Report No.2, May 1991.

36. McKenney, T.L. "Grounding Resistance of Unidirectionally Stiffened Double Hulls." Joint M.I.T. - Industry Program on Safe Tankers, Report No.3, May 1991.

37. Peer, D.B. "Coupling of Global Motion and Local Deformation in Tanker Grounding" Joint M.I.T. - Industry Program on Safe Tankers, Report No.4, May 1991

38. Thomas, P. and T. Wierzbicki. "Performance Criteria vs Design Standards for Commercial Tank Vessels." Joint M.I.T. - Industry Program on Safe Tankers, Report No.5, October 1991. Presented at the Fifth International Symposium on Practical Design of Ships and Mobile Units, May 1992.

39. Beach, J. "Cluster Technologies." Trans. ASNE Destroyer, Cruiser, and Frigate Symp. 29 Sept. 1990.

40. Vaughan, H. "Damage to Ships Due to Collision and Grounding." Det norske Veritas report, DnV 77-345.

41. Kohler, P.E., et al., "Potential Oil Spill From Tankers in Case of Collision and/or Grounding - A Comparative Study of Different VLCC Designs." DnVC Report 90-0074, May 1990.

42. Snyder, B. and D. Mcafee, "Collision Assesment of Double Hull Tankers." DTRC Report SSPD-92-173, Jan 1992.

43. Report of the RR701 Committee to the Maritime Environmental Protection Committee of the IMO, Shipbuilding Research Association of Japan, 1978.

44. Kuroiwa, T. Research Engineer, Mitsubishi Heavy Industries, LTD, Nagasaki, Japan. Private Communication April 1992.

45. Calladine, C.R. Private Communication, February 1992.

Appendix A

The Tube Crushing Analogy

It is of interest to discuss the significance of the exponents in Equation (1.1) through the example of a related, well understood problem in structural plasticity, the axial crushing of a square prismatic tube of width b. The origin of the fractional power n can be related to the way work is partitioned between the near-tip and far-field events. Resistance of the tube can be conveniently measured by the so-called mean crushing force, P_m. The expression for dimensionless mean crushing force, derived in references [23] and [24] has the form;

$$\frac{P_m}{M_o} = A_1 \frac{b}{H} + A_2 \frac{r}{t} + A_3 \frac{H}{r}, \qquad \textbf{(A1)}$$

where $M_o = (2/\sqrt{3})\ \sigma_o t^2/4$, is a fully plastic bending moment of the plate strip per unit length, A_1, A_2, A_3 are numerical constants, and, as shown in Figure A1, H is the half length of the folding wave and r is the local radius of curvature (rolling radius) of the diagonal fold lines. The three terms on the right hand side of (A1) represent the work of bending about stationary horizontal hinge lines, the work of bending and re-bending (rolling) in the inclined, moving hinge lines, and the membrane work in the "corner" deformation, respectively. It can be seen from (A1) that the individual work contributions are not independent but are related through

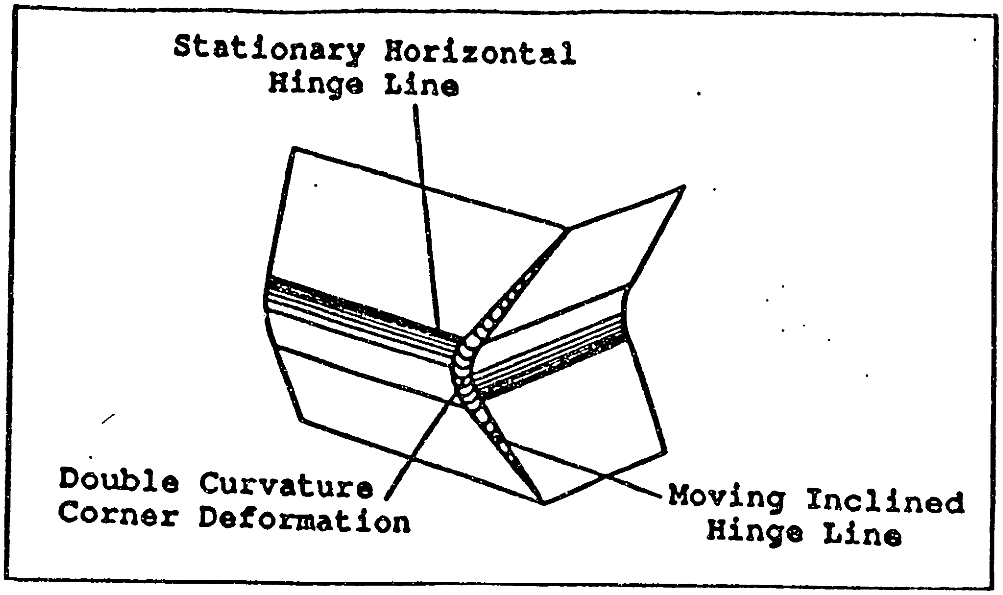

Figure A1 The three energy absorbing mechanisms in the "Basic Folding Element"

two geometric parameters, H and r. Equation (A1) is derived from equating the applied work to the plastic work for incremental deformation of a currently kinematically admissible flow field; it is an approximate upper bound to the crushing force.

The corresponding lowest upper bound to the crushing force is found by minimization of (A1) with respect to the parameters H and r. It leads to;

$$P_m = \frac{3}{4} (A_1 A_2 A_3)^{\frac{1}{3}} \sigma_o t^{\frac{5}{3}} b^{\frac{1}{3}} \qquad \textbf{(A2)}$$

Two important conclusions can be drawn from this minimization process;

(i). The three-term equation (A1) is reduced to a one-term expression. Thus, a one-term formula describes the mean crushing force of the tube even though the plastic work involves three distinct mechanisms.

(ii). At the minimum point, the contribution of all three terms in (A1) turns out to be the same. As a result, two-thirds of the work goes to bending (at the stationary and moving hinge lines) while one-third of the work is dissipated by membrane stretching.

In Section 1.5 it was shown that two-thirds of the work goes into membrane stretching and one-third into bending for the plate cutting process.

From the tube crushing solution it can be inferred that a single-term solution for the penetration force with a fractional power coefficient can be obtained if a deformation mode involves a coupling between bending and membrane action through a geometric parameter. Such a deformation mode is identified in the Section 1.3.

Appendix B

Estimation of Shear Work

The neglect of shear strain in the rate of work calculation (Section 1.5) requires additional justification. To do this, the following supplementary assumptions must be made:

(i) The shear work is uncoupled from the membrane energy in the transverse direction.

(ii) The transverse velocity in the plastic zone is a parabolic diminishing function of y.

(iii) The width and length of the membrane deformation zone are related as shown in Figure B1.

Consider the case that the energy dissipation occurs in a pure shear flow, i.e. $\dot{\varepsilon}_{xx} = \dot{\varepsilon}_{yy} = 0$ (assumption (i)). It then follows from the yield condition (1.8) and the associated flow rule (1.9) that $\sigma_{xx} = \sigma_{yy} = 0$, and $\sigma_{xy} = \sigma_o/\sqrt{3}$. The condition that the longitudinal strain rate vanishes $\dot{\varepsilon}_{xx} \equiv 0$, implies that the longitudinal component of the velocity vector must be zero $V_x = 0$. The shear component of the strain rate is then

$$\dot{\varepsilon}_{xy} = \frac{1}{2}\frac{\partial V_y}{\partial x} . \qquad \textbf{(B1)}$$

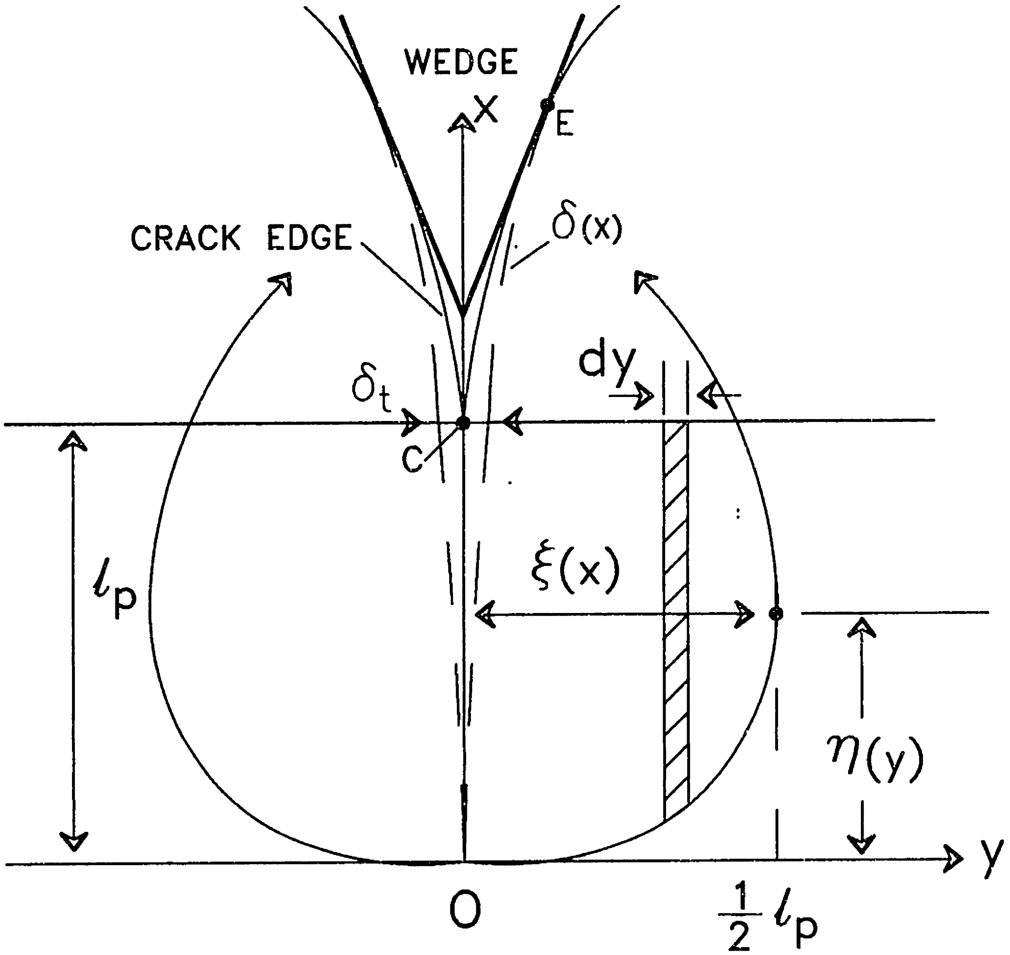

Figure B1 The near-tip deformation zone for which the rate of work in shear is estimated.

The corresponding rate of work in shear is

$$\dot{E}_{shear} = \int_S 2\, t\sigma_{xy}\dot{\epsilon}_{xy}\, dS = 2\int_0^{\xi}\int_{\eta}^{l_p} 2\, t\frac{\sigma_o}{\sqrt{3}}\,\frac{1}{2}\,\frac{\partial V_y}{\partial x}\, dx\, dy\,, \tag{B2}$$

where the area S over which the integral is taken is shown in Figure B1. The integration with respect to x is readily performed;

$$\dot{E}_{shear} = \frac{2}{\sqrt{3}}\sigma_o t \int_0^{\frac{l_p}{2}} V_y(y)\, dy\,. \tag{B3}$$

Given assumptions (ii) and (iii), the transverse velocity field in the near tip region (see Figure 1.2) is taken in the form;

$$V_y(y) = V_n\left(\frac{2y}{\ell_p}\right)^2 . \tag{B4}$$

Substituting (B4) into (B3) and integrating one obtains;

$$\dot{E}_{shear} = \frac{\sigma_o\, t\, V_n\, \ell_p}{3\sqrt{3}} . \tag{B5}$$

Comparison of Equation (B5) with Equation (1.22) for the rate of membrane work in the purely transverse stretching mode shows that $\dot{E}_{shear} \approx 0.25\ \dot{E}_m$. This however is an upper bound for the rate of work in shear stretching because in uncoupling the calculations the circumscribed yield surface was used. It is reasonable to take the average between the circumscribed and inscribed yield conditions by applying a reduction factor of 0.85. When this is done, the total rate of work in membrane stretching and shear becomes;

$$\dot{E}_m + \dot{E}_{shear} = (0.85)\,1.25\,\dot{E}_m = 1.06\,\dot{E}_m . \tag{B6}$$

This is only 6% higher than the rate of work calculated on the basis of transverse stretching alone. It can, therefore, be concluded that as long as assumptions (i) through (iii) hold, the neglect of shear deformation in the calculation of rate of membrane work does not lead to any appreciable loss of accuracy. The shape of the near-tip plastic zone however, may be strongly affected by the presence of shear.

Appendix C

Experimental Apparatus Construction Details

The following figures give construction details for the support frame and wedges made for the experiments reported in Chapter Two.

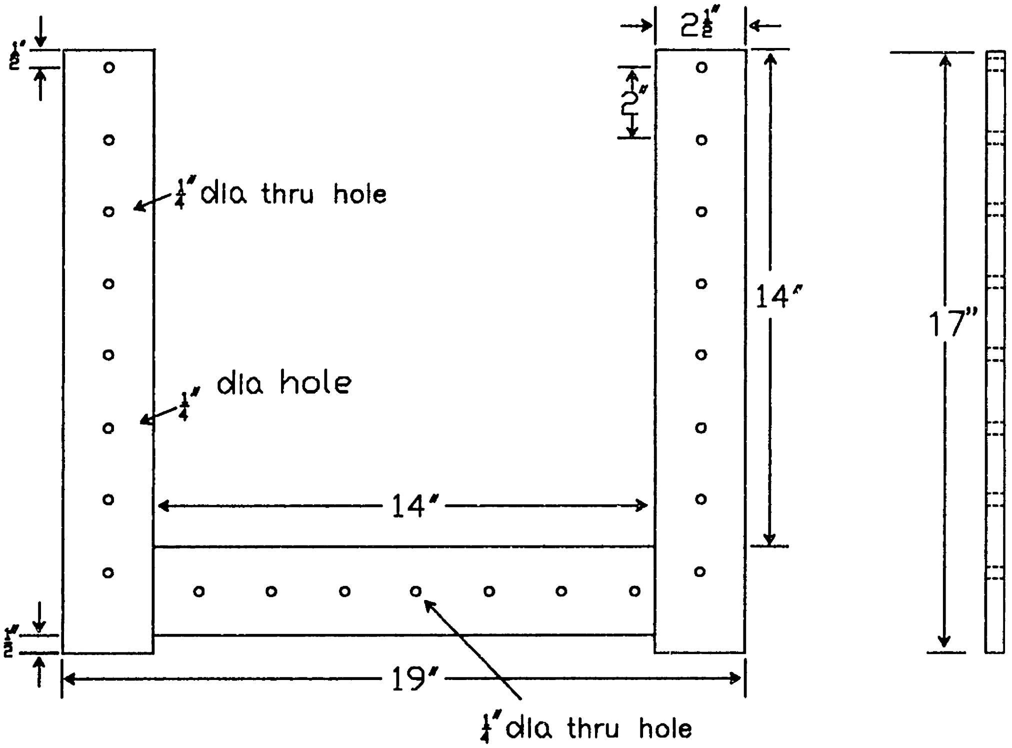

Figure C1. Inner frame details.

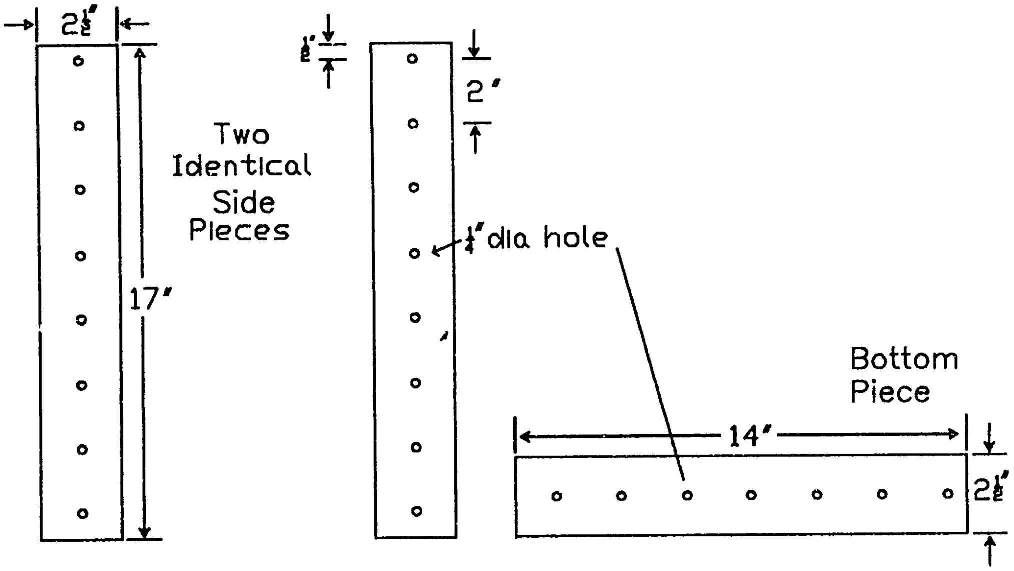

Figure C2. Outer frame.

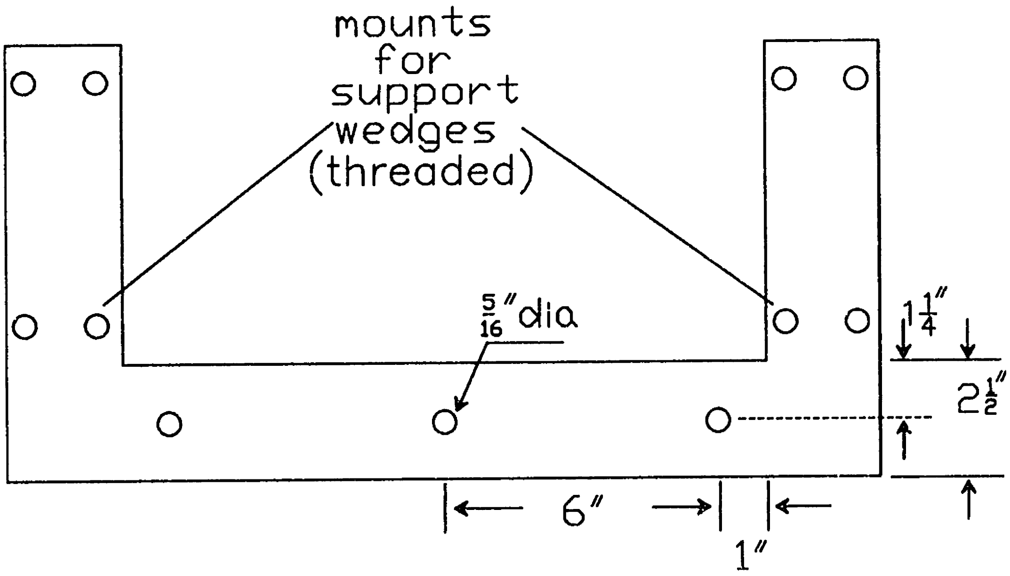

Figure C3. Bottom frame mount.

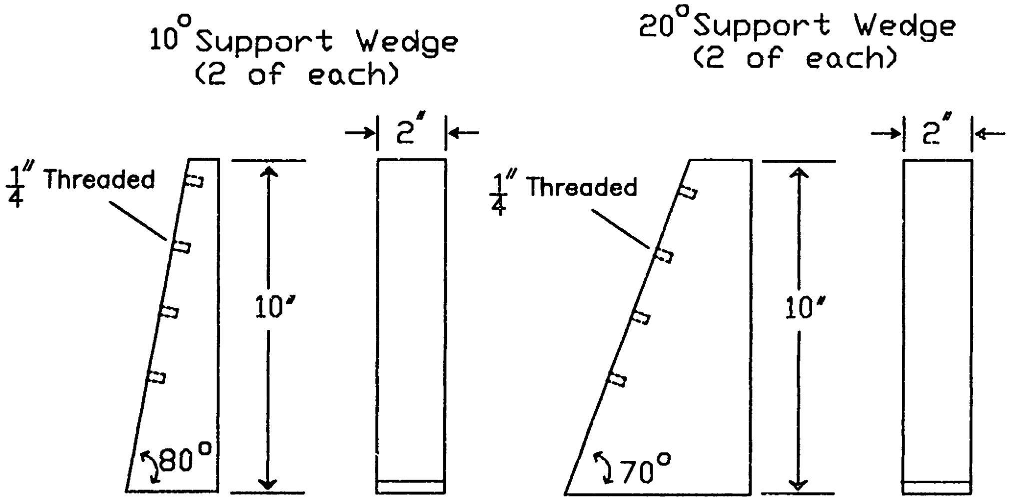

Figure C4. Side supports.

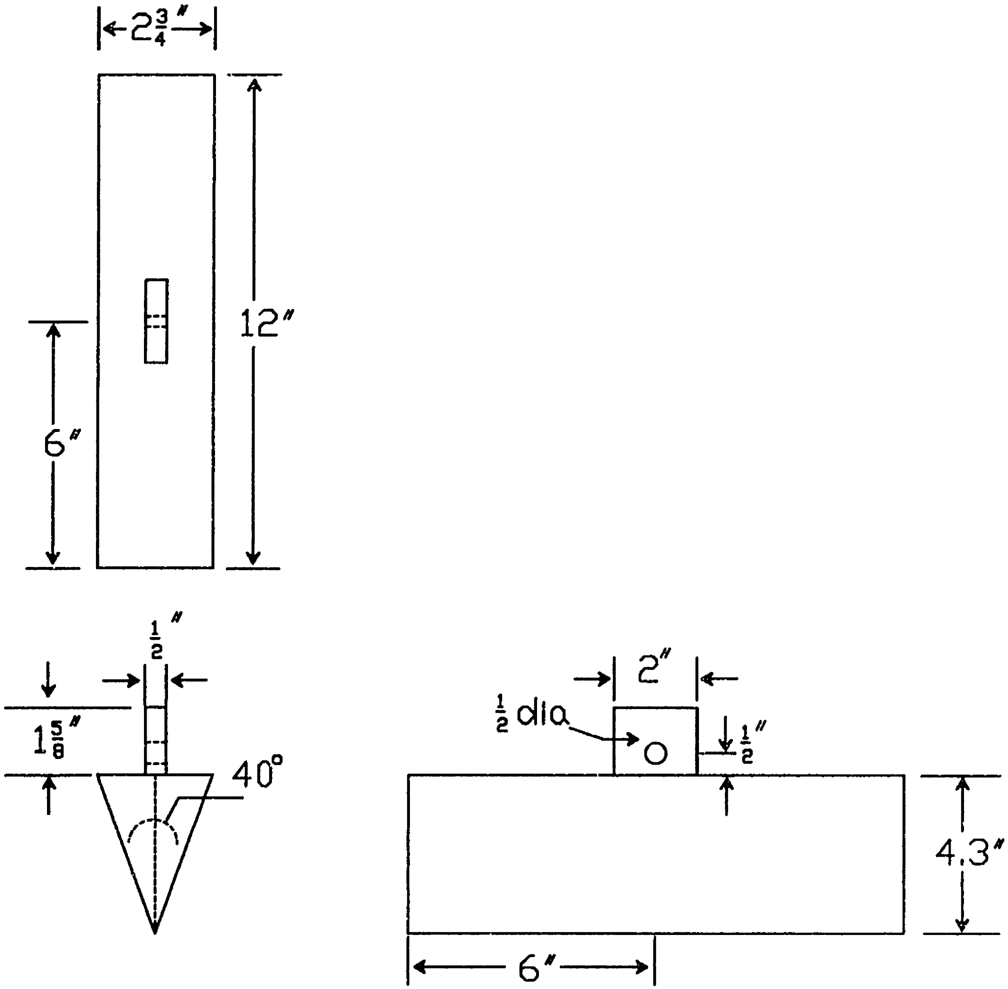

Figure C5. Wedge #1

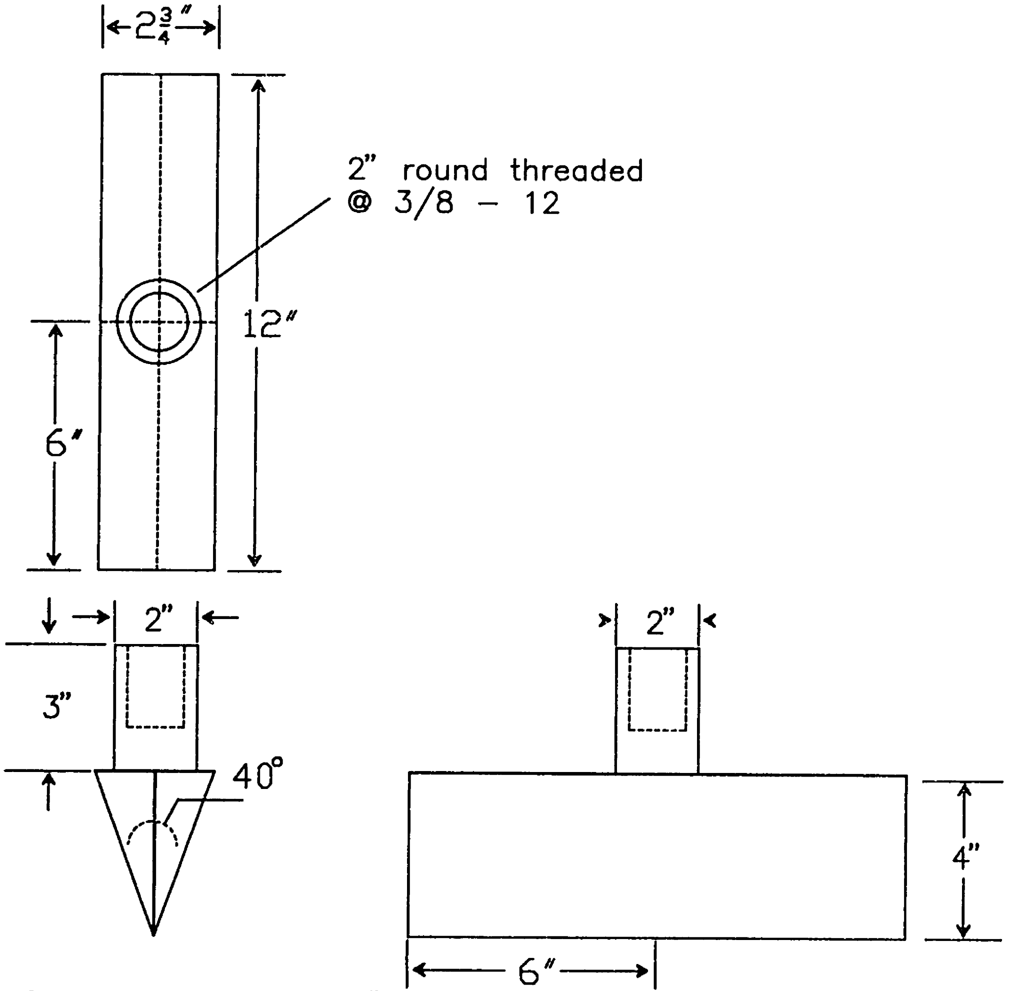

Figure C6. Wedge #2

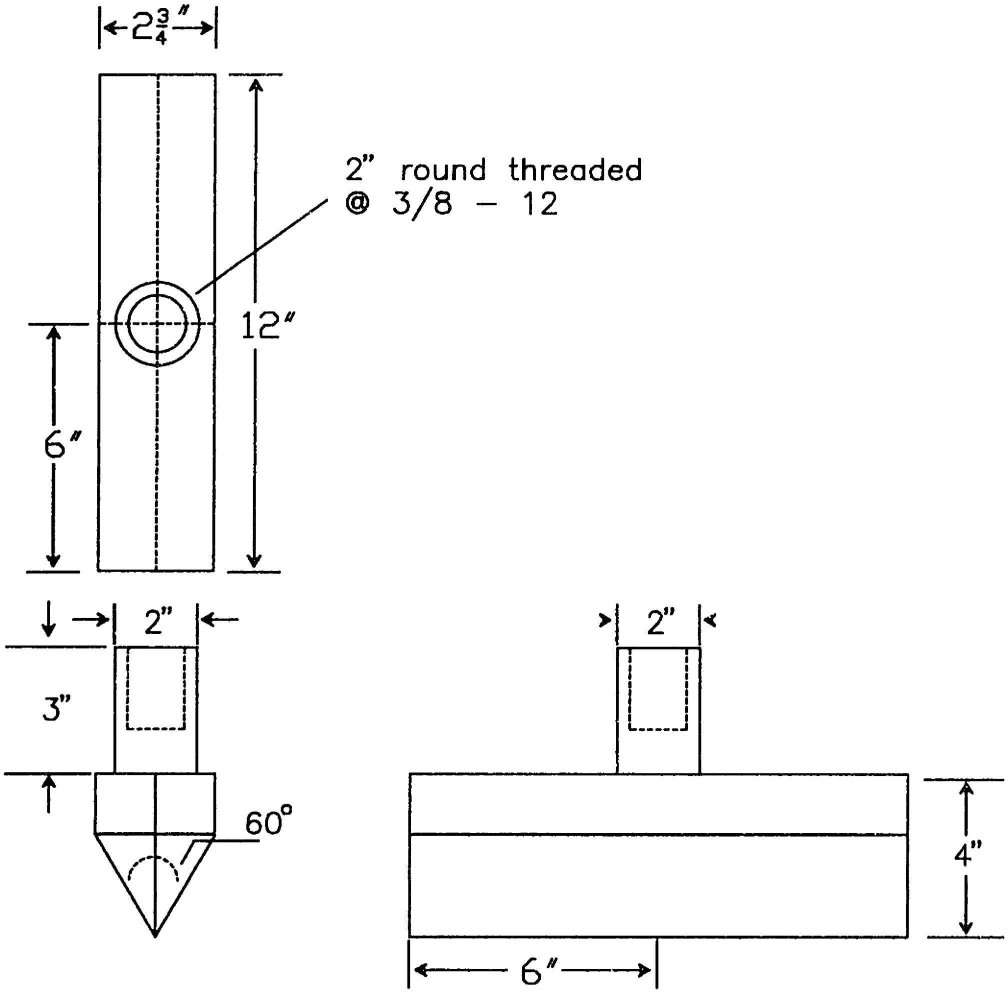

Figure C7. Wedge #3

Appendix D.

Experimental Data

A. Test Sample Specifications

Sample #	1
Material Type	3030 AL
Sample Thickness	1/16" (1.587mm)
Dimensions	19 X 16.5 in
Average Yield Strength	113.0 MPa

Sample #	2
Material Type	3030 AL
Sample Thickness	1/16" (1.587mm)
Dimensions	19 X 16.5 in
Average Yield Strength	114.25 MPa

Sample #	3
Material Type	3030 AL
Sample Thickness	1/16" (1.587mm)
Dimensions	19 X 16.5 in
Average Yield Strength	114.25 MPa

Sample #	4
Material Type	3030 AL
Sample Thickness	1/16" (1.587mm)
Dimensions	19 X 16.5 in
Average Yield Strength	114.0 MPa

Sample #	5
Material Type	3030 AL
Sample Thickness	1/32" (0.794mm)
Dimensions	19 X 16.5 in
Average Yield Strength	114.5 MPA

Sample #	6
Material Type	3030 AL
Sample Thickness	1/32" (0.794mm)
Dimensions	19 X 16.5 in
Average Yield Strength	113.25 MPa

Sample #	7
Material Type	3030 AL
Sample Thickness	1/32" (0.794mm)
Dimensions	19 X 16.5 in
Average Yield Strength	113 MPa

Sample #	8
Material Type	3030 AL
Sample Thickness	1/32" (0.794mm)
Dimensions	19 X 16.5 in
Average Yield Strength	113.5 MPa

Sample #	9
Material Type	3030 AL
Sample Thickness	1/64" (0.397mm)
Dimensions	19 X 16.5 in
Average Yield Strength	111.5 MPA

Sample #	10
Material Type	3030 AL
Sample Thickness	1/64" (0.397mm)
Dimensions	19 X 16.5 in
Average Yield Strength	111.0 MPa

Sample #	11
Material Type	3030 AL
Sample Thickness	1/64" (0.397mm)
Dimensions	19 X 16.5 in
Average Yield Strength	111.5 MPa

Sample #	12
Material Type	3030 AL
Sample Thickness	1/64" (0.397 mm)
Dimensions	19 X 16.5 in
Average Yield Strength	110.5 MPa

Sample #	13
Material Type	ASTM A366 Steel
Sample Thickness	1.47 mm
Dimensions	19 X 16.5 in
Average Yield Strength	228 MPA

Sample #	14
Material Type	ASTM A366 Steel
Sample Thickness	1.47 mm
Dimensions	19 X 16.5 in
Average Yield Strength	225.5 MPA

Sample #	15
Material Type	ASTM A366 Steel
Sample Thickness	1.47 mm
Dimensions	19 X 16.5 in
Average Yield Strength	227.5 MPA

Sample #	16
Material Type	ASTM A366 Steel
Sample Thickness	1.47 mm
Dimensions	19 X 16.5 in
Average Yield Strength	228 MPA

Sample #	17
Material Type	ASTM A366 Steel
Sample Thickness	1.47 mm
Dimensions	19 X 16.5 in
Average Yield Strength	228 MPA

Sample #	18
Material Type	ASTM A366 Steel
Sample Thickness	1.47 mm
Dimensions	19 X 16.5 in
Average Yield Strength	228 MPA

Sample #	19
Material Type	ASTM A366 Steel
Sample Thickness	2.0 mm
Dimensions	19 X 16.5 in
Average Yield Strength	225 MPA

Sample #	20
Material Type	ASTM A366 Steel
Sample Thickness	2.0 mm
Dimensions	19 X 16.5 in
Average Yield Strength	225.5 MPA

Sample #	21
Material Type	ASTM A366 Steel
Sample Thickness	2.0 mm
Dimensions	19 X 16.5 in
Average Yield Strength	225 MPA

Sample #	22
Material Type	ASTM A366 Steel
Sample Thickness	2.0 mm
Dimensions	19 X 16.5 in
Average Yield Strength	225 MPA

Sample #	23
Material Type	ASTM A366 Steel
Sample Thickness	2.0 mm
Dimensions	19 X 16.5 in
Average Yield Strength	225 MPA

Sample #	24
Material Type	ASTM A366 Steel
Sample Thickness	2.0 mm
Dimensions	19 X 16.5 in
Average Yield Strength	225 MPA

Appendix E.

Calculation of Steady State Resisting Force for Longitudinal Girders

The assumed deformation mode for the longitudinal girder is shown in Figure E1. The girder is forced outward by the reef and bent about a hinge a distance τ up from the bottom plate, where $0< \tau \leq h$ is the height at which the local rock width b is precisely equal to s_1. Although the characteristic wave length of the flaps is not known precisely, it is known from experimental observation and photographs of actual groundings that the pattern does exist. In the present formulation it is convenient to take this characteristic length to be equal to the wedge length ℓ^* or some multiple of it. It is shown later that the exact value is not needed to obtain the estimated force.

This formulation follows closely the tearing model for the bottom plate developed in [34] and [35], and applied in [37], as well as in Section 2.2 of this paper. It also agrees in methodology with the work of Vaughan [40] who estimated the grounding damage by relating the force to the volume of material effected. Friction is not included in the present formulation.

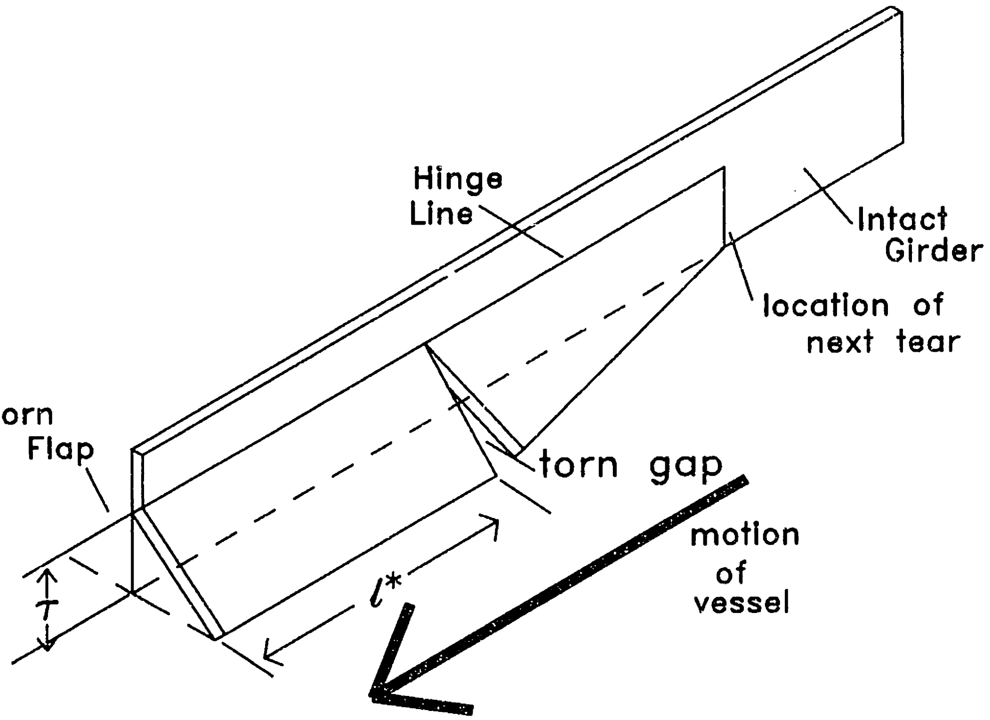

Figure E1. Steady state deformation mode for the longitudinal girders.

The solution for resisting force of the girders begins by equating the external work with the internal resistance of the girder over the characteristic distance ℓ^*

$$F_g\ell^* = E_m + E_b + E_{frac} \tag{E1}$$

It is shown in [34] and [36] that the work of bending the girder about the hinge at τ is an order of magnitude less than the membrane work required to tear the flap. Likewise, the work of fracture is neglected in [33] and [39] for the same reason. The plastic zone near the tip of the vertical crack in the longitudinal girder is an order of magnitude smaller than the plastic membrane zone which surrounds the torn region. Neglecting the work of bending and the work of fracture, Equation (E1) becomes

$$F_g \ell^* = E_m . \tag{E2}$$

In the plane strain rupture condition,

$$E_m = t \int_S \sigma_o \, \epsilon_{cr} \, dS . \tag{E3}$$

For the assumed geometry shown in Figure E1 the integration of Equation (E3) yields

$$E_m = t \, \sigma_o \epsilon_{cr} \tau \, \ell^* . \tag{E4}$$

The characteristic wave length of the flaps is eliminated by substituting (E4) into (E2);

$$F_g = t \, \sigma_o \epsilon_{cr} \tau . \tag{E5}$$

Equation (E5) is identical in form to the expressions for tearing of the bottom plate derived by Vaughan [40] and Wierzbicki [34].

Appendix F

Calculations for USDH Tank Vessel

The dimensionless plots presented in Section 3.6 were produced from a spread sheet which used the equations derived in this appendix. Since these expressions are not truly dimensionless until a specific hull is analyzed, the following scantlings for a 39,000 DWT USDH tank vessel are used when necessary;

$t_{p1} = 16$ mm $t_{p2} = 14$ mm $t_g = 14.5$ mm

$h = 1.6$ M $s_1 = 2$ M

The resulting dimensionless ratios are used;

$h/tp_1 = 100$ $h/t_{p2} = 114$ $s_1/h = 1.25$ $h/t_g = 110$

Equation (3.14) for the cutting force in the bottom plate can be non-dimensionalized as follows;

$$\frac{F_{c_1}}{\sigma_1 \, t_{p_1}^{\,2}} = 1.265\,\Lambda^{0.4}\,r^{0.4}\,(\bar{\delta}_t)^{0.6}\left(\frac{\Delta}{t_{p_1}}\right)^{0.4} g'(\theta)\,, \qquad (\Delta > 0) \qquad \textbf{(F1)}$$

This expression is further simplified by setting r = 2 and $\bar{\delta}_t$ = 1, and expressing the dimensionless cutting force in terms of dimensionless penetration depth:

$$\frac{F_{c_1}}{\sigma_o \, t_{p_1}^{\,2}}\left(\frac{\Delta}{h}\right) = 1.67\,\Lambda^{0.4}\left(\frac{h}{t_{p_1}}\right)^{0.4}\left(\frac{\Delta}{h}\right)^{0.4} g'(\theta)\,, \quad \left(\frac{\Delta}{h} > 0\right) \qquad \textbf{(F2)}$$

Now, using the dimensionless ratio (h/t_{p1}) for the specific hull chosen, the force to cut the bottom plate is expressed:

$$\frac{F_{C_1}}{\sigma_o\, t_{P_1}^{\,2}} = 10.54\ \Lambda^{0.4}\left(\frac{\Delta}{h}\right)^{0.4} g'(\theta)\ , \qquad \left(\frac{\Delta}{h} > 0\right). \qquad \textbf{(F3)}$$

The dimensionless cutting force in the inner bottom plate is arrived at in a similar fashion:

$$\frac{F_{C_2}}{\sigma_o\, t_{P_2}^{\,2}} = 11.1\ \Lambda^{0.4}\left(\frac{\Delta}{h} - 1\right)^{0.4} g(\theta)\ , \qquad \left(\frac{\Delta}{h} \geq 1\right). \qquad \textbf{(F4)}$$

Equation (3.16), for the tearing force in the bottom plate, can be non-dimensionalized as follows:

$$\frac{F_{T_1}}{\sigma_o\, t_{P_1}^{\,2}} = \frac{\epsilon_{cr}\,\Delta\,\Lambda}{t_{P_1}}\left[1 - \frac{\epsilon_{cr}\cos\theta}{(\tan\theta)^2}\right], \qquad (\theta > \theta_{cr})\ . \qquad \textbf{(F5)}$$

Again, expressing the dimensionless tearing force in terms of dimensionless penetration, and using the ratio (h/t_{p1}) given above, Equation (F5) becomes,

$$\frac{F_{T_1}}{\sigma_o\, t_{P_1}^{\,2}}\left(\frac{\Delta}{h}\right) = 100\,\epsilon_{cr}\Lambda\left(\frac{\Delta}{h}\right)\left[1 - \frac{\epsilon_{cr}\cos\theta}{(\tan\theta)^2}\right], \qquad (\theta > \theta_{cr})\ . \qquad \textbf{(F6)}$$

The dimensionless tearing force in the inner bottom plate is expressed in a similar fashion:

$$\frac{F_{T_2}}{\sigma_o\, t_{p_2}{}^2}\left(\frac{\Delta}{h}\right) = 110\,\epsilon_{cr}\Lambda\left(\frac{\Delta}{h} - 1\right)\left[1 - \frac{\epsilon_{cr}\cos\theta}{(\tan\theta)^2}\right], \quad \left(\theta > \theta_{cr} \;\wedge\; \frac{\Delta}{h} > 1\right). \tag{F7}$$

Finally, the girder resisting force given by Equation (3.22) is non-dimensionalized:

$$\frac{F_g}{\sigma_o\, t_g^2} = \sum_{m=1}^{k} 2\,\frac{\epsilon_{cr}}{t_g}\,\tau_m \qquad (k = 1,2,3\ldots)\,. \tag{F8}$$

The distance τ_m is made dimensionless and expressed in terms of dimensionless penetration depth (Δ/h) as follows;

$$\overline{\tau}_m = \frac{\tau_m}{h} = \left(\frac{\Delta}{h}\right) - \frac{(2m-1)}{\Lambda}\left(\frac{s_1}{h}\right). \tag{F9}$$

For the geometry given the ratio (s_1/h) is known and the dimensionless distance $\overline{\tau}_m$ is,

$$\overline{\tau}_m = \frac{\Delta}{h} - 1.25\left[\frac{(2m-1)}{\Lambda}\right]. \tag{F10}$$

In this case the limitation $\overline{\tau}_m \le 1$ applies.

Substituting (F10) into (F8), and using the value of (h/t_g) given above, the dimensionless girder force is expressed in terms of dimensionless penetration depth,

$$\frac{F_g}{\sigma_o\, t_g^2}\left(\frac{\Delta}{h}\right) = \sum_{m=1}^{k} 220\,\epsilon_{cr}\,\overline{\tau}_m\,, \qquad (k=1,2,3\ldots.)\,. \tag{F11}$$

Here, k is expressed in terms of (Δ/h),

$$k = \frac{1}{2}\left[\left(\frac{h}{s_1}\right)\left(\frac{\Delta}{h}\right)\Lambda + 1\right] , \qquad \textbf{(F12)}$$

and using the ratio (h/s_1) for the specific hull geometry given above,

$$k = 0.4\left(\frac{\Delta}{h}\right)\Lambda + 0.5 , \qquad \textbf{(F13)}$$

rounded down to the nearest integer as before.

It is important to note that while the dimensionless ratios used to describe the hull construction in this analysis are derived from a specific design, it is reasonable to assume that these ratios are representative of any USDH section.